The Pennsylvania State University

The Graduate School

Department of Mechanical Engineering

A COMPARISON OF HELICOPTER ACTIVE ROTOR GUST REJECTION AND VIBRATION ALLEVIATION METHODS

A Thesis in

Mechanical Engineering

by

Jonas Corl

Submitted in Partial Fulfillment
of the Requirements
for the Degree of

Master of Science

August 2009

The thesis of Jonas Corl was reviewed and approved* by the following:

Christopher D. Rahn
Professor of Mechanical Engineering
Thesis Co-Advisor

Edward C. Smith
Professor of Aerospace Engineering
Thesis Co-Advisor

Stephen C. Conlon
Assistant Professor of Aerospace Engineering
Thesis Co-Advisor

Liming Chang
Professor of Mechanical Engineering

Karen A. Thole
Professor of Mechanical Engineering
Head of the Mechanical and Nuclear Engineering Department

*Signatures are on file in the Graduate School

ABSTRACT

Dynamic Interface (DI) tasks such as station keeping, takeoff, and landing during helicopter-ship interactions are often unacceptably workload-intensive due not only to close quarters and a rolling ship, but also to a gusty environment that is amplified by ship superstructure. Previous research has focused on creating controllers with the ship's airwake properties included in the synthesis in order to compensate for gusts without affecting pilot commands. These controllers alleviate gusts using either the standard swashplate-based control or using trailing-edge flaps (TEFs) but both methods show similar performance. This study investigates the effects of both controllers on the requirements of the swashplate actuators. A nonlinear inverse kinematic and dynamic model of the swashplate mechanism is developed that relates the blade pitching motions to actuator and pitch link motions and forces. Results from simulations of a UH-60 Blackhawk landing on an LHA class ship in various airwakes are input into the swashplate model to determine the motion and forces required of the actuators. The controllers are compared with regard to their relative impact on component wear and fatigue. Trailing edge flap based gust alleviation is shown to reduce the total actuator cumulative travel by 31% and the number of direction reversals in a single actuator by 38%.

Helicopter vibrations can exacerbate the effects of high workload environments by increasing pilot fatigue and causing back pain during long missions. Previous work has shown that active rotors equipped with trailing edge flaps are able to significantly reduce helicopter vibrations at the rotor hub and pilot seat. Trailing edge flap and root pitch methods of active rotor vibration control from previous studies are compared in terms of vibration reduction capabilities and required actuation force, power, and weight. Root pitch control and trailing edge flaps show closed loop multi-axis vibration reductions of 84% and 90%, respectively. Trailing edge flaps are found to be the most desirable due to low actuation power requirements. Current actuation technology, however, is not sufficient for trailing edge flaps on heavy helicopters, whereas root pitch actuation has been successfully demonstrated.

TABLE OF CONTENTS

LIST OF FIGURES

LIST OF TABLES

NOTATION

Style

$\mathbf{a}$	A vector or matrix
a	The scalar magnitude of vector **a**
$\hat{\mathbf{a}}$	A unit vector in the direction of vector **a**
$\dot{\mathbf{a}}$	The first time-derivative of vector **a**
$\ddot{\mathbf{a}}$	The second time-derivative of vector **a**
$\mathbf{a}'$	Vector **a** prior to a rotation
$\mathbf{r}$	Vector representation in global coordinates
$\mathbf{s}$	Vector representation in local coordinates
$\mathbf{c}$	Pitch link or actuator vector representation

Subscripts

i	An index, typically the number of the blade
k, n	Other index subscripts
g	Denotes a variable pertaining to gusts, or the disturbances
top	Upper (top) swashplate
bot	Lower (bottom) swashplate
$section$	Blade section number
sp	Swashplate
PL	Pitch link
A	Actuator

w	Wear
N	Normal, as in normal force
b	Blade
long	Longitudinal
lat	Lateral
col	Collective
ped	Pedal
v	Vehicle
HHC	Higher Harmonic Control
IBC	Individual Blade Control
T1	First Torsion Mode

Symbols

TEF	Trailing Edge Flap
AWC	Airwake Compensator
CFD	Computational Fluid Dynamics
$\mathbf{x}$	System state vector
$\mathbf{u}$	Control vector
$\mathbf{w}$	Disturbance Vector
$\mathbf{A}$	State Matrix
$\mathbf{B}$	Input Matrix
$\mathbf{G}$	Gust, or disturbance, matrix
u_v	Vehicle longitudinal translational rate
v_v	Vehicle lateral translational rate
w_v	Vehicle vertical translational rate

p_v	Vehicle roll rate
q_v	Vehicle pitch rate
r_v	Vehicle yaw rate
ϕ_v	Vehicle roll angle
θ_v	Vehicle pitch angle
ψ_v	Vehicle yaw angle
u_g	Vehicle longitudinal translational rate disturbance
v_g	Vehicle lateral translational rate disturbance
w_g	Vehicle vertical translational rate disturbance
p_g	Vehicle roll rate disturbance
q_g	Vehicle pitch rate disturbance
r_g	Vehicle yaw rate disturbance
δ_{lat}	Swashplate AWC lateral cyclic control input
δ_{long}	Swashplate AWC longitudinal cyclic control input
δ_{col}	Swashplate AWC collective control input
δ_{ped}	Swashplate AWC tail rotor collective control input
$\mathbf{T}_{zd}(s)$	Transfer function from the disturbance vector to performance variables
$\left\|\mathbf{T}_{zd}(s)\right\|_2$	H_2 norm of the transfer function $\mathbf{T}_{zd}(s)$
$\left\|\mathbf{T}_{zd}(s)\right\|_\infty$	H_∞ norm of the transfer function $\mathbf{T}_{zd}(s)$
ω	Angular rate
δ_f^i	ith blade's TEF deflection angle, positive down
δ_0	TEF collective pitch

δ_{1C}	TEF lateral pitch
δ_2	TEF reactionless pitch (disk warping pitch)
ψ	Azimuthal angle
$\mathbf{q}$	Generalized coordinate vector
$\mathbf{\Phi}$	Constraint vector
$\mathbf{J}$	Jacobian matrix
$\mathbf{r}_k$	Global vector to the local origin on link *k*
$\mathbf{r}_k^A$	Global vector to point *A* on link *k*
$\mathbf{s}_k^A$	Local vector to point *A* on link *k*
$\mathbf{R}_k$	Transformation matrix from link *k*’s local coordinates to global
$\boldsymbol{\nu}$	Velocity right-hand-side vector
$\boldsymbol{\gamma}$	Acceleration right-hand-side
$x_k{}^P$	*x*-component of the local vector to point *P* on link *k*
$\mathbf{M}_k$	Link *k* translational and centroidal rotational inertia matrix
$\mathbf{t}_k$	Link *k* translational and rotational velocity vector
$\mathbf{W}_k$	Link *k* angular velocity matrix
$\mathbf{w}_k$	Link *k* applied force and torque vector
n	Number of links in a mechanism
m	Mobility of mechanism
j_k	Number of joints in a mechanism that allow *k* degrees of freedom
$\mathbf{E}_3$	Unit vector pointing along rotor shaft
$\mathbf{E}_1$	Unit vector pointing to the right of the helicopter, perpendicular to $\mathbf{E}_3$

$\mathbf{E}_2$	Unit vector pointing to the front of the helicopter, perpendicular to $\mathbf{E}_3$
ψ_{bi}	Azimuthal angle of blade *i*
ε	Pitch link lead angle—the azimuthal angle between a blade and its pitch link's connection to the swashplate
N_b	Number of blades
Ω	Rotor rotation rate
R	Rotor radius
c	Blade chord length
θ_i	Total pitch of blade *i* at 75% rotor radius
θ_{1C}	Lateral cyclic pitch
θ_{1S}	Longitudinal cyclic pitch
θ_0	Collective pitch
θ_{cyc}	Total cyclic component of pitch
θ_{col}	Collective component of blade pitch at 75% rotor radius
θ_{twist}	Difference in built-in pitch from blade root to 75% rotor radius
$\{\mathbf{x}_i, \mathbf{y}_i, \mathbf{z}_i\}$	Local coordinate axes of blade *i*
$\mathbf{r}_b$	Vector from the swashplate center to a blade's pitch bearing's center
$\mathbf{r}_h$	Vector from a blade's pitch bearing center to the corresponding pitch link's upper rod eye center
$\mathbf{r}_p$	Vector from the swashplate center to the pitch link's lower rod eye center
z_{col}	Vertical displacement of the swashplate
$\mathbf{c}_{PL}$	Vector representing the pitch link

$\mathbf{a}_1$	Unit parallel to the $\mathbf{E}_1$-$\mathbf{E}_2$ plane in the azimuthal direction of the pitch connection to the upper swashplate
$\mathbf{a}_2$	Unit vector $\mathbf{a}_1$ rotated by ninety degrees in azimuth
η	Angle of $\mathbf{r}_\mathrm{p}$ with $\mathbf{a}_1$-$\mathbf{a}_2$ plane
ψ_p	Azimuthal angle of $\mathbf{r}_\mathrm{p}$
φ_{sp}	Swashplate roll angle
θ_{sp}	Swashplate pitch angle
$\mathbf{R}_{sp}$	Lower swashplate rotation matrix
$\{\mathbf{e}_1,\mathbf{e}_2,\mathbf{e}_3\}$	Bottom swashplate local frame basis vectors
$\mathbf{n}$	Swashplate normal vector
$\mathbf{r}_{base}$	Vector from the global origin to an actuator base
$\mathbf{r}_A$	Vector from the swashplate center to the connection between an actuator and the lower swashplate
$\mathbf{c}_A$	Vector representing an actuator
M_θ	Blade section aerodynamic moment
I_θ	Blade angular moment of inertia per unit length about the feathering axis
I_0	Blade angular moment of inertia per unit length about the chordwise center of mass
m_0	Blade mass per unit length
x_I	Blade chordwise center of mass offset
k_r	Torsional root spring stiffness
$\mathbf{F}_{PL}$	Pitch link force vector

$I_{f,\mathrm{section}}$	Blade section angular moment of inertia about the feathering axis
M_a	Total blade aerodynamic moment
m_{sp}	Swashplate mass (upper and lower combined)
r_{sp}	Swashplate effective radius
$\mathbf{I}_{sp}$	Swashplate angular inertia matrix
$\mathbf{F}_A$	Actuator force vector
$\boldsymbol{\alpha}$	Angular acceleration vector
$\boldsymbol{\omega}$	Angular velocity vector
D	Damage
σ_k	Cyclic stress level
n_k	Number of cycles at stress level σ_k
N_k	Number of cycles to failure at stress level σ_k
V_w	Wear volume
k_w	Wear coefficient
F_N	Normal force
L	Travel distance
H	Material hardness
P	Per revolution
$\theta_{HHC,i}$	Higher Harmonic Control (HHC) component of the pitch of blade i
A_k	HHC cyclic amplitude
θ_k	HHC collective amplitude

ϕ_{HHC}	HHC control phase angle
$\theta_{IBC,i}$	IBC component of the pitch of blade *i*
ω_{T1}	Blade first torsional frequency

ACKNOWLEDGEMENTS

This project was supported by Lord Corporation, by the Office of Naval Research, grant number N00014-06-0205, and by the Applied Research Laboratory at the Pennsylvania State University Exploratory and Foundational Program. Without this support, the project would not have been possible.

I thank my advisors for all the help they have given me in pursuit of knowledge and my degree. Dr. Rahn has helped me navigate out of several situations where I was thinking in circles, Dr. Smith helped me to see the big picture, and Dr. Conlon provided fresh insight and pointed questions. Thank you for all of your help—you were an integral part of my education. I also thank Dr. Sommer for giving me permission to use some computer code he had written, saving me from recreating work already performed and vetted. Kirk Frederickson from Sikorsky also greatly helped me by obtaining helicopter parameters for my work, for which I am grateful.

Thanks to my fellow graduate students are also in order. Thank you, Lloyd Scarborough, Conor Marr, Pam Montanye, Chris Cormier, and Mihir Mistry for listening to me talk about research, even if I was rambling, and for lending me your thoughts. Thank you also for helping to make my graduate experience enjoyable.

I thank my parents and grandparents for supporting me in all of my endeavors. To my parents, without your hard work and love, I would not be the man I am today. To my grandparents, you helped to make me feel at home. Finally, I thank God that I have had the opportunity to freely pursue an advanced education—an opportunity so many others do not have even though they wish it.

Chapter 1

Introduction

1.1 Background

Helicopters have become extremely versatile in military and civil applications, including use for combat, for search and rescue, as ambulances, for fire fighting, for reconnaissance, and for transportation. Vertical flight ability enables a helicopter to operate from small landing zones, from close quarters on ships, and to hover over areas where landing is not possible, such as at sea during rescue missions. These same environments where the helicopter is the most able aircraft to perform the needed task, such as operation from a ship, unfortunately remain the most challenging and dangerous for the helicopter pilot, passengers, and the helicopter. Operations between a ship and a helicopter such as landing, station-keeping, and take-off, known as dynamic interface (DI) operations, present a difficult work environment for helicopter pilots because of the precision involved in matching the roll and pitch of the helicopter to that of the ship and the unsteady airwake generated by the ship deck and superstructure [1, 2]. Moreover, helicopter vibrations, especially over extended missions, increase the chances of pilot fatigue, increasing the difficulty of performing high-concentration tasks [3].

There are currently two ways to mitigate the risk of pilot error due to high workload and fatigue during DI tasks: (1) preventing the pilot from taking-off or landing in adverse conditions and (2) automatically compensating for conditions which increase pilot workload or fatigue. The first method is currently implemented in Wind-over-Deck (WOD) envelopes, or Ship-Helicopter Operating Limits (SHOL) in the U.K., Canada, and Australia, which limit the wind-ship conditions in which DI operations are allowed. Each WOD envelope consists of a maximum wind speed for each direction relative to the ship as shown in Figure 1.1. These envelopes are landing spot and approach specific because ships may have multiple landing spots with different airwake severities. Other shipboard hazards, such as nearby superstructure, also increase the difficulty of landing and will therefore affect the WOD envelope.

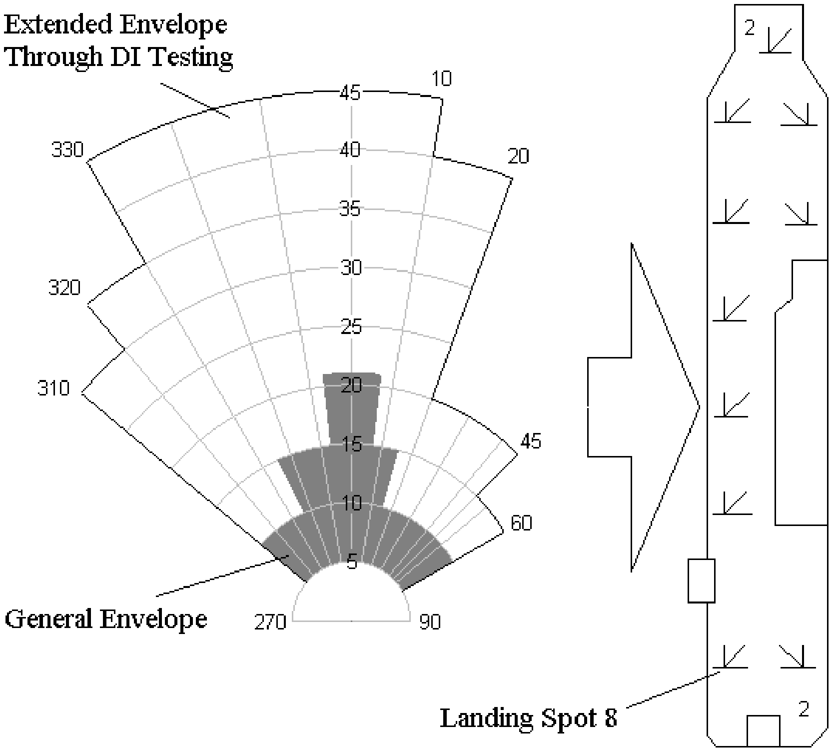

Figure 1.1: An Example WOD Envelope, Specific to a Landing Spot on a Ship [4].

The general WOD envelop, as shown in Figure 1.1, often restricts helicopters from operating in conditions in which they are quite capable. DI tests are performed to extend the envelope, and thus the operational capabilities. These tests are expensive because they require the coordination of a ship and a helicopter, and the wind conditions that are desired must be present to test the interface. Computer simulations have been developed to predict pilot workload in various airwakes in an effort to circumvent the high costs of DI testing [1, 2].

The second method of mitigating pilot workload and fatigue is to alleviate the conditions that increase workload and fatigue. This solution uses existing flight controls to augment helicopter response if the required actuations are within system capabilities, or it can be accomplished by using additional flight controls that would require modifications to the helicopter hardware as well as the avionics.

1.2 Helicopter Flight Control

1.2.1 The Swashplate Mechanism

Conventional helicopters control their main rotor blades' pitches by means of a swashplate mechanism, as shown in the picture and Computer Aided Drafting, or CAD, model of Figure 1.2. The swashplate mechanism consists of at least three servos, or actuators, a lower swashplate, an upper swashplate, and a pitch link for every blade that connects the upper swashplate to the pitch horn of the blade. The lower swashplate can move vertically along the shaft that rotates the rotor and can tilt in any direction with respect to the helicopter, but it does not rotate with the rotor. A bearing mates the upper swashplate with this lower plate so that the upper swashplate will move with the lower, but will also rotate with the rotor. Typically, a pair of scissors, shown in Figure 1.2a, that have one link connected to the rotating hub and one to the upper swashplate, maintains the rotation of the upper swashplate. The upper swashplate is connected to each blade's pitch horn through a pitch link. When referring to the swashplate mechanism in this paper, "the swashplate" denotes both upper and lower swashplates combined, unless explicitly stated otherwise.

When the three servos travel in unison, the result is no change in the tilt angle of the swashplate. All blade root pitch angles increase or decrease by the same amount through action of the pitch links on the pitch horns as they follow the motion of the top swashplate. This is called

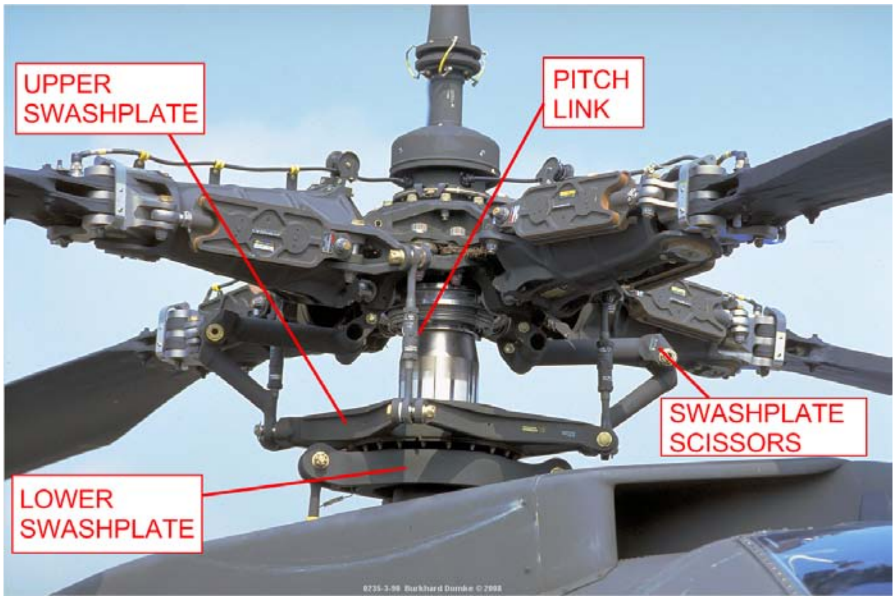

Figure 1.2a: An AH-64 Rotorhead [5].

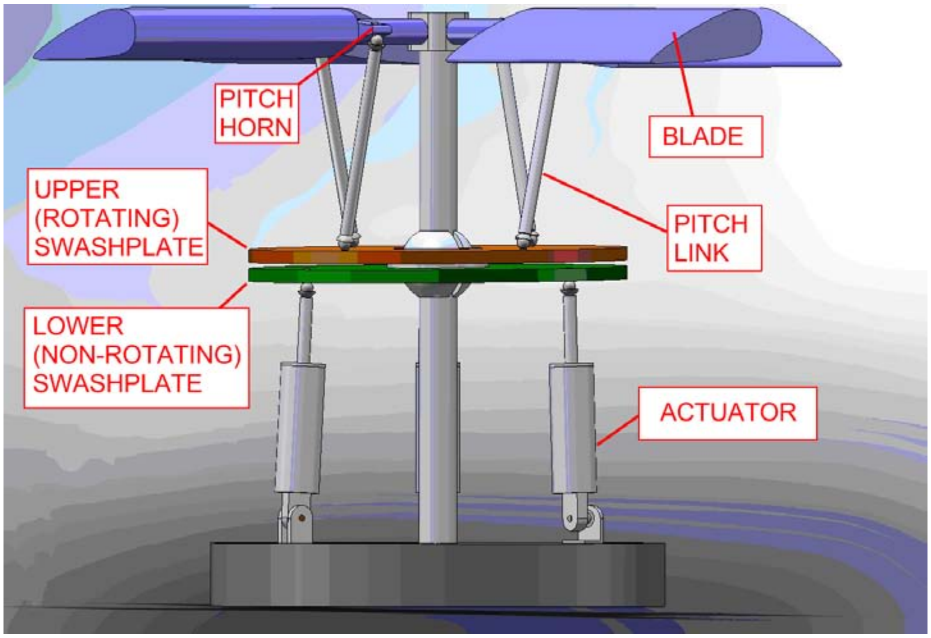

Figure1.2b: A CAD model of an example swashplate.

Figure 1.2: Swashplate Mechanisms.

collective pitch, and increasing the angle of attack of all of the blades increases the rotor thrust. If the swashplate servos move by different amounts, this imparts a cyclic pitch on each blade because the pitch links move up and down as they revolve about the center on the now-inclined plane of the swashplate. As they rotate with the rotor, the blades pitch up and down from cyclic action of the pitch link. This pitching produces blade flapping, lagging ninety degrees out of phase with the pitch input. For example, if the swashplate is tilted such that the right side of the plate is lower than the left, then the blades on a counter-clockwise rotating rotor (as viewed from above) with pitch links preceding the blades flap down toward the front of the helicopter and up toward the rear. This cyclic pitching of the blades tilts the rotor thrust vector, which allows control of the helicopter with aid from tail rotor for anti-torque and yaw control.

1.2.2 An Active Rotor

A different method of flight control is accomplished by placing the actuation in the rotating frame—on the rotor. This approach, called individual blade control (IBC), is a form of an active rotor. An active rotor is one that operates at higher frequencies than needed for primary control. Active rotors can be controlled by a number of methods, including root pitch control, active blade twist, gurney flaps, and trailing-edge flaps. These methods work, in principle, the same way as a swashplate for primary flight control in that they change the rotor azimuthal lift distribution to tilt the thrust vector. None of these methods are currently implemented on a production helicopter for primary flight control. Some may not even have the authority for primary flight control, but all do show promise for reducing vibrations, exterior noise, and required rotor power. The distinguishing trait between IBC and a rotor actuated solely by the swashplate mechanism is the possibility in IBC of controlling each blade individually with no constraints imposed by the swashplate.

While no production helicopters to date have incorporated IBC, Kaman Corporation, headquartered in Connecticut, makes production helicopters similar to ones with on-blade actuation. Kaman employs a servoflap design in which each blade has a trailing control flap, but one that is not necessarily integrated into the blade itself. This flap, when pitched, imparts a moment on the blade which either twists the blade or pitches the blade on a torsionally soft root spring. This control is not IBC because the servoflaps are actuated by cables which are controlled by a swashplate, albeit one that requires much smaller actuation forces than a conventional swashplate and, therefore, weighs less. Figure 1.3 shows a helicopter with servoflaps.

Figure 1.3: A SH-2 Seasprite with Servoflaps. [6]

1.3 Alleviating Helicopter Gust Response

In an effort to understand the complexities of helicopter-ship interaction, a program called the Joint Shipboard Helicopter Integration Process (JSHIP) was established [4, 7]. The JSHIP program focused on non-naval helicopters landing on Navy ships. As part of this program, the Dynamic Interface Modeling and Simulation System (DIMSS) sought to develop WOD envelopes without the expense and difficulty of real helicopter-ship testing. The program developed a simulation of a Sikorsky UH-60 Blackhawk landing on a LHA-class ship. The ship airwake simulation was validated by placing anemometers on a LHA deck and comparing the readings to the simulation of the same conditions. Similar validation was performed by comparing simulator helicopter response to real at-sea test data for maneuvers adapted from ADS-33D. After validation, testing for WOD envelopes using a man-in-the-loop simulation in the NASA Ames Vertical Motion Simulator concluded that landing spot 8 (see Figure 1.1) in a 30 degrees, 30 knots WOD condition required unacceptably high pilot workload. This DI configuration scored a 4 out of 5 on the Deck Interface Pilot Effort Scale (DIPES), with scores of 4 and 5 denoting unacceptable conditions.

1.3.1 Swashplate-Based Gust Rejection

As the primary method of rotor control for conventional helicopters, the swashplate has been viewed as the logical actuation mechanism for gust alleviation. Horn, Bridges, and Lee [8] developed a flight controller that used the swashplate for rotor control to reject shipboard gusts. This controller was designed around the airwake properties of the 30 degrees, 30 knots WOD condition found, in Reference [7], to have unacceptably high pilot workload levels for the UH-60 performing DI operations at landing spot 8 on an LHA-class ship. An H_∞ robust controller was developed that incorporated spectral properties of the airwake into the controller synthesis in order to reject gusts.

To incorporate the airwake into the controller design, Horn *et al*. [8] used the GENHEL-PSU simulation code. GENHEL-PSU is a modified version of U.S. Army/NASA Ames FORTRAN-based computer simulation code of the UH-60 Blackhawk called GENHEL. In the simulation, the UH-60 was made to hover over landing spot 8 in the 30 degrees, 30 knot WOD condition, while aircraft states, state derivatives, and control inputs were recorded. The hover condition over landing spot 8 was maintained by an Optimal Control Model (OCM) of a human pilot developed in other studies [1, 9]. Next, the researchers extracted a simple 9-state linear model of the aircraft as shown below:

$$\begin{aligned}
&\dot{\mathbf{x}} = \mathbf{Ax} + \mathbf{Bu} + \mathbf{Gw} \\
&\mathbf{x} = \begin{bmatrix} u_v & v_v & w_v & p_v & q_v & r_v & \phi_v & \theta_v & \psi_v \end{bmatrix} \\
&\mathbf{u} = \begin{bmatrix} \delta_{lat} & \delta_{long} & \delta_{col} & \delta_{ped} \end{bmatrix} \\
&\mathbf{w} = \begin{bmatrix} u_g & v_g & w_g & p_g & q_g & r_g \end{bmatrix}
\end{aligned} \tag{1.1}$$

In this model, **x(t)** is the helicopter state vector comprised of vehicular translational and angular rates as well as angular orientations, **u(t)** is the control vector of equivalent pilot stick deflections, and **w(t)** is the disturbance vector of equivalent gusts—the gusts in terms of the effect on the aircraft.

This model was then inverted to find the equivalent gusts. Because **G** is a 9 x 6 matrix, and is therefore not square, the study took the least-squares approximation for the vector **w** using the pseudo-inverse as shown below:

$$\mathbf{w} = \mathbf{G}^{+}\left(\dot{\mathbf{x}} - \mathbf{Ax} - \mathbf{Bu}\right). \tag{1.2}$$

Next, spectral filters, or transfer functions, were derived using a least-squares approximation. These filters match the Power Spectral Density (PSD) of the disturbance vector when excited by a zero mean unity white noise signal. Figure 1.4 shows one of the gust filters derived using this method.

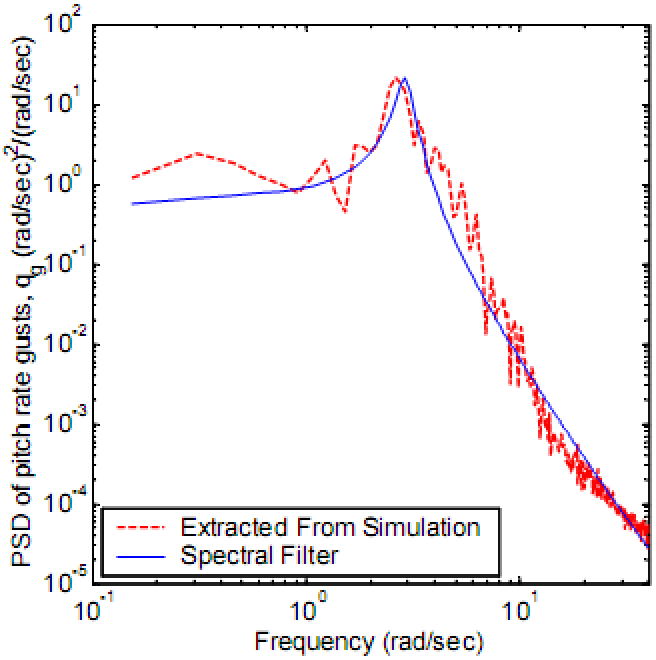

Figure 1.4: PSD of Pitch Rate Disturbances. [8]

Once the gusts were modeled in this way, control synthesis could begin. The study opted for a Multiple Input, Multiple Output (MIMO) control architecture for the Stability Augmentation System (SAS). Figure 1.5 shows a block diagram of the augmented plant model.

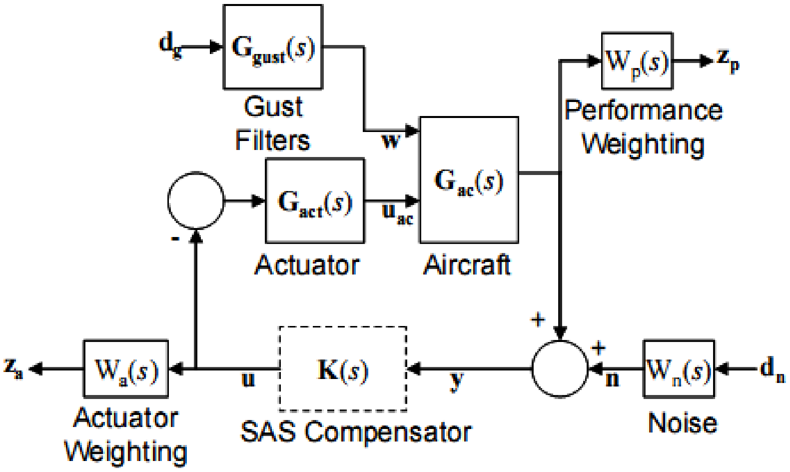

Figure 1.5: Augmented Plant Model in Reference [8].

Horn *et al.* created H_2 and H_∞ controllers using this model, as well as a reduced-order SAS from the H_2 controller. Robust control attempts to find compensator values, **K(s)**, that will satisfy a performance criterion. For H_2 synthesis, the goal is to minimize the H_2 norm,

$$\left\|\mathbf{T}_{zd}(s)\right\|_2 = \sqrt{\frac{1}{2\pi}\int_{-\infty}^{\infty} tr\left\{\mathbf{T}_{zd}(j\omega)^* \mathbf{T}_{zd}(j\omega)\right\} d\omega}\,, \tag{1.3}$$

and for H_∞ synthesis, the goal is to constrain the maximum singular value of the closed-loop system:

$$\left\|\mathbf{T}_{zd}(s)\right\|_\infty = \sup_{\omega} \overline{\sigma}\left[\mathbf{T}_{zd}(j\omega)\right] < \gamma\,, \tag{1.4}$$

where $\mathbf{T}_{zd}$ is the transfer function relating disturbances to performance variables.

Results showed that all controllers designed rejected gusts to some degree when tested in the GENHEL simulation program, with the H_∞ controller showing the largest decrease in vehicle angular rates. The performance of the modified SAS derived from the H_2 controller using model order reduction proved comparable to that of the H_2 controller, itself.

The modified SAS in Reference [8] altered pilot commands in certain frequencies as a consequence of the controller architecture. To resolve this, Horn and Bridges [10] employed the Model Following Controller (MFC) architecture shown in Figure 1.6. If there are no disturbances or inversion errors, the MFC design achieves the desired response without the need of feedback. Also, the Airwake Compensator (AWC) can be scheduled for different gust conditions or turned off entirely if it is not desired. Moreover, this architecture ensures that the AWC has no effect if the controller is already tracking pilot commands.

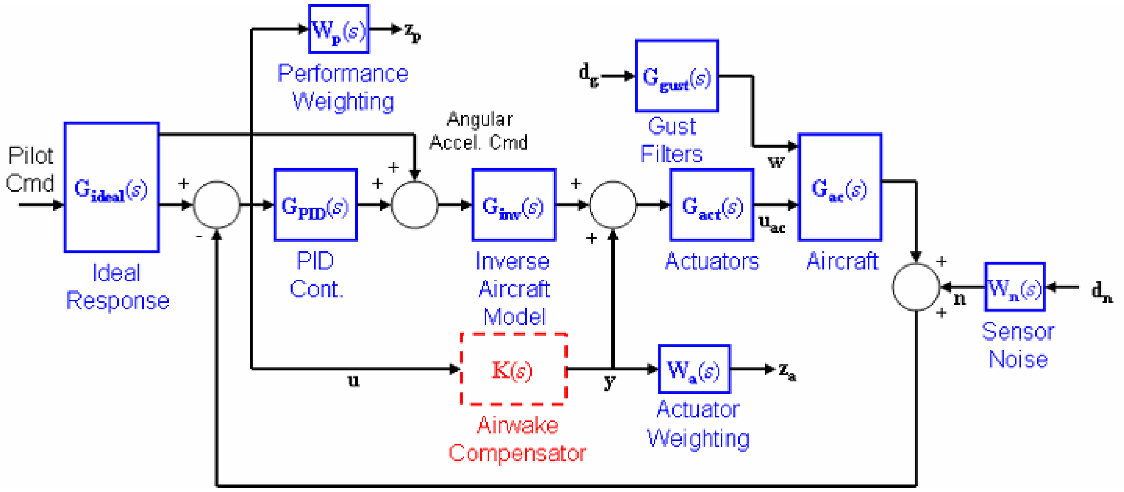

Figure 1.6: Augmented Plant Model with Model Following Controller Architecture. [10]

The AWC design process used the same methodology as had been employed for the robust H_2 controller synthesis in Reference [8]. This created a high order compensator, which was then reduced in order by first removing the low frequency poles and an equal number of zeros. Further model order reduction was performed after this, resulting in an AWC with 30 states. This AWC was implemented in GENHEL, and once again used the OCM of the pilot to provide commands in order to maintain position. This final controller reduced helicopter rate response to gusts by up to 90%.

1.3.2 Trailing Edge Flap-Based Gust Rejection

The works cited previously [8, 10] used the swashplate to control the rotor for helicopter shipboard gust rejection, as can be seen by examining the control vector, **u**, in Equation 1.1. Montanye [11] used an active rotor approach where each blade on the rotor was model to have a trailing edge flap (TEF). TEFs, unlike the servoflaps in Figure 1.3, are integral to the blade—that is, each flap spans a portion of the chord of the blade. Figure 1.7 shows a blade with a trailing edge flap.

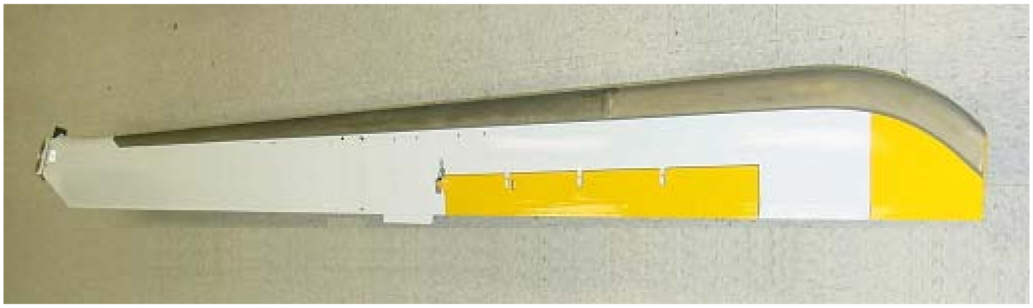

Figure 1.7: The SMART Rotor Blade with a Trailing Edge Flap. [12]

TEFs have been examined for use on helicopters for vibration control [44-46], for exterior noise reduction [55], and for rotor performance enhancement [63]. TEFs, and IBC rotors in general, have the potential to reduce helicopter weight by removing or reducing the size of traditional primary actuators, reduce parasitic drag by removing the swashplate mechanism, and physically decouple secondary control from primary control. Montanye investigated TEFs for use in gust rejection, while the primary flight control remained the duty of the swashplate. These flaps were designed to be lift flaps instead of moment flaps. Lift flaps impart a change in the airfoil section coefficient of lift, but are not expected to pitch the entire blade, as do the servoflaps as used by Kaman. This limited the authority of the flaps because they were not used for pitching the entire blade, but it was appropriate the UH-60 rotor used in the study, which has torsionally rigid blades. Neither the flap drag nor the flap pitching moment was modeled.

Before designing a controller for gust rejection, Montanye conducted an authority analysis to determine what size TEF was needed to produce the control moments required to reject shipboard gusts. First, a quasi-steady aerodynamic model was derived for the flaps and implemented in GENHEL for the UH-60. Next, a GENHEL simulation was run in which the rotor had no flaps, the helicopter body was constrained so that it would not move, and cyclic pitch inputs were fed to the swashplate so that the resulting moments on the constrained body could be recorded. The flaps were sized so that, with a 3 degree, once per revolution cyclic pitch, they could create the same maximum hub moments as were required for gust rejection from the swashplate-based AWC [10].

After sizing the flaps, controller design followed the same route taken by Horn and Bridges [10] for an H_2 robust controller, except that instead of stick deflections, the AWC only outputted trailing edge flap commands that mimic stick commands,

$$\delta_f^i = \delta_0 + \delta_{1C}\cos(\psi_i) + \delta_{1S}\sin(\psi_i) + \delta_2(-1)^i \,, \tag{1.5}$$

where i is blade number and ψ_i is the azimuth of blade i. This decomposed each flap pitch (δ_f^i) to a collective flap pitch (δ_0), a lateral cyclic flap pitch (δ_{1C}), a longitudinal flap pitch (δ_{1S}), and a flap pitch from the reactionless mode (δ_2). In this controller, then, true IBC was not realized since the TEF pitches are interdependent.

An actuator weighting function matrix was chosen so that actuation of the flaps over 10 radians per second was penalized in the control synthesis. The yaw axis was uncontrolled with respect to the AWC and the pitch axis was given three-fourths the weight of the roll axis in the controller design to reduce the likelihood of the flaps actuating to saturation.

Figure 1.8 shows the performance of both the swashplate-based AWC and the TEF-based AWC. The reductions in rates in the pitch and roll axes are similar, and the difference in the yaw axis is because yaw was not controlled with the TEF-based controller.

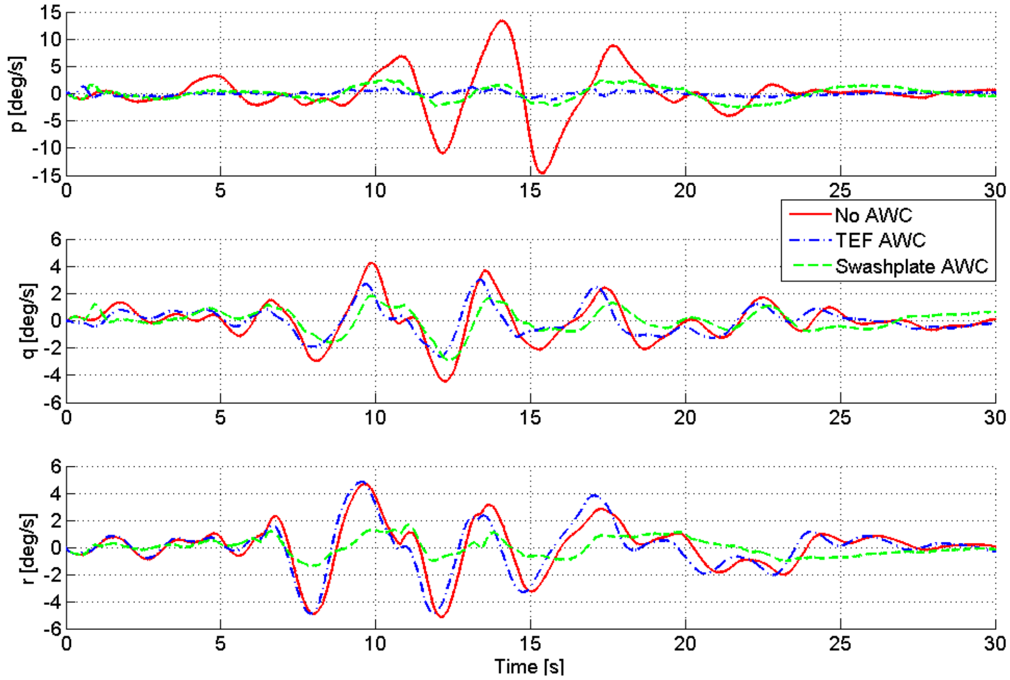

Figure 1.8: Swashplate versus TEF Gust Rejection. [11]

Figure 1.8 shows that the controllers performed similarly in roll and pitch, so the results beg the question: what makes one method better than the other? To help answer which is better, the kinematics and dynamics of the primary flight actuators are modeled to find a comparison on the actuator level.

1.4 Modeling the Swashplate and Servos

1.4.1 Mechanism Modeling

Comparing the results from the two different AWCs requires modeling the relationship between blade pitches and the actuator displacements and forces. The varied approaches for multi-body kinematic and dynamic modeling are reviewed here.

Haug [13] developed a method called the Dynamic Analysis and Design System, or DADS. This method creates a set of Differential-Algebraic Equations (DAE) for the system. First, a vector of generalized coordinates, **q**, is established. This vector consists of angles and positions of the mechanisms' bodies' center of masses in global coordinates. Next, a constraint vector, **Φ**, is formed that consists of a column vector of the constraint equations that individually are either vector or scalar equations. This constraint vector is generally ordered such that kinematic constraints, or those related to a joint, appear first, and then the driver constraints, or those that specify motion, appear last. For example, for the planar four-bar linkage shown in Figure 1.9 there would be a vector **q** of length 9 because the three links capable of moving would each have one angle of rotation and two positions within the plane. A constraint for one of the revolute joints would be that the local vector pointing to point B on link 2 would have the same global coordinates as the local vector pointing to point B on link 3. A constraint equation sufficient for describing this revolute in the planar case would be,

$$\mathbf{r}_3^B - \mathbf{r}_2^B = \left(\mathbf{r}_3^{CG} + \mathbf{R}_3\mathbf{s}_3^B\right) - \left(\mathbf{r}_2^{CG} + \mathbf{R}_2\mathbf{s}_2^B\right) = 0, \tag{1.6}$$

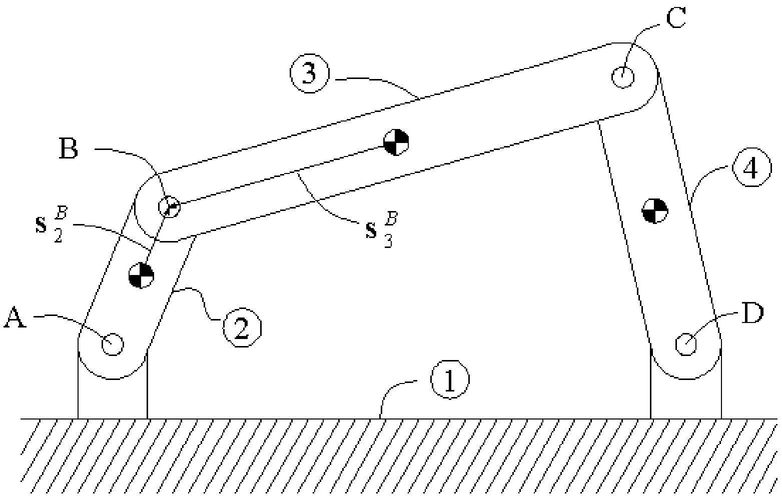

Figure 1.9: An Example Four-Bar Linkage.

where any vector $\mathbf{s}_k^P$ is the vector in local coordinates from the center of gravity of link *k* to point P on link *k*, a vector $\mathbf{r}_k^P$ is the vector in global coordinates from the global origin to point P on link *k*, a vector $\mathbf{r}_k^{CG}$ is the global vector to the center of gravity (CG) of link *k*, and $\mathbf{R}_k$ is the rotational transformation matrix that acts on vectors in link *k* local coordinates and returns the vector representation in global coordinates.

After defining all constraint equations, including driving constraints, the Jacobian for the system is generated by taking the partial derivatives of the constraint vector with respect to each of the generalized coordinates. The Jacobian is used to evaluate where the mechanism is indeterminate, to estimate generalized coordinates via the Newton-Raphson method, and to determine the derivatives of the generalized coordinates via multiplication of the Jacobian's inverse with the velocity right-hand-side, $\boldsymbol{\nu}$, or the acceleration right-hand-side, $\boldsymbol{\gamma}$, as appropriate. These two vectors, $\boldsymbol{\nu}$ and $\boldsymbol{\gamma}$, are derived from the constraint equations in Appendix A. The derivatives of the generalized coordinates can then be used to calculate forces using a Newtonian approach if dynamic behavior needs to be examined.

Haug’s method can be applied to 2-D and 3-D mechanisms quite effectively. It can systematically deal with a mechanism of any number of links, and it has the advantage of being capable of both forward and inverse kinematics and dynamics. In this thesis, forward dynamics denotes knowing the positions and forces of some links or actuators and finding the resulting motions of the end effector, which in the case of the swashplate mechanism would be the blade pitches. Inverse kinematics indicates utilizing knowledge of the end effector motion to find the motion of the actuators and inverse dynamics involves finding the forces required in those actuators to achieve the end effector motion.

Chace [14] developed another method of kinematic and dynamic analysis. Chace’s vector method solves the position analysis problem by treating every link as a vector. The constraints are built-in, so that some vectors are known entirely, while others have an unknown magnitude or direction, or both. Take, for example, a two-dimensional case. In a plane, any determinate n-vector polygon can be reduced to a vector triangle, where one vector-side is the sum of the n-2 known vectors, and the other two vectors in the triangle may contain unknowns (see Figure 1.10). Since a triangle is a loop, and a loop originates and terminates at a single point, the triangle can be written as the vector sum:

$$\mathbf{C} + \mathbf{s} + \mathbf{t} = \mathbf{0} \ . \tag{1.7}$$

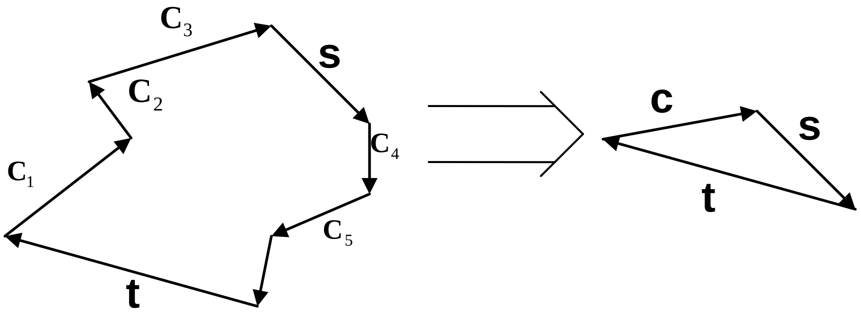

Figure 1.10: Reduction of a Vector Polygon to a Vector Triangle

That vector sum can then be rewritten in magnitude-direction form as,

$$C\hat{\mathbf{C}} + s\hat{\mathbf{s}} + t\hat{\mathbf{t}} = 0\,, \tag{1.8}$$

where for some vector **a**, **â** denotes a unit vector in the direction of **a** and *a* denotes the magnitude of **a**. The above form clearly shows how much information the previous equation contains: there are three magnitudes and three directions. Because it is a vector equation, it may contain two unknowns and still be soluble. There are six possible combinations, since we know that **C** is known. These combinations are: $s, \hat{\mathbf{s}}; t, \hat{\mathbf{t}}; s, t; \hat{\mathbf{s}}, \hat{\mathbf{t}}; s, \hat{\mathbf{t}}; t, \hat{\mathbf{s}}$. From these six, there are only four unique cases, mathematically, since the combinations of unknowns $s, \hat{\mathbf{s}}$ and $t, \hat{\mathbf{t}}$ are the same, and $s, \hat{\mathbf{t}}$ and $t, \hat{\mathbf{s}}$ are the same. For the first two cases, a complete vector is unknown and for the second two cases, a magnitude of one vector and a direction of another are unknown. See Appendix A for solutions to the vector polygon equations.

In three dimensions, the vector polygon equation becomes the vector tetrahedron equation,

$$\mathbf{C} + \mathbf{s} + \mathbf{t} + \mathbf{r} = \mathbf{0}\,, \tag{1.9}$$

where each of the four vectors is an edge of a tetrahedron. Because the vectors have three scalar components each, the equation can have up to three unknowns and still be solved. Like the vector polygon equation, this equation also has a set number of cases that have solutions. There are nine solvable cases, in which the unknowns may be the orientation angles of a vector (in spherical coordinates) or the length of a vector. Each of the generalized solutions is obtained by solving a polynomial [15].

Finally, once a position solution for a linkage is obtained using the generalized solutions, the velocities and accelerations of the joints and links are found by taking the first and second time derivatives of the position vectors. Vector dynamics are then applied using a Newtonian approach to solve for forces [14]. See Appendix A for further description of the method.

1.4.2 Swashplate Models

The swashplate, in particular, has been the subject of previous kinematic and dynamic modeling. The swashplate can be viewed as a type of parallel robot [16] with the swashplate acting as the end-effector.

Saffarian and Fahimi [17] and Kim and Ti1bury [19] investigated the kinematic behavior of the swashplate of a radio-controlled (RC) helicopter with two blades and a fly-bar. The fly bar mechanism complicates the analysis of the control mechanism, but it is necessary for stability and control of an RC helicopter. Kim and Tilbury developed a model of the entire helicopter, including swashplate and fly-bar kinematics and helicopter aerodynamics and dynamics. The swashplate model used, however, was a simplified model relating swashplate angles to blade cyclic pitch. Saffarian and Fahimi developed a more complete kinematic model of the swashplate by implementing an augmented matrix method for transformations similar to the one described by Denavit and Hartenberg [18]. The transformation matrix for a vector from local to global coordinates consisted of the 3x3 rotation tensor, **R**, incorporated into a 4x4 matrix,

$$\mathbf{T} = \begin{bmatrix} \mathbf{R}_{3x3} & \mathbf{r}_{k,3x1} \\ 0_{1x3} & 1 \end{bmatrix}, \tag{1.10}$$

where $\mathbf{r}_{\boldsymbol{k}}$ is the position vector from the global origin to the local origin on link *k* in global coordinates. This transformation matrix then multiplied augmented local position vectors of the form,

$$\mathbf{s}_k^{\ P} = \begin{bmatrix} x_k^{\ P} & y_k^{\ P} & z_k^{\ P} & 1 \end{bmatrix}^T, \tag{1.11}$$

(where *k* is the number of the link and *P* is the terminal point of the vector) to give the global augmented vector to point *P*.

Once the global position vector was found for a joint on a link, this vector was equated to the global position vector to the same joint from the perspective of another link, just as constraint equations are built using Haug's method. This provided a constraint equation for a spherical joint. For revolute joints, the additional constraints were already incorporated into the transformation matrices by using the single unknown rotation angle in the plane of rotation, and then by making the known transformation from the coordinates of that plane to the global coordinates.

The inverse kinematic relations for swashplate deflections to servo rotations (the servos were rotary arms connected to a push-link instead of linear actuators) for the model RC helicopter were determined. Next, the constraint equations were used to solve for forward kinematics. Nonlinear relations were developed that could be used to solve for the forward kinematics of the mechanism over the range $(-\pi/2, \pi/2)$, where the solution was explicit. Then the upper-loop kinematics were addressed by creating a forward kinematic model relating swashplate deflections to blade pitch. This model, since it was kinematic in nature, did not address the dynamics of the fly-bar, but instead treated the fly-bar flap angle as an input. Finally, all the models were combined to make a simulation of the kinematics of the total mechanism. The results were analyzed with a particular interest in the blade motion output for desired swashplate motion and fly-bar flap angle inputs.

Lange *et al*. [20] analyzed the kinematics, and later the dynamics [21], of the swashplate of the CL-327 Guardian, an unmanned coaxial helicopter. The kinematic analysis of the swashplate was divided into forward and inverse kinematics of the mechanism, and again divided into the rotating frame kinematics and the fixed frame kinematics. Analytical models were generated from a vector-based constraint equation approach. The governing kinematic equations could then be solved using the contour approach. A velocity analysis was also performed on the rotating frame and fixed frame linkages, resulting in a thorough kinematical analysis of the CL-327 Guardian's swashplate.

The dynamic analysis of the CL-327 was based on Newton-Euler equations of the form,

$$\mathbf{M}_k \dot{\mathbf{t}}_k = -\mathbf{W}_k \mathbf{M}_k \mathbf{t}_k + \mathbf{w}_k \,, \tag{1.12}$$

where k is the link number, $\mathbf{M}_k$ is the link translational and centroidal rotational inertia matrix, $\mathbf{W}_k$ is the link angular velocity matrix, $\mathbf{t}_k$ is a vector composed of rotational and translational velocities, and $\mathbf{w}_k$ is the applied force and torque vector, or wrench, which was then decomposed into conservative and non-conservative wrenches. The coordinates for each link were then generalized to form a single vector equation based on the Newton-Euler equation above. Once constraints were enforced, this provided a solution for the inverse dynamics of the system, where the applied loads were the aerodynamic loads on the blades.

In particular for the UH-60, Abhishek, Datta, and Chopra [22] developed a model of the swashplate for the purposes of predicting the effect of swashplate dynamics and blade dynamics on servo loads. By coupling the structural loads model with the swashplate model, and by modeling the servos as spring-dampers, a forward dynamic model of the rotor system was developed which incorporated not only the stiffness of the control system, but also the damping and inertial effects. To do this, the swashplate was modeled as one thin disk rotating with the rotor, and pitching with the control system inputs. The mass of the swashplate was taken into account, but the pitch links and servo rods were not assigned masses. Moreover, the pitch links were assumed to be vertical and perpendicular to the swashplate so that, in the vertical direction, the sum of the pitch link loads equaled the inertial load plus the servo load. The moments generated by the pitch links were always the vertical pitch link force times the radius on the swashplate, regardless of swashplate orientation. While this approximation may be good for small angles, it does not take into account the nonlinear relation between the swashplate angles and position and the blade pitch angles that is imposed by distance constraints within the mechanism. Additionally, the inertia of the non-rotating swashplate was not considered. While this model was designed for the UH-60, it is not useful here because the present interest is to model the inverse kinematics and dynamics of the swashplate mechanism rather than the effect of the swashplate and servos on the rotor.

1.4.3 Wear Concerns

While modeling the swashplate kinematics and dynamics should result in motions and forces of the servos, or actuators, it is not only the displacement, rate, forces, and power required of the actuators that are of interest. The reliability of the mechanism and the actuators is major concern, especially the effect of actuation on the potential for wear in swashplate components. In the swashplate mechanism, sliding contacts that are subject to wear include the hydraulic actuator seals and rods, spherical bearings, such as those in rod eyes, and the sliding contact between the mast and the swashplate.

For example, Williams and Hyncica [25] address some mechanisms of wear for lubricated contacts. According to Williams and Hyncica, there must be a loss of mass for damage to be considered wear. Plastic deformation of a surface is not considered wear. Two and three-body wear are addressed in the study. Of particular importance here is the finding that there is a critical hydrodynamic film thickness where the wear due to particulates (three-body wear) changes from a random pitting mechanism to parallel gouging of one or both sliding surfaces, resulting in a greater potential for material to be lost from the surfaces due to wear. Figure 1.11 is a depiction of the two types of wear. A study examining the effects of the controllers on the swashplate mechanism and servos should take into account these two possibilities for wear when addressing the reliability implications of each controller.

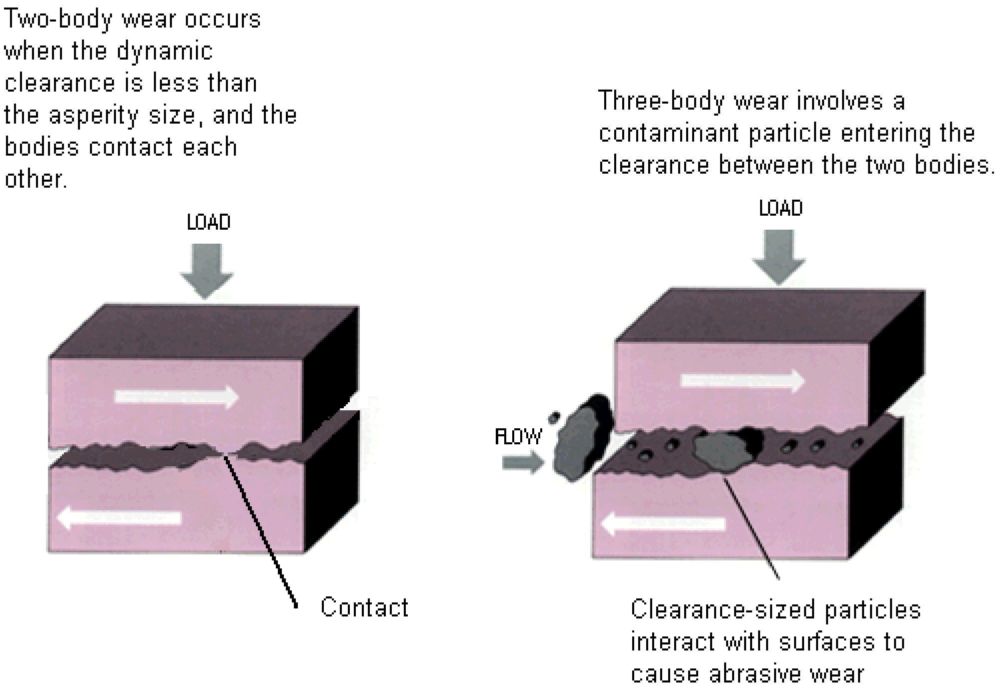

Figure 1.11: Two and Three-Body Wear [67].

1.5 Goals

There are established methods for evaluating the kinematics and dynamics of a swashplate mechanism. None of the references surveyed presented an evaluation of the effects of different gust alleviation methods on the swashplate actuators. Both a swashplate-based AWC and a TEF-based AWC show promising results for reducing workload, so the question of which method is better remains. Additionally, more incentive than gust alleviation alone must exist for modifying a helicopter rotor. Using the rotor for vibration reduction offers another reason for rotor modifications, as well as a method of reducing pilot fatigue caused by vibrations, thus improving safety.

Therefore, this thesis will accomplish the following:

(1) Develop an inverse kinematic and dynamic model of the swashplate mechanism.

(2) Compare the effects of swashplate-based gust alleviation versus TEF-based gust alleviation on the swashplate servos in terms of actuator displacements, forces, rates, fatigue, and wear.

(3) Compare TEF and root pitch IBC for the purposes of helicopter vibration reduction and recommend future areas of investigation.

These goals are accomplished in the following chapters. Chapter 2 details the creation of an inverse kinematic and dynamic model of the swashplate mechanism using a vector approach. The rotor cyclic and collective pitches from previous simulations serve as the starting point from which servo motions are determined. Additionally, rigid blade torsional dynamics and swashplate inertial effects are included in the Newtonian mechanics which dictate the swashplate actuator forces. All other links serve as rigid bodies with no mass.

Chapter 3 describes the motions and forces required of the swashplate actuators for gust alleviation using the swashplate-based controller and the TEF-based controller. A case with no gust alleviation is used as a baseline for the comparison. The actuator travel, stroke length, and number of reversals in each case are compared as wear metrics. Component fatigue is also addressed.

Chapter 4 conducts a literature review of vibration alleviation using TEFs and root pitch IBC. The results from various works and authors are synthesized to determine the better IBC scheme in terms of vibration reduction, performance, and actuator requirements. The results from this review raise further questions regarding actuator capability and performance trade-offs. Future work recommendations attempt to address these questions.

Finally, Chapter 5 presents a brief summary of conclusions of the thesis and recommendations for future work.

Chapter 2

The Swashplate Model

2.1 Mobility Analysis

The GENHEL simulation of the UH-60 in the CFD ship airwake with airwake compensation outputs rotor collective and cyclic states for every simulation time step. In the GENHEL simulation, the swashplate actuators, or servos, are modeled as transfer functions relating mixer inputs to the rotor longitudinal cyclic, lateral cyclic, and collective outputs. In order to compare the actuator behavior, a model relating the cyclic and collective pitches of the rotor to the actual servo displacements and forces is needed. GENHEL does not model the swashplate mechanism, but rather uses functions representative of the entire control system, combining the servos, valves, control mixing, and the swashplate mechanism. In this chapter, a model of the swashplate is developed to address actuator issues.

A mobility analysis can help to gain insight into the kinematics of the mechanism. Considering only the two pairs of scissors necessary to enforce swashplate rotation constraints, the swashplate mechanism for the UH-60’s four-bladed rotor contains four blades, four pitch links, one rotating upper swashplate, one non-rotating lower swashplate, two pairs of scissors, and three hydraulic actuators. The actuators each consist of a fixed cylinder and a moving cylinder rod. The total number of links comes to twenty-two when the helicopter frame and the rotor shaft are included. Figure 2.1 shows the mechanism topology, which illustrates the connectivity of the individual links but not necessarily the shape of the mechanism. Each shape in the figure represents a link in the mechanism. The overlap of two shapes represents a joint, which is denoted by “S”, “R”, “C”, or “S-C”, denoting spherical, revolute, cylindrical, and spherical-cylindrical joints, respectively. Each of these joints constrains a different number of degrees of freedom. A spherical joint, or ball joint, constrains the translations of the two links at that point to be the same. A revolute joint constrains all three translational motions and restricts rotation of the links to a single plane. A cylindrical joint constrains two translations and two rotations, such that the two links can rotate with respect to each other along the allowed axis of translation. Finally, the spherical-cylindrical joint constrains only two translational motions, but allows the three rotations of the spherical, allowing the lower swashplate to tilt, move vertically, and rotate.

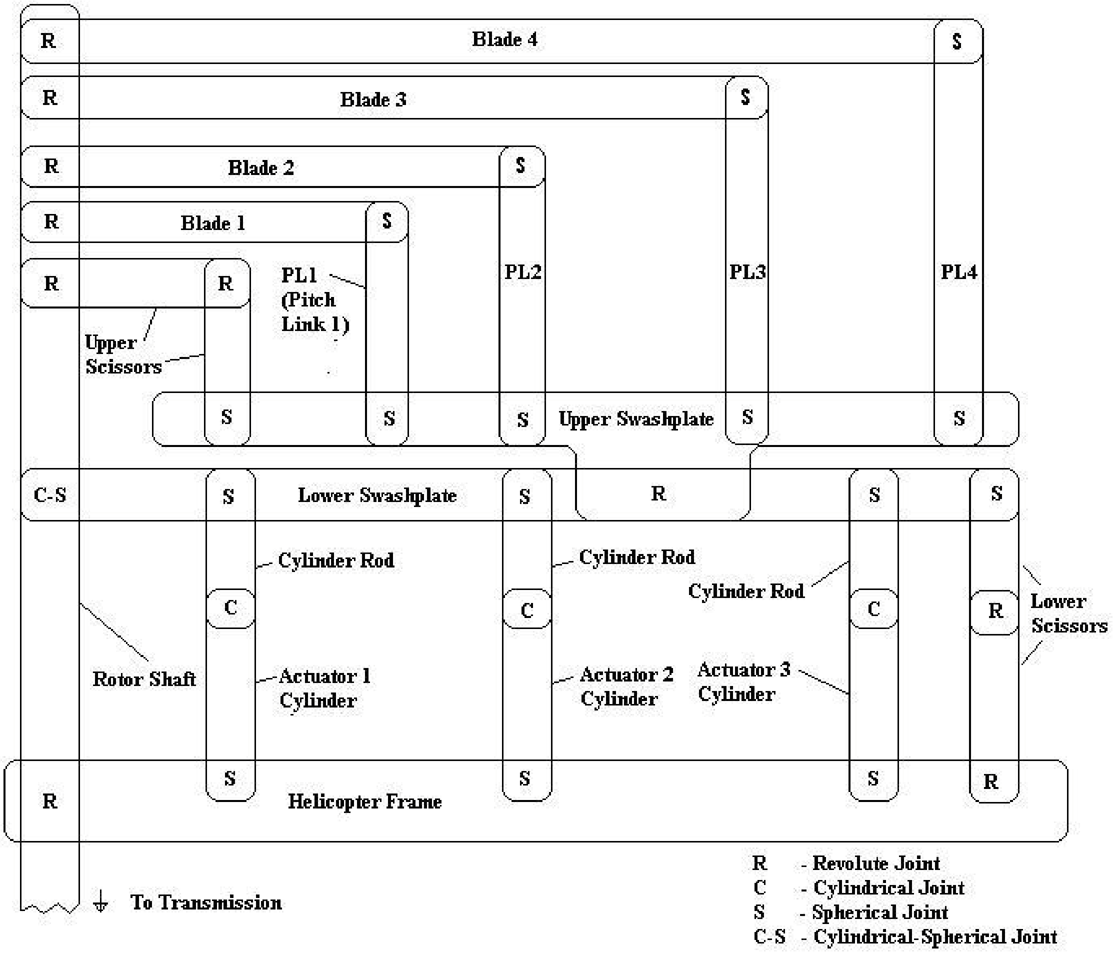

Figure 2.1: Topology of the Swashplate Mechanism.

The mobility of the mechanism, or the total number of translational and rotational degrees of freedom, is easily determined using the Chebychev-Grübler-Kutzbach criterion [15],

$$m = 6(n-1) - 5j_1 - 4j_2 - 3j_3 - 2j_4 - j_5 , \tag{2.1}$$

where m is the mobility of the mechanism, n is the number of links, and each j_k is the number of joints that allow k degrees of freedom. The sixteen spherical joints are j_3's, the ten revolute joints are j_1's, the three cylindrical joints are j_2's, and the spherical-cylindrical joint is a j_4. This gives a mobility of m=14 for the entire linkage. Each cylinder rod, actuator cylinder, and pitch link is able to rotate about its long axis, which accounts for ten degrees of freedom that are not of interest. Moreover, the shaft has a prescribed rotation rate determined by the engine throttle. The remaining three degrees of freedom are the collective pitch of the blades, the lateral cyclic pitch, and the longitudinal cyclic pitch. If these are prescribed, then the actuator displacements can be calculated without calculating forces, assuming all links are rigid. Moreover, if the masses, angular moments of inertia, and applied forces are known, one can calculate the required actuator forces to produce the prescribed blade motions. These are respectively known as the inverse kinematics and the inverse dynamics analysis methods. It is necessary here to model the inverse kinematics and dynamics because the pitch and flap angles of the blades are already known from GENHEL for the duration of each AWC simulation, and the actuator motions and forces that are required to produce the rotor motions must be determined.

2.2 Swashplate Kinematics

The nonlinear kinematics of the swashplate are modeled using inverse kinematics and a vector-rotation approach. The GENHEL output consists, in part, of a time vector and the rotor cyclic and collective pitches for each time step, so the fixed frame values of the pitches are decomposed in order to resolve the time history pitch of each individual blade in the rotating frame.

First, it is necessary to establish a set of basis vectors that define the fixed frame of the helicopter. For this investigation, an orthonormal basis set {$\mathbf{E}_1$, $\mathbf{E}_2$, $\mathbf{E}_3$} defines the fixed frame, where $\mathbf{E}_1$ points to the right of the helicopter, $\mathbf{E}_2$ points to the front of the helicopter, and $\mathbf{E}_3$ points along the mast, or the helicopter's local "up" direction. These are not conventional aeronautical coordinates, but the transformation to the convention of **x** forward, **y** right, and **z** down is simply,

$$\begin{bmatrix} \mathbf{x} \\ \mathbf{y} \\ \mathbf{z} \end{bmatrix} = \begin{bmatrix} 0 & 1 & 0 \\ 1 & 0 & 0 \\ 0 & 0 & -1 \end{bmatrix} \begin{bmatrix} \mathbf{E}_1 \\ \mathbf{E}_2 \\ \mathbf{E}_3 \end{bmatrix}. \tag{2.2}$$

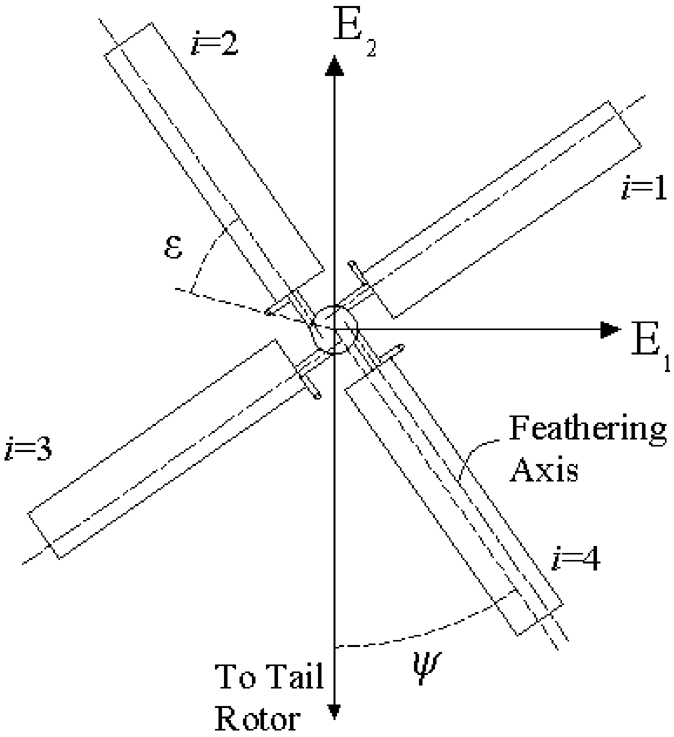

Figure 2.2: Top View of Rotor and Rotor Azimuths.

At simulation time t=0, the blades are oriented with the helicopter fixed-frame axes, $\mathbf{E}_1$ and $\mathbf{E}_2$. The blades are numbered such that,

$$\psi_{bi} = \psi + \frac{2\pi i}{N_b}, \tag{2.3}$$

where ψ_{bi} is the azimuth of blade i, ψ is the rotor speed, Ω, times the time, t, and N_b is the total number of blades on the rotor. The azimuth of a pitch link joint on the upper swashplate is fixed with respect to its blade. The angle between the two is the pitch link lead angle, or ε. Figure 2.2 shows this notation.

The cyclic and collective pitches are combined to form the total pitch of each blade at each time step using,

$$\theta_i = \theta_{1C}\cos(\psi_{bi}) + \theta_{1S}\sin(\psi_{bi}) + \theta_0 = \theta_{cyc} + \theta_{col} + \theta_{twist}, \tag{2.4}$$

where $\theta_{1\mathrm{C}}$ is the lateral cyclic pitch, $\theta_{1\mathrm{S}}$ is the longitudinal cyclic pitch, θ_0 is the collective pitch of the blade at the root, θ_{col} is the collective pitch of the blade at 75% of the radius (R), θ_{cyc} is the pitch of the blade due to cyclic pitch commands, and θ_{twist} is the constant blade twist from the 0.75 R location to the blade root. When referring to the three inputs, $\theta_{1\mathrm{C}}$, $\theta_{1\mathrm{S}}$, and θ_0 are used, and when referring to blade angles, θ_{col} and θ_{cyc} are used. The blade twist is included because the collective input is considered to be zero when $\theta_{col}=0$, not when the blade root has zero pitch. The cyclic and collective pitches for each blade are decoupled in this way so that solutions for the collective and cyclic swashplate motions can be found independently. The rotations of the blade from the non-rotated $\{\mathbf{x}_i',\mathbf{y}_i',\mathbf{z}_i'\}$ frame to the rotated $\{\mathbf{x}_i, \mathbf{y}_i, \mathbf{z}_i\}$ blade coordinate frame, are shown in Figure 2.3, , where $\mathbf{y}_i$ is along the feathering axis. The view in Figure 2.3 is from the center of rotation for the rotor outward along the feathering axis of the blade.

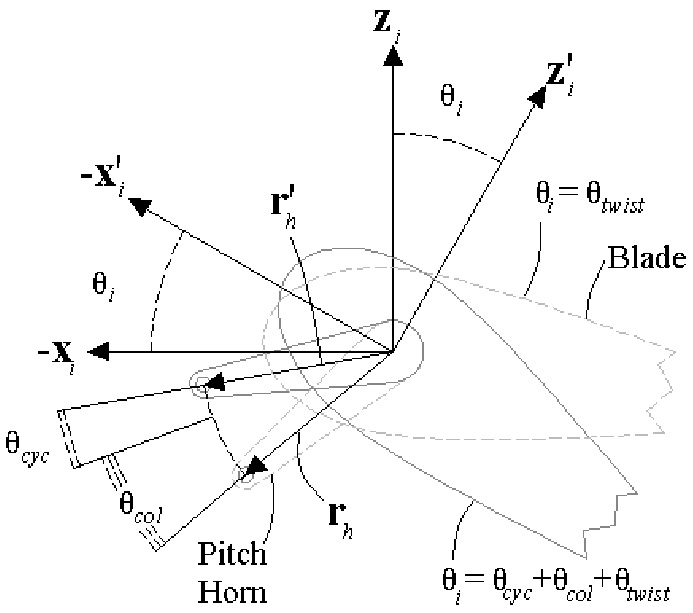

Figure 2.3: Blade Pitch Angles.

These cyclic and collective pitch angles determine the swashplate's vertical position, z_{col}, and its pitch, θ_{sp}, and roll, φ_{sp}, rotation angles. The first, and simplest, variable to calculate is the vertical position. Next, after solving for the vertical displacement of the swashplate, rotations about that point give the swashplate angles.

The collective is named so because the vertical motion of the swashplate imparts the same pitch on all of the blades together. Since the blades act in unison with respect to the swashplate collective motion, it is only necessary to solve for the collective pitch of one blade to solve for all of them. Figure 2.4 demonstrates the vector problem to be solved in order to find z_{col}, the travel of the swashplate resulting in collective pitch. The direction of $\mathbf{c}_{PL}$ and the magnitude of z_{col} are the unknowns, and **O** is the origin, which is the global position of the center of the swashplate when θ_{col} equals zero.

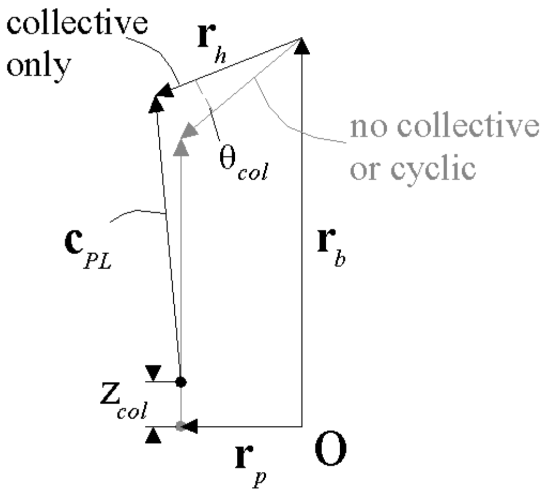

Figure 2.4: Representation of the Collective Pitch Vector Problem.

The vertical displacement of the swashplate, z_{col}, is found by solving the pitch link loop equation,

$$\mathbf{r}_b + \mathbf{r}_h = \mathbf{r}_p + z_{col}\mathbf{E}_3 + \mathbf{c}_{PL}\,. \tag{2.5}$$

This equation is solved by applying the distance constraint that the pitch link is of constant length c_{PL}, so that the solution is,

$$\left\|\mathbf{r}_b + \mathbf{r}_h - \mathbf{r}_p - z_{col}\mathbf{E}_3\right\| = c_{PL}\,, \tag{2.6}$$

$$\mathbf{k} = \mathbf{r}_b + \mathbf{r}_h - \mathbf{r}_p\,, \tag{2.7}$$

$$\left\|\mathbf{k} - z_{col}\mathbf{E}_3\right\| = k_1^{\ 2} + k_2^{\ 2} + \left(k_3 - z_{col}\right)^2 = c_{PL}^{\ \ 2}\,, \tag{2.8}$$

and thus

$$z_{col} = k_3 - \sqrt{c_{PL}^{\ \ 2} - k_1^{\ 2} - k_2^{\ 2}}\,, \tag{2.9}$$

where k_1, k_2, and k_3 are the components of vector **k**, in the $\mathbf{E}_1$, $\mathbf{E}_2$, and $\mathbf{E}_3$ directions.

Following these calculations for the vertical motion of the swashplate, the vertical position of the joint between each pitch link and the upper swashplate is calculated. This is another vector problem with the pitch link enforcing a distance constraint, except that the unknowns are the directions of two vectors, rather than a direction and a distance. The position of vector $\mathbf{r}_p$ is desired in order to determine the vertical position of each pitch link bottom due to the cyclic inputs. Figure 2.5 shows the vectors on the swashplate. Only one blade-pitch link-swashplate loop is shown for clarity.

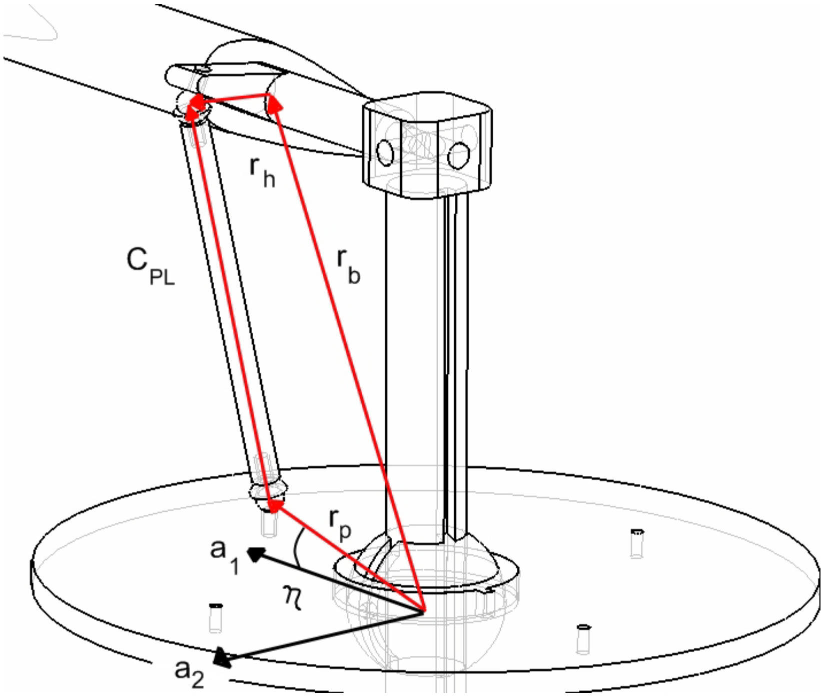

Figure 2.5: The Cyclic Pitch Vector Problem.

Of the vectors shown in Figure 2.5, $\mathbf{r}_b$ and $\mathbf{r}_h$ are known, and $\mathbf{c}_{PL}$ and $\mathbf{r}_p$ are of known lengths, but unknown directions. Basis vectors $\mathbf{a}_1$ and $\mathbf{a}_2$ lie in the $\mathbf{E}_1$-$\mathbf{E}_2$ plane, but $\mathbf{a}_1$ points in the same azimuth as $\mathbf{r}_p$, and $\mathbf{a}_2$ remains perpendicular. The solution of $\mathbf{r}_p$ for each of the pitch links is of primary concern for finding the swashplate tilt angles. First, as was done in the solution for z_{col}, the vector equation is defined,

$$\mathbf{r}_b + \mathbf{r}_h - \mathbf{r}_p = \mathbf{c}_{PL}\,, \tag{2.10}$$

where the vectors $\mathbf{r}_b$ and $\mathbf{r}_p$ are measured from the swashplate origin (not the global origin). In the $\{\mathbf{a}_1,\mathbf{a}_2,\mathbf{a}_3\}$ basis $\mathbf{r}_p$ has the representation,

$$\mathbf{r}_p = \begin{bmatrix} r_p\cos(\eta) \\ 0 \\ r_p\sin(\eta) \end{bmatrix}. \tag{2.11}$$

All vectors are transformed into the $\{\mathbf{a}_1,\mathbf{a}_2,\mathbf{a}_3\}$ basis using,

$$\begin{bmatrix} \mathbf{a}_1 \\ \mathbf{a}_2 \\ \mathbf{a}_3 \end{bmatrix} = \begin{bmatrix} \sin(\psi_p) & -\cos(\psi_p) & 0 \\ \cos(\psi_p) & \sin(\psi_p) & 0 \\ 0 & 0 & 1 \end{bmatrix} \begin{bmatrix} \mathbf{E}_1 \\ \mathbf{E}_2 \\ \mathbf{E}_3 \end{bmatrix}, \tag{2.12}$$

which allows decomposition of the vectors into components in the same basis. If again the vector $\mathbf{k}$ is used to denote the sum of the completely known vectors, then applying the pitch link distance constraint gives,

$$\left(k_1 - r_p\cos(\eta)\right)^2 + k_2^{\,2} + \left(k_3 - r_p\sin(\eta)\right)^2 = c_{PL}^{\,2}, \tag{2.13}$$

which with the following transformations,

$$\cos(\eta) = \frac{1-\tan^2\left(\frac{\eta}{2}\right)}{1+\tan^2\left(\frac{\eta}{2}\right)}, \tag{2.14}$$

and

$$\sin(\eta) = \frac{2\tan\left(\frac{\eta}{2}\right)}{1+\tan^2\left(\frac{\eta}{2}\right)}, \tag{2.15}$$

yields the solution:

$$\eta = 2\tan^{-1}\left(\frac{k_3 - \sqrt{k_3^{\,2} - AB}}{A}\right),$$

$$A=\left(\frac{\left(k_1{}^2+k_2{}^2+k_3{}^2+r_p{}^2-c_{PL}{}^2\right)}{2r_p}+k_1\right),$$

$$B=\left(\frac{\left(k_1{}^2+k_2{}^2+k_3{}^2+r_p{}^2-c_{PL}{}^2\right)}{2r_p}-k_1\right). \qquad (2.16)$$

There are two solutions for the angle η, but the proper one for this geometry is shown in Equation 2.16. Now that the angle η is known, the positions of the lower rod eyes on the pitch links are known from Equation 2.11.

If the first and second pitch link lower rod eye vectors, $\mathbf{r}_{\mathrm{p1}}$ and $\mathbf{r}_{\mathrm{p2}}$, are found using this method, they can be used to find the rotation angles of the swashplate. This is done by finding the vectors relative to these two vectors that represent the plane of the swashplate in local coordinates. In this case, the swashplate is modeled as a thin plate so that any two non-collinear pitch link lower rod eye vectors represent the plane in which the swashplate is oriented, without further manipulation of the vectors.

To represent other vectors as having been rotated with the swashplate, it is necessary to either find the rotation angles or to know the other vectors' locations relative to the $\mathbf{r}_{\mathrm{p}}$'s, which define the rotated plate. The most concise method of expressing swashplate orientation involves using the swashplate rotation angles. The lower swashplate's orientation is represented by a rotation matrix that is formed from two rotations: the first rotation is a roll about the $\mathbf{E}_2$ axis, φ_{sp}, and the second rotation is a pitch about the $\mathbf{e}_1{}'$ axis, θ_{sp}, as shown in Figure 2.6. In matrix form, this transformation between the global and local swashplate bases is,

$$\begin{bmatrix}\mathbf{e}_1\\ \mathbf{e}_2\\ \mathbf{e}_3\end{bmatrix}=\begin{bmatrix}\cos(\varphi_{sp}) & 0 & -\sin(\varphi_{sp})\\ \sin(\theta_{sp})\sin(\varphi_{sp}) & \cos(\theta_{sp}) & \sin(\theta_{sp})\cos(\varphi_{sp})\\ \cos(\theta_{sp})\sin(\varphi_{sp}) & -\sin(\theta_{sp}) & \cos(\theta_{sp})\cos(\varphi_{sp})\end{bmatrix}\begin{bmatrix}\mathbf{E}_1\\ \mathbf{E}_2\\ \mathbf{E}_3\end{bmatrix}=\mathbf{R}_{sp}\begin{bmatrix}\mathbf{E}_1\\ \mathbf{E}_2\\ \mathbf{E}_3\end{bmatrix}. \qquad (2.17)$$

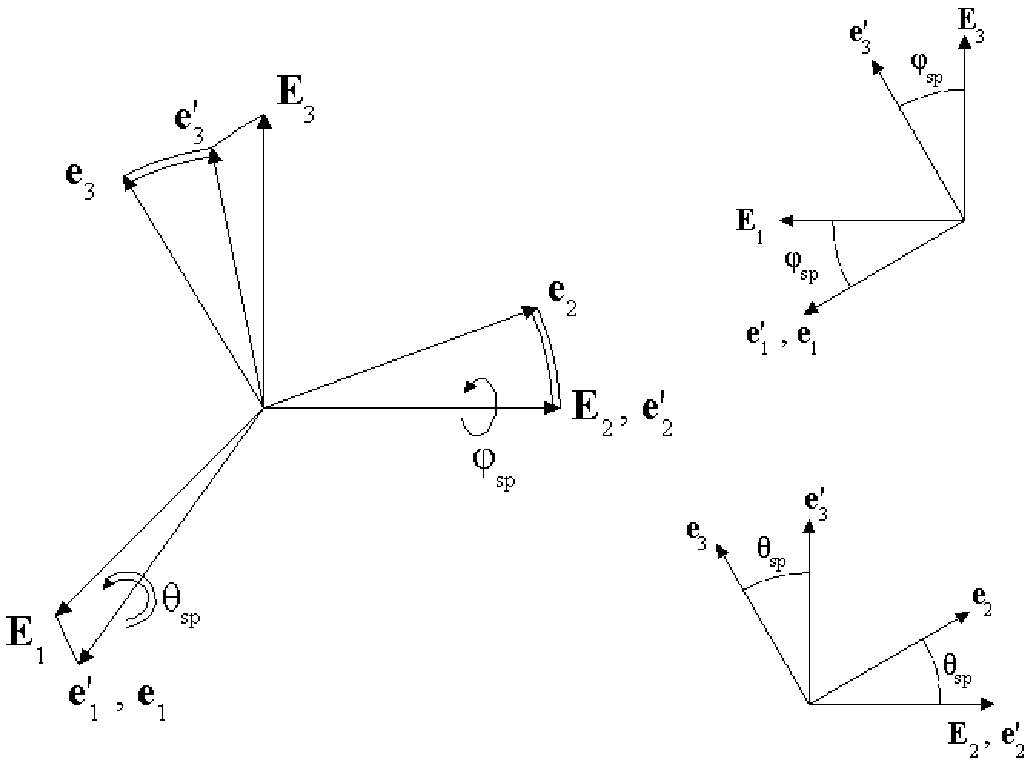

Figure 2.6: The Swashplate Rotation Angles.

Assuming the swashplate is thin, the vectors to the pitch link lower rod eyes on the swashplate can be distilled into a single normal vector representing the orientation of the swashplate by taking their cross product. Of this normal vector, **n**, the unit vector $\hat{\mathbf{n}}$ is simply the basis vector $\mathbf{e}_3$. This means that the known normal vector can be used to solve the equation,

$$\mathbf{R}_{sp}{}^{-1}\mathbf{E}_3 = \hat{\mathbf{n}}\,, \tag{2.18}$$

giving,

$$\theta_{sp} = \sin^{-1}(-\hat{n}_2)\,, \tag{2.19}$$

and

$$\varphi_{sp} = \sin^{-1}\left(\frac{\hat{n}_1}{\cos(\theta_{sp})}\right). \tag{2.20}$$

Finally, once the swashplate angles are calculated, each swashplate actuator's extension is solved by rotating each vector that points from the swashplate center to the actuator rod end by the rotation matrix $\mathbf{R}_{sp}^{-1}$ to find the representation in global coordinates, $\mathbf{r}_A$, and then solving the vector equation,

$$z_{col}\mathbf{E}_3 + \mathbf{r}_A - \mathbf{r}_{base} = \mathbf{c}_A \, , \tag{2.21}$$

where $\mathbf{r}_{base}$ is the vector from the global origin to the actuator base and $\mathbf{c}_A$ is the vector representing the extended or retracted actuator, from base to rod end. The solution to this equation is simple, since the left side is known. Actuator extensions are then obtained by finding the change in the magnitude of $\mathbf{c}_A$ from the neutral position magnitude. Please see Appendix B for some checks performed to verify the computer model of the swashplate kinematics.

2.3 Swashplate Dynamics

Once the inverse kinematics relating blade motions to actuator motions have been solved, the task becomes one of finding the forces the actuators must generate in order to produce the prescribed rotor motions. Once again, as in the kinematics, the process of finding the actuator requirements begins in the blades. Each blade experiences aerodynamic and inertial forces which affect the flight of the helicopter. For the analysis here, the torsional moments are of concern. Flap and pitching motions of the blade are known from GENHEL, and can both be included in the blade torsion equation. However, flap motion for a blade that has the center of gravity balanced at the feathering axis and no kinematic pitch-flap coupling has no effect on the torsional loads. The blade rigid flap-pitch equation of motion for torsion becomes the same as the equation of motion for rigid torsion without considering blade flap. Moreover, since the purpose of this model is to compare the effect of two controllers on the actuators in a DI operation that is similar to a hover, it is assumed that the aerodynamic moment remains constant. In hover, this assumption is reasonable because the moment coefficient about the quarter-chord axis for a given airfoil section remains relatively constant over a wide range of blade angles of attack [23], and the air velocity over each radial blade segment is nearly constant.

Figure 2.7 shows the torsion-axis moments on the blade that are considered, including the aerodynamic moment, the propeller moment, and the moment due to inertia.

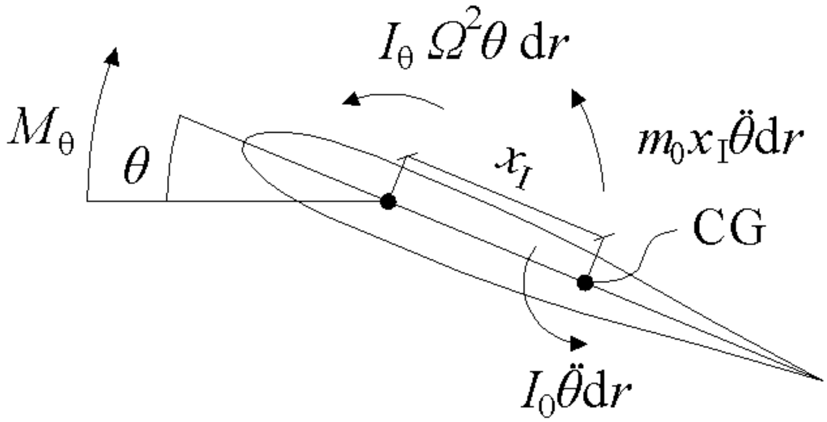

Figure 2.7: Blade Segment Torsional Loads.

Integration along the blade length gives the inertial and aerodynamic moments which are then balanced with the torque due to the pitch link force to give the moment balance at the blade root,

$$-\int M_\theta dr + \int I_\theta \Omega^2 \theta dr + \int I_0 \ddot{\theta} dr + \int m_0 {x_I}^2 \ddot{\theta} dr + k_r \theta - \left(\mathbf{r}_h \times \mathbf{F}_{PL}\right)\cdot \hat{\boldsymbol{\theta}} = 0\,, \qquad (2.22)$$

where $\hat{\boldsymbol{\theta}}$ is the direction of rotation, $\mathbf{F}_{PL}$ is the pitch link force vector, I_0 is the mass moment of inertia in pitch about the center of mass, I_θ is the section mass moment of inertia about the feathering axis, Ω is the angular velocity of the rotor, m_0 is the mass per unit length, k_r is the spring constant for the blade root in pitch, r is the radius, and M_θ is the section aerodynamic pitching moment. Using the parallel axis theorem,

$$I_\theta = I_0 + m_0 {x_I}^2\,, \qquad (2.23)$$

and resolving the integrals gives the moment balance,

$$-M_a + \sum_{section} I_{f,\mathrm{section}}\left(\ddot{\theta} + \Omega^2 \theta_{\mathrm{section}}\right) + k_r \theta - \left(\mathbf{r}_h \times \mathbf{F}_{PL}\right) \cdot \hat{\boldsymbol{\theta}} = 0 , \qquad (2.24)$$

with,

$$I_f = \int I_0 dr , \qquad (2.25)$$

and

$$M_a = \int M_\theta dr . \qquad (2.26)$$

The built-in twist of the blade varies from the root to the tip, so the integral over the radius is simplified to a summation of the spanwise blade sections to allow for changing blade pitch angles. The root cutout spans the first 15% of the radius. Therefore, for the calculations here, the blade is segmented into 17 spanwise sections of length 5% R, though it could be divided into more or fewer segments for greater accuracy or greater speed of calculation, respectively. The section pitch angle is determined by adding the root pitch angle and the average section twist angle.

The unknown in Equation 2.24 is the magnitude of the pitch link force, which is needed to find the forces on the swashplate. The direction of the pitch link force vector coincides with the direction of the pitch link, and is obtained by solving Equation 2.10. However, the angular acceleration of the blade, $\ddot{\theta}$, must be determined before calculating the pitch link force. The blade angles calculated in the kinematics section are derived from cyclic and collective angle outputs from the GENHEL models. Unfortunately, there are no blade acceleration outputs from this particular simulation, so the accelerations are estimated by differentiating a cubic interpolant of the angular positions. With this approach, a least-squares curve fitting method fits a cubic polynomial to the blade pitch data series which is centered on point θ_n, where n denotes the time step. The second derivative of this least-squares estimate at point θ_n is then estimated numerically. The index n is next incremented and the process is repeated until the end of the data series is reached, and the accelerations at all time steps are estimated. This process loses the first and last three data points because the curve fitting is based on a centered seven-point cubic interpolant, not a right or left-sided one. These data points are not a significant loss from the approximately ten-thousand points in the data series.

Solving for the pitch link force is now a matter of rearranging Equation 2.24 to be,

$$F_{PL} = \frac{-M_a + \sum_{section} I_{f,section}\left(\ddot{\theta} + \Omega^2 \theta_{section}\right) + k_r \theta}{\left(\mathbf{r}_h \times \hat{\mathbf{F}}_{PL}\right) \cdot \hat{\theta}}, \tag{2.27}$$

where F_{PL} is the magnitude of the pitch link force vector. The pitch link force vectors are solved for each blade.

The next challenge is to solve for the actuator forces by solving the force and moment balances on the swashplate. The swashplate is regarded as two thin disks, one rotating with the rotor at angular speed Ω about $\mathbf{E}_3$, and the other with zero rotation about the $\mathbf{E}_3$ direction (the shaft direction). As thin disks, the top and bottom swashplates are assigned moment of inertia matrices of,

$$\mathbf{I}_{sp} = \begin{bmatrix} \frac{m_{sp} r_{sp}^{\ \ 2}}{4} & 0 & 0 \\ 0 & \frac{m_{sp} r_{sp}^{\ \ 2}}{4} & 0 \\ 0 & 0 & \frac{m_{sp} r_{sp}^{\ \ 2}}{2} \end{bmatrix}, \tag{2.28}$$

where m_{sp} is the mass of the top or bottom swashplate and r_{sp} is the radius of the disk. The masses of the top and bottom swashplates are assumed to be the same in this model.

The swashplate bearing, represented as a cylindrical-spherical bearing in the mobility analysis, and the swashplate scissors allow three degrees of freedom for the swashplate—two rotations and one vertical translation. Because reaction forces at the bearing for the lateral and longitudinal directions are not of interest, the component of the force balance equation in the direction of interest, $\mathbf{E}_3$, is found by taking the dot product of the forces with $\mathbf{E}_3$. Similarly, the reaction torque due to the upper and lower swashplate scissors is not of interest. The lateral and longitudinal moments on the swashplate are examined by taking the moment balance equation's projection onto $\mathbf{E}_1$ and $\mathbf{E}_2$. The force equation before projection onto the $\mathbf{E}_3$ direction is,

$$2m_{sp}\ddot{z}_{col}\mathbf{E}_3 - \sum_{i=1}^{N_b}\left(\mathbf{F}_{PL,i}\right) + \sum_{n=1}^{3}\left(\mathbf{F}_{A,n}\right) = 0\,, \qquad (2.29)$$

and the moment balance equation from which pitch and roll moments are extracted is,

$$\sum_{i=1}^{N_b}\left(\mathbf{r}_{p,i}\times\mathbf{F}_{PL,i}\right) + \sum_{n=1}^{3}\left(\mathbf{r}_{A,n}\times\mathbf{F}_{A,n}\right) + \mathbf{I}_{sp}\boldsymbol{\alpha}_{top} + \mathbf{I}_{sp}\boldsymbol{\alpha}_{bot}$$

$$+\boldsymbol{\omega}_{top}\times\mathbf{I}_{sp}\boldsymbol{\omega}_{top} + \boldsymbol{\omega}_{bot}\times\mathbf{I}_{sp}\boldsymbol{\omega}_{bot} = 0\,. \qquad (2.30)$$

In these equations $\mathbf{F}_{A,n}$ is the n^{th} actuator's force, $\mathbf{r}_{A,n}$ is the global representation of the vector from the swashplate center to the joint with actuator *n*, $\boldsymbol{\omega}$ denotes an angular velocity, $\boldsymbol{\alpha}$ denotes an angular acceleration, and subscripts *top* and *bot* refer to the top (upper) and bottom (lower) swashplates.

The angular velocities of the top and bottom swashplates, $\boldsymbol{\omega}_{top}$ and $\boldsymbol{\omega}_{bot}$, are determined by a constraint-based approach. From the position solution, the swashplate angles are already known, so that the rates, $\dot{\varphi}_{sp}$ and $\dot{\theta}_{sp}$, are readily calculated using the same approach as was used to find the blade pitch angle rates. Given that these rates are determined, and the rate of rotation about the rotor shaft is a constant speed of Ω, the top and bottom swashplate angular velocities must satisfy the constraints,

$$\begin{bmatrix} \mathbf{E}_3{}^T \\ \mathbf{E}_2{}^T \\ \mathbf{e}_1{}^T \end{bmatrix} \boldsymbol{\omega}_{top} = \begin{bmatrix} \Omega \\ \dot{\varphi}_{sp} \\ \dot{\theta}_{sp} \end{bmatrix}, \qquad (2.31)$$

and,

$$\begin{bmatrix} \mathbf{E}_3{}^T \\ \mathbf{E}_2{}^T \\ \mathbf{e}_1{}^T \end{bmatrix} \boldsymbol{\omega}_{bot} = \begin{bmatrix} 0 \\ \dot{\varphi}_{sp} \\ \dot{\theta}_{sp} \end{bmatrix}. \qquad (2.32)$$

These equations are solved by multiplying both sides by the inverse of the coefficient matrix on the left to obtain the angular velocity vectors. Similarly, the angular acceleration vectors, $\boldsymbol{\alpha}_{top}$ and $\boldsymbol{\alpha}_{bot}$, are simply the time derivatives of the angular velocity vectors, which gives,

$$\boldsymbol{\alpha}_{top} = \boldsymbol{\alpha}_{bot} = \begin{bmatrix} \mathbf{E}_3{}^T \\ \mathbf{E}_2{}^T \\ \mathbf{e}_1{}^T \end{bmatrix}^{-1} \begin{bmatrix} 0 \\ \ddot{\varphi}_{sp} \\ \ddot{\theta}_{sp} \end{bmatrix}. \qquad (2.33)$$

With the angular velocity and accelerations solved, the unknown actuator forces in the force balance equation and the two moment balance equations are solved by decomposing the actuator force vectors into magnitudes and directions. The direction of each actuator's force is known because it is equivalent to the direction of the actuator, $\mathbf{c}_A$, which was solved in the kinematics section. The unknown magnitudes comprise three unknowns in the three equations, which allows for an exact solution using,

$$\begin{bmatrix} \mathbf{E}_1 \cdot \left(\mathbf{r}_{A,1} \times \hat{\mathbf{F}}_{A,1}\right) & \mathbf{E}_1 \cdot \left(\mathbf{r}_{A,2} \times \hat{\mathbf{F}}_{A,2}\right) & \mathbf{E}_1 \cdot \left(\mathbf{r}_{A,3} \times \hat{\mathbf{F}}_{A,3}\right) \\ \mathbf{E}_2 \cdot \left(\mathbf{r}_{A,1} \times \hat{\mathbf{F}}_{A,1}\right) & \mathbf{E}_2 \cdot \left(\mathbf{r}_{A,2} \times \hat{\mathbf{F}}_{A,2}\right) & \mathbf{E}_2 \cdot \left(\mathbf{r}_{A,3} \times \hat{\mathbf{F}}_{A,3}\right) \\ \mathbf{E}_3 \cdot \hat{\mathbf{F}}_{A,1} & \mathbf{E}_3 \cdot \hat{\mathbf{F}}_{A,2} & \mathbf{E}_3 \cdot \hat{\mathbf{F}}_{A,3} \end{bmatrix} \begin{bmatrix} F_{A,1} \\ F_{A,2} \\ F_{A,3} \end{bmatrix} +$$

$$\begin{bmatrix} \mathbf{E}_1 \cdot \left(\sum_{i=1}^{N_b} \left(\mathbf{r}_{p,i} \times \mathbf{F}_{PL,i}\right) + \mathbf{I}_{sp}\left(\boldsymbol{\alpha}_{top} + \boldsymbol{\alpha}_{bot}\right) + \boldsymbol{\omega}_{top} \times \mathbf{I}_{sp}\boldsymbol{\omega}_{top} + \boldsymbol{\omega}_{bot} \times \mathbf{I}_{sp}\boldsymbol{\omega}_{bot} \right) \\ \mathbf{E}_2 \cdot \left(\sum_{i=1}^{N_b} \left(\mathbf{r}_{p,i} \times \mathbf{F}_{PL,i}\right) + \mathbf{I}_{sp}\left(\boldsymbol{\alpha}_{top} + \boldsymbol{\alpha}_{bot}\right) + \boldsymbol{\omega}_{top} \times \mathbf{I}_{sp}\boldsymbol{\omega}_{top} + \boldsymbol{\omega}_{bot} \times \mathbf{I}_{sp}\boldsymbol{\omega}_{bot} \right) \\ \mathbf{E}_3 \cdot \left(2m_{sp}\ddot{z}_{col}\mathbf{E}_3 + \sum_{n=1}^{3} \mathbf{F}_{A,n} \right) \end{bmatrix} = \mathbf{0} \, . \qquad (2.34)$$

Thus, the actuator motions for a given rotor motion are calculated by multiplication of Equation 2.34 by the inverse of the force coefficient matrix, thereby solving the inverse dynamics of the swashplate.

Chapter 3

Actuation Comparison and Results

3.1 Simulation Data

Results from the two gust compensation controllers showed similar performance (see Figure 1.8) and lead one to delve into the effects each controller has on the helicopter in aspects other than pitch, roll, and yaw rates. The model of the swashplate mechanism, detailed in Chapter 2, is used to determine the swashplate actuator motions and forces during DI operations. This is next used to compare the swashplate-based and TEF-based airwake compensators with regards to their effect on the swashplate actuators in terms of required motion and forces, fatigue, and potential for wear.

The GENHEL simulations, which include the ship airwake and the AWCs, output the lateral and longitudinal cyclic pitches and the collective pitches for the helicopter rotor over the entire simulation. The cyclic pitches for the swashplate-based and TEF-based gust compensation, as well as a case where the MFC and pilot model controller are operating, but the AWC is disabled, are shown in Figure 3.1. The “No AWC” case in the figure has the most exaggerated motions overall because the pilot model attempts to keep station, but there is no additional gust rejection. There is a time delay incorporated into the OCM of the pilot, which may have the result that once the controller begins to correct for a gust, the effect on the roll and pitch of the helicopter is already pronounced and larger cyclic pitches are required to return the helicopter to the desired position and orientation than if there was no time delay. The “Swashplate” AWC and the “TEF” AWC cases in the figure have less pronounced longitudinal pitching than the “No AWC” case, but the magnitude of the varying pitches in the swashplate case is, in general, greater than that of those in the TEF case. This is understandable since the swashplate AWC is using the swashplate to compensate for gusts on top of the MFC pitches, whereas the TEF AWC does not adjust cyclic and collective pitches for compensation, but adjusts flap deflection to impart differential lift on the rotor.

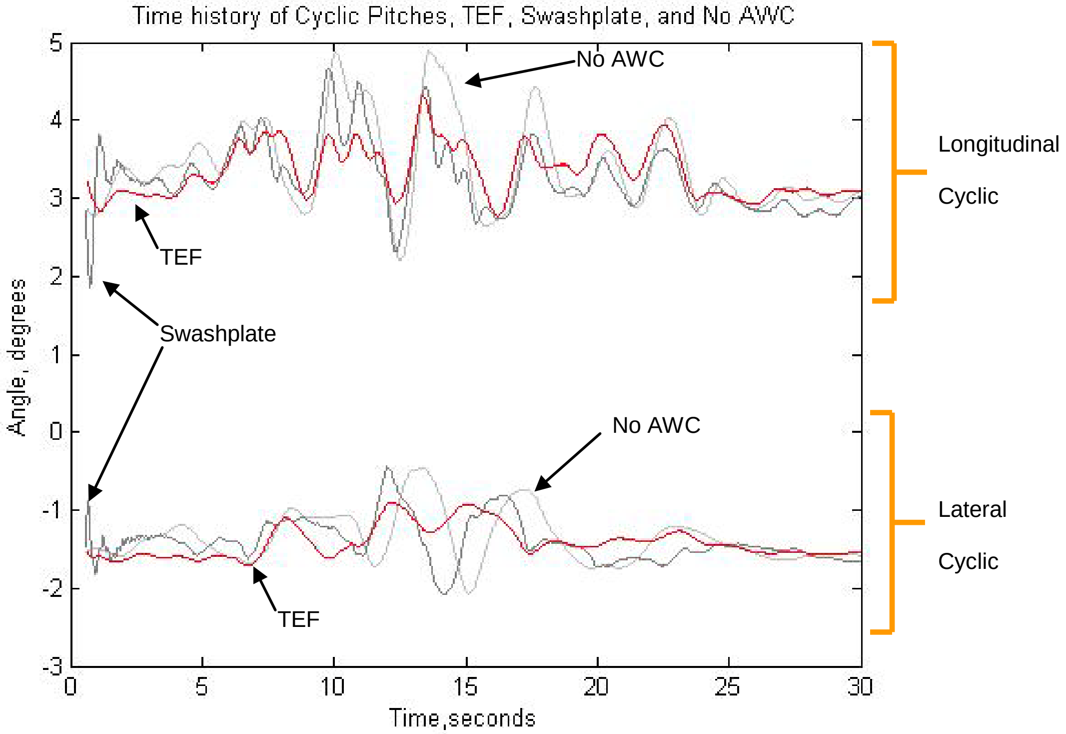

Figure 3.1: GENHEL Simulation Cyclic Pitch Time Histories.

A comparison of the total range of cyclic pitch is shown in Figure 3.2. Interestingly, the total range of cyclic pitches is greatest for the swashplate AWC case, even though locally the peaks of the “No AWC” are of greater magnitude over most of the simulation. The TEF AWC case requires less rotor cyclic range by almost half.

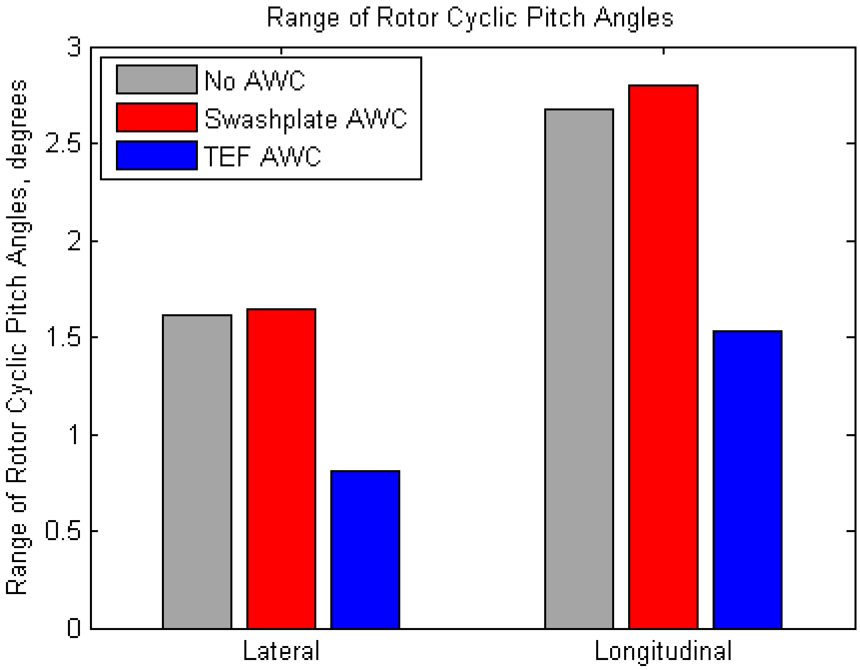

Figure 3.2: The Range of Rotor Cyclic Pitches.

3.2 Swashplate Model Results

Using the GENHEL results, force and displacement histories for the swashplate actuators are generated with the swashplate model. The model parameters, representative of the UH-60 swashplate, are listed in Table C.1. Figure 3.3 is a representation of the azimuthal position of the actuators used for the UH-60. The base of actuator 1 is in the $\mathbf{E}_1$ direction, the base of actuator 2 is in the $\mathbf{E}_2$ direction, and the base of actuator 3 is in the $-\mathbf{E}_1$ direction, and all are at the same radius and oriented vertically when in their neutral positions. The resulting actuator extensions and forces for all the cases are displayed in Figures 3.4 and 3.5.

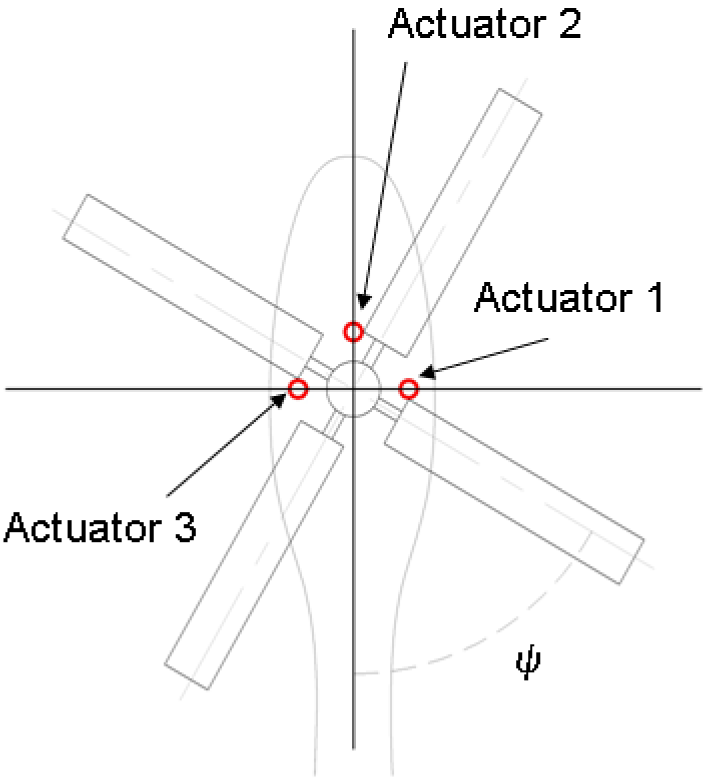

Figure 3.3: Actuator Azimuthal Positions—View of Rotor from Above.

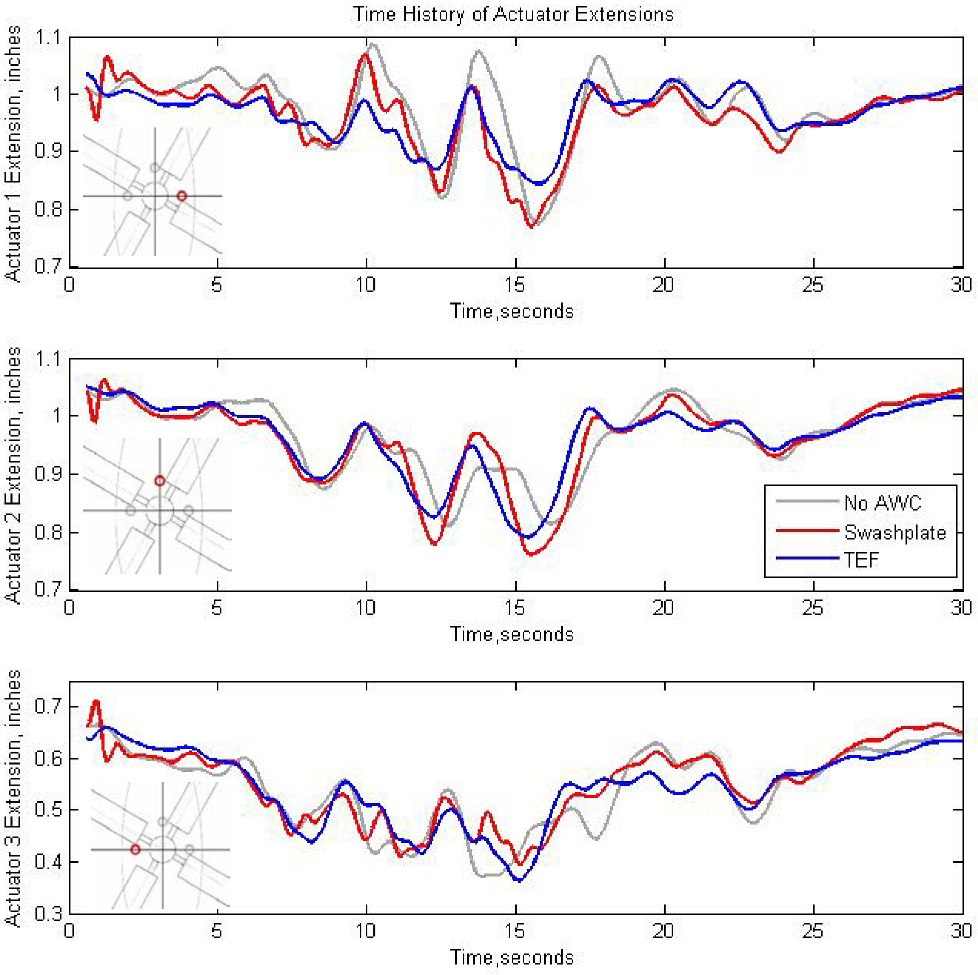

Figure 3.4: Swashplate Actuator Extensions.

In Figure 3.4 the swashplate and TEF motions follow a similar pattern while the motions of the actuators in the case with no AWC show a somewhat different pattern. This is to be expected because the same type of behavior is seen in the longitudinal and lateral cyclic pitches, but notice how the differences in actuator extensions are generally less than 0.1 inches.

Qualitatively, the swashplate case is producing more high frequency motion in the actuators than the TEF case.

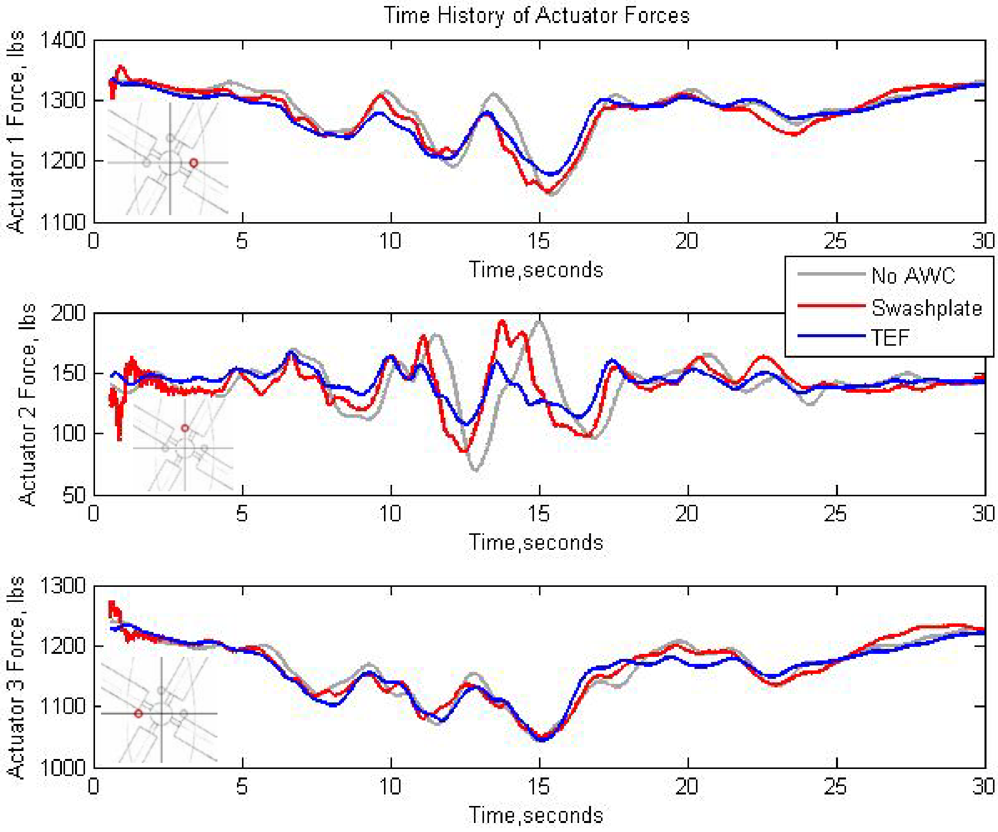

Figure 3.5: Swashplate Actuator Forces.

Similarly, in Figure 3.5, the actuator forces for each case follow the same general path, though there are differences. This similarity is because the helicopter is made to hover over the same position at the same altitude in all simulations, which results in collective blade pitches that are very similar for the cases over the entire simulation. The force curves oscillate about the force due to collective pitch, which varies as the pilot model controller adjusts the collective in an attempt to hold position. Also note that in actuators 1 and 3, the force curve is always between 1000 and 1400 pounds. These two actuators bear the majority of the vertical loading when there is a cyclic input and all of the vertical loading when there is no cyclic input for this actuator-swashplate geometry. A 120-degree separation of the actuators distributes vertical loads more evenly among all three actuators. Of particular interest are the oscillations in forces in the swashplate case compared to the TEF case. These are especially apparent in the actuator 2 plot, but they are present in all plots with magnitudes of the same order as those in the plot for actuator 2.

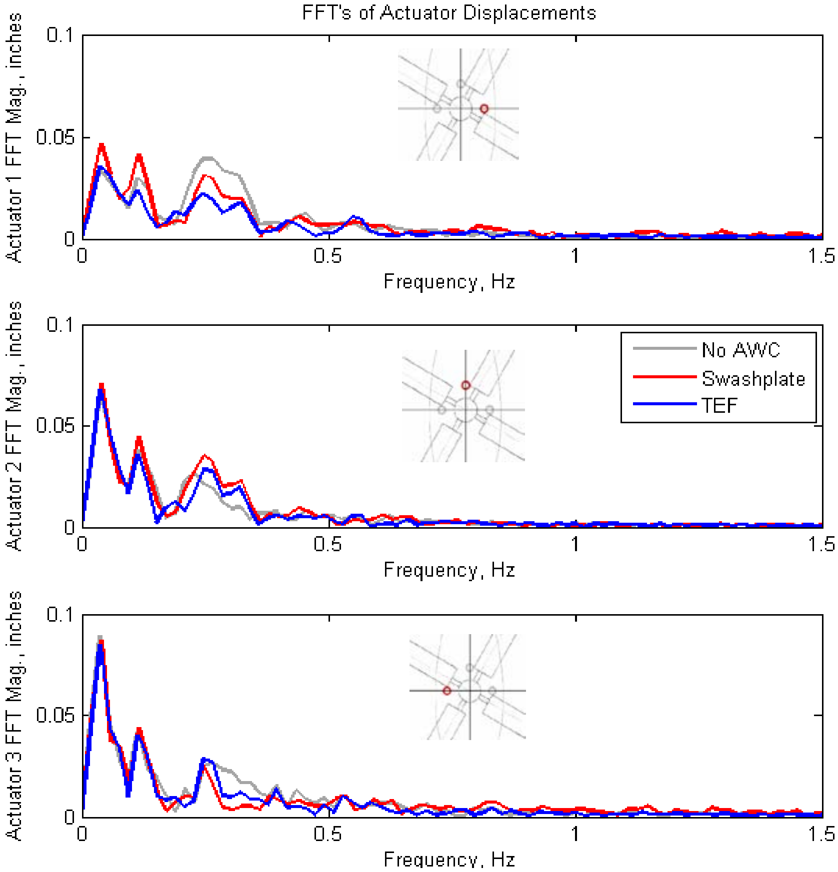

Figure 3.6: FFT’s of Actuator Displacements.

The frequency components of the actuator extensions and forces are readily examined by taking a Fast Fourier Transform (FFT) of the time series. The primary frequencies are all less than 0.5 Hz for the swashplate motions, as shown in Figure 3.6—hardly a difficult task for the actuators, which have a cut-off frequency of about 10 Hz. One would expect the larger components to be low frequency because the large actuator motions in Figure 3.2 occurred over a larger time period. Because the gross motions were very close, the FFT's are similar as well.

Fourier transforms of the actuator forces are displayed in Figure 3.7. Actuators 1 and 3 show a frequency distribution similar to that of the actuator displacements. Interestingly, the FFT for actuator 2 shows more activity in the swashplate case above 0.5 Hz than the TEF and baseline "No AWC" cases. This is expected because the swashplate is not actuating for gust rejection in the TEF and "No AWC" cases. Moreover, the forces due to collective motion are not as large in this actuator as in actuators 1 and 2, and so do not obscure the small oscillatory forces. It is also interesting to note that actuator 2 has a significantly lower magnitude for the peak frequency component in the TEF case than in the swashplate case and the "No AWC" case.

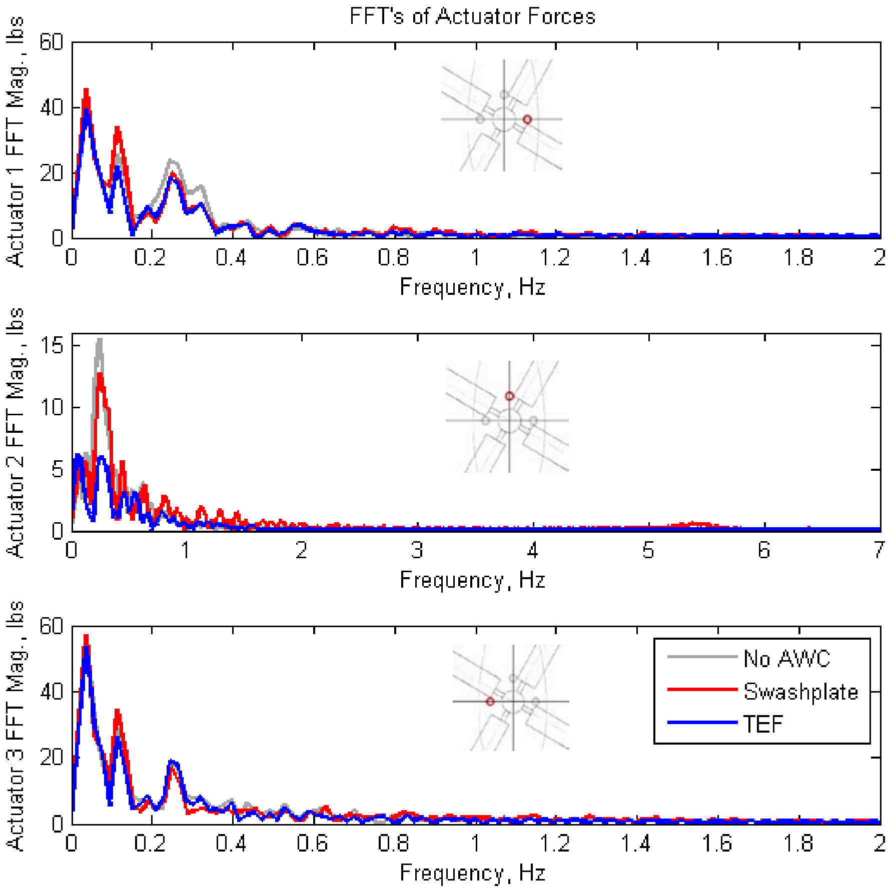

Figure 3.7: FFT's of Actuator Forces.

The actuators are capable of 20,000 lbs stall load and a no-load velocity of 6 in/sec. These forces certainly are not, nor were ever expected to be, outside the actuator limits, and calculation of the rates reveals that the maximum rate is about 0.5 in/sec, as shown Figure 3.8.

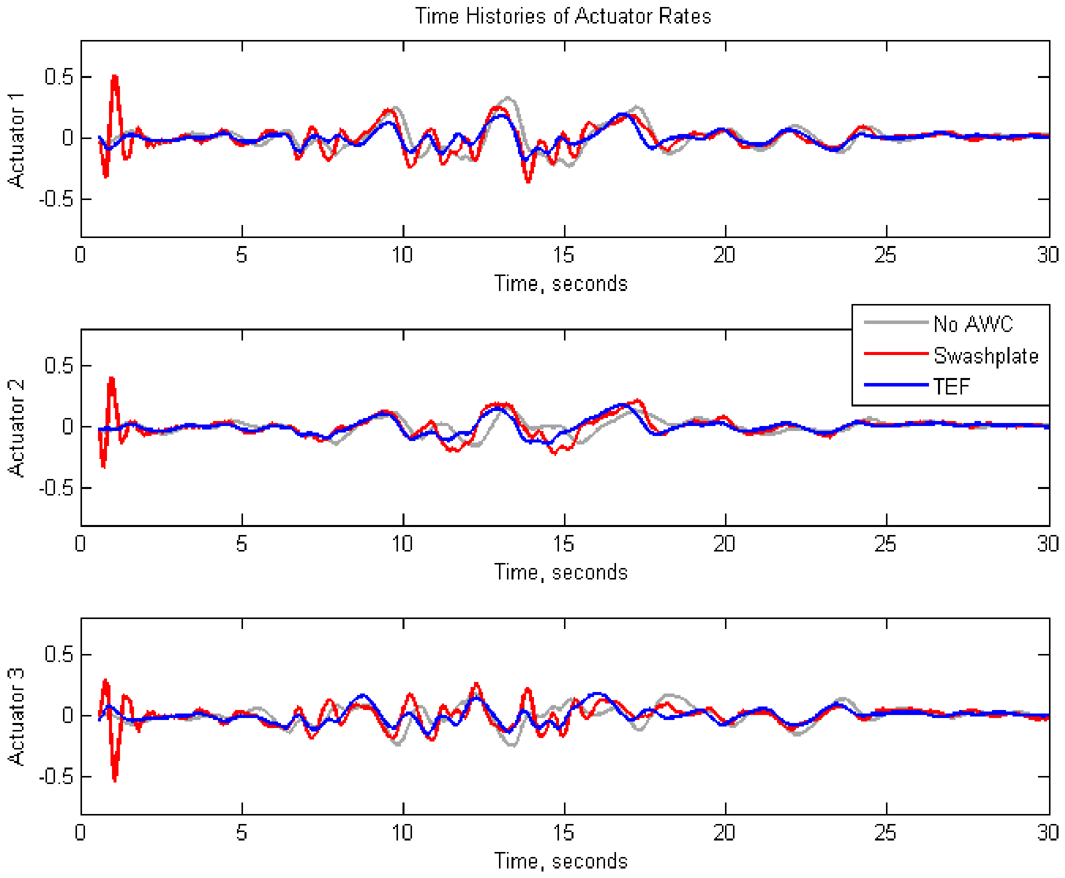

Figure 3.8: Actuator Rates.

The forces are small for swashplate-based gust alleviation when compared to the tough performance criteria the actuators must meet for extreme maneuvers. There are clearly no control system performance capabilities that either gust alleviation scheme is required to exceed. Even so, it is useful to examine the power required for actuation to see if there is total power savings with TEFs and to determine whether the total power consumed is significant. The root mean-square (RMS) power, illustrated in Table 3.1, is an indicator of the power each method requires of the swashplate actuators. For a complete comparison, the TEF power obtained with this model should be added to the flap actuation power obtained from a TEF dynamics model.

	RMS Power, HP			% of “No AWC” case		
	No AWC	SP	TEF	No AWC	SP	TEF
Act1	0.019	0.019	0.012	100	100.9	61.5
Act2	0.001	0.002	0.001	100	141.6	102.4
Act3	0.013	0.015	0.010	100	110.3	76.3

Table 3.1: RMS Power of the Actuators.

As can be seen from Table 3.1, the power required for actuation in this case is quite small. Nevertheless, for a trailing edge flap system to use an equal or lesser amount of power for actuation when compared to the swashplate-based AWC, it must consume no more than about 0.013 RMS HP for gust alleviation.

The two gust rejection methods have different influences on rotor actuation requirements, but it is clear that all motions and forces are well within system capabilities. The power consumed is very small when compared to the total control system capability, which in turn is much less than the power required to rotate the blades to keep the helicopter aloft. Both AWC methods are quite feasible in terms of swashplate actuation requirements.

3.3 Reliability

Both AWC methods show similar displacement, rate, force, and power requirements. The discrepancy in power required is small enough that aerodynamic drag differences in the two methods are likely to dwarf it. None of the metrics thus far have clearly pointed to the best method of gust alleviation, so the methods are next compared in terms of reliability.

3.3.1 Fatigue

Even though both systems are feasible in terms of actuation demands, reliability is a major concern for any aircraft system, especially when flight critical components, such as the swashplate actuators, the control system, and the rotor, are involved. Helicopters, in particular, suffer from component fatigue due to the high vibratory loads created in forward flight. Naturally, then, it is of interest to investigate the impact the changing actuation loads have on component life. Typically, cumulative fatigue damage is approximated using the Palmgren-Miner cycle-ratio summation rule [66],

$$\sum_k \frac{n_k}{N_k} = D \,, \tag{3.1}$$

where the total number of cycles (n_k) at each stress level (σ_k) is divided by the total number of cycles that that level can withstand to failure (N_k). Counting the number of these cycles over a period of time can give an estimation of the life of a component. The component fails when D=1. Unfortunately, the specific geometries of the UH-60 components are not known, so stresses can not be calculated.

As a measure of potential fatigue damage, the number of actuator forcings—an approximation of force half-cycles—is counted instead of the stress cycles. This are proportional to the stresses in the component of interest, whether it is a bearing, a thread, a rod-eye, or some other part. One forcing is the change in force over the period where the sign of the derivative of the force remains constant. This means that if the force is increasing, decreases for a period, and then increases again, the magnitude of the decrease is recorded and added to a histogram bin. The forcings are thus grouped by magnitude to give a better idea of how the forces on the actuators and interconnected components behave over the simulation.

The histograms of the forcings, by actuator, are displayed in Figure 3.9. It is immediately evident that the there are considerably more forcings in the swashplate AWC case than in the other two cases combined. However, these are mostly less than 30 lbs., whereas the pitch links on a UH-60 must withstand oscillatory loads of 3000 lbs. [24]. Clearly, the components should be sized to manage these small loads. Only for non-endurance limit materials should this be a problem that would warrant further investigation, and even then only if a swashplate-based AWC is being used a significant portion of flight time.

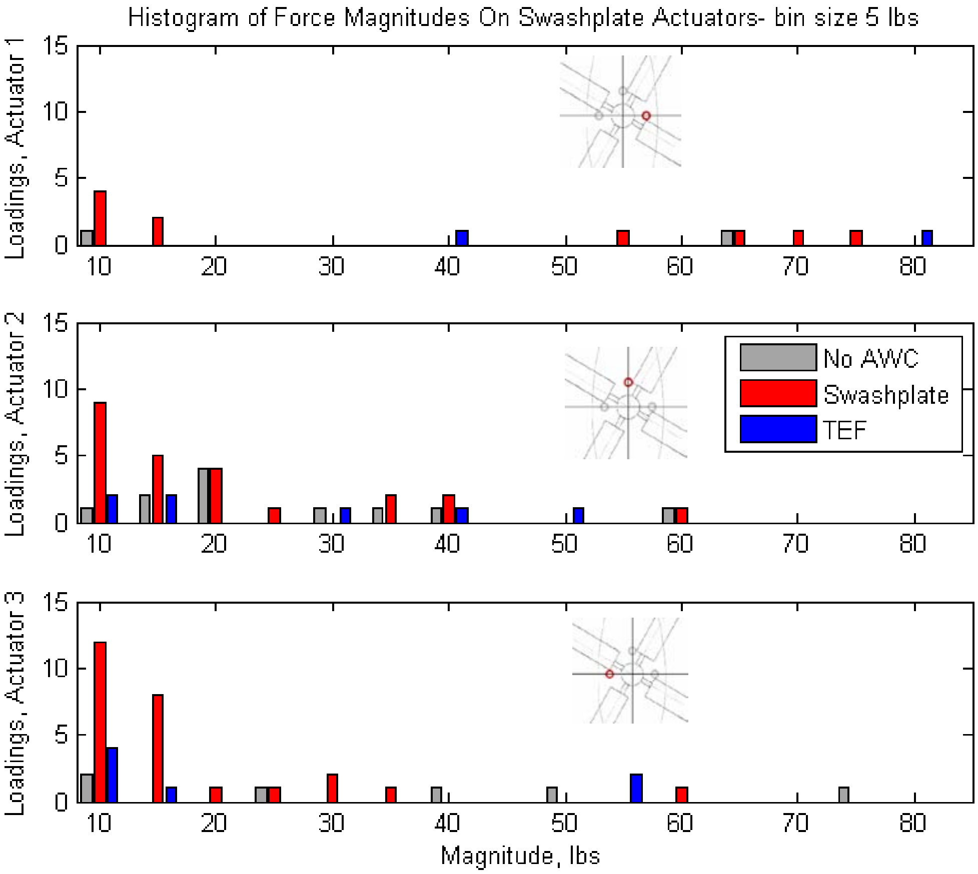

Figure 3.9: Histogram of Actuator Forcing.

3.3.2 Wear

The other major reliability concern for actuator components is wear. At the simplest level, two-body sliding wear can be described by Archard's Wear Equation [25],

$$V_w = \frac{k_w F_N L}{H}, \tag{3.2}$$

where V_w is the volume of material worn away from a surface, k_w is the wear coefficient, F_N is the normal force, L is the sliding distance, and H is the hardness of the wear surface. The wear coefficient depends on the two materials and the lubrication of the sliding contact. Spherical joints and hydraulic cylinder seals see lubricated sliding wear, so it is worth investigating which method of airwake compensation is more likely to result in the most wear. Unfortunately, neither the normal forces on the wear surfaces nor the wear surfaces' hardnesses are known. However, the cumulative actuator travel corresponds to the sliding distance on the actuator seals. This will be used as a comparison metric.

The cumulative actuator travel is the total distance traveled by an actuator over the entire simulation. This means that if an actuator extends one inch and then retracts half an inch over the simulation, the cumulative travel is one and a half inches. The cumulative travel for all actuators and cases is displayed in Figure 2.10. The values of total travel are given in Table 3.2.

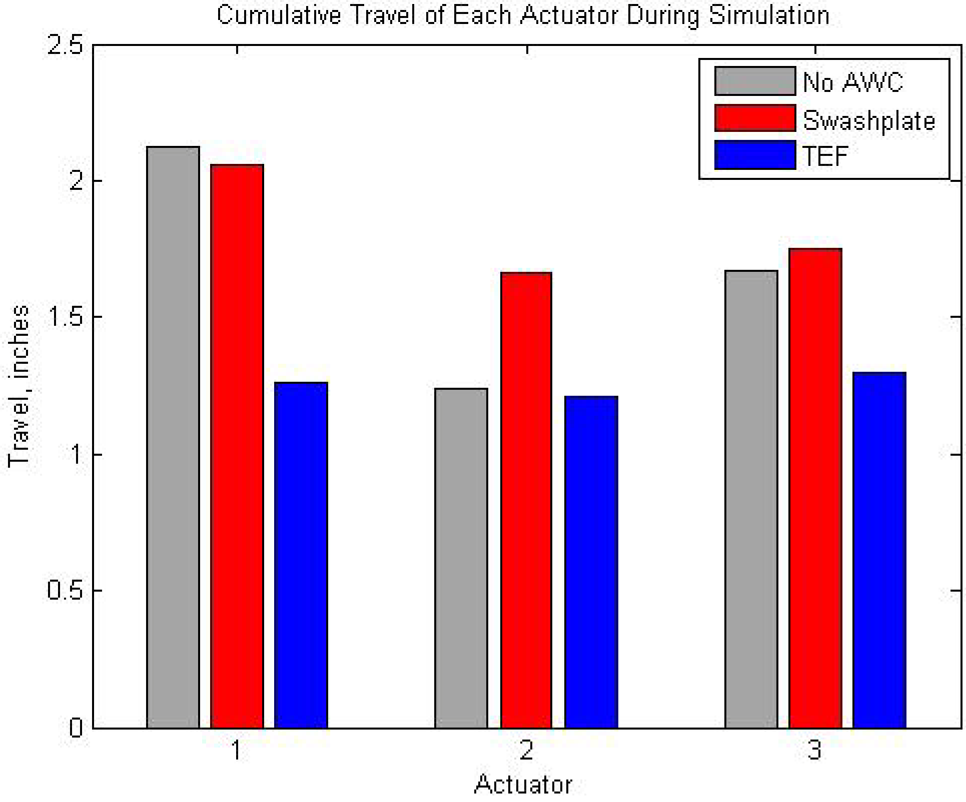

Figure 3.10: Cumulative Actuator Travel.

	Cumulative Actuator Travel, inches			% of "no AWC" case		
	no AWC	SP	TEF	no AWC	SP	TEF
Act1	2.12	2.05	1.26	100	96.7	59.2
Act2	1.24	1.66	1.21	100	134.1	97.5
Act3	1.67	1.75	1.30	100	104.8	77.9

Table 3.2: Cumulative Actuator Travel.

The actuator travels, and therefore the amounts of wear due to airwake compensation, are considerably different. While the "no AWC" case has travel similar to the swashplate case except in actuator 2, the TEF case has greatly diminished travel compared to the other two. The greater travel was expected of the swashplate AWC case. The case without gust rejection has large travel due to larger actuator strokes, while the swashplate case's travel can be attributed to a larger number of small strokes, as seen in Figure 3.4. The TEF case clearly shows less travel in the swashplate servos, of which reliability is of the utmost importance. Comparing combined travel of all of the actuators shows that, overall, travel in the TEF case is reduced by 31% from the travel in the swashplate case. If shipboard gust alleviation is used frequently, or if this can be representative of atmospheric gust alleviation which would conceivably be used for more flight hours, the reduced travel in the TEF case could increase the life of these flight critical components. Of course, the reliability of the added components for a TEF system would have to be tested and taken into consideration to completely understand the reliability advantages and disadvantages.

While simple wear is certainly a concern in the design of any component, perhaps a greater concern is 3-body wear, in which a particulate becomes trapped between the two sliding surfaces and tumbles and gouges the components. Hydraulic cylinder seals and bearings are lubricated by a thin hydrodynamic film, in which two surfaces are separated by a fluid layer, which greatly reduces wear. The thicker this film, the more clearance is available to pass large particles though without causing damage to either surface. Every time a hydraulic cylinder—one of the actuators—reverses direction of motion, the minimum fluid film thickness decreases, increasing the chances that a particle may be large enough to cause damage to the seal, or to the cylinder rod or bore, or to both [25, 26]. Additionally, this fluid film may not fully form if the distance between direction reversals, a “stroke”, is not greater than twice the film thickness [26]. This incomplete fluid film formation results in a boundary lubrication condition which effectively increases the value of k_w in Archard’s Wear Equation, and thus increases the potential for wear. Figure 3.11 diagrams the possibilities of minimum film thickness reduction and boundary lubrication.

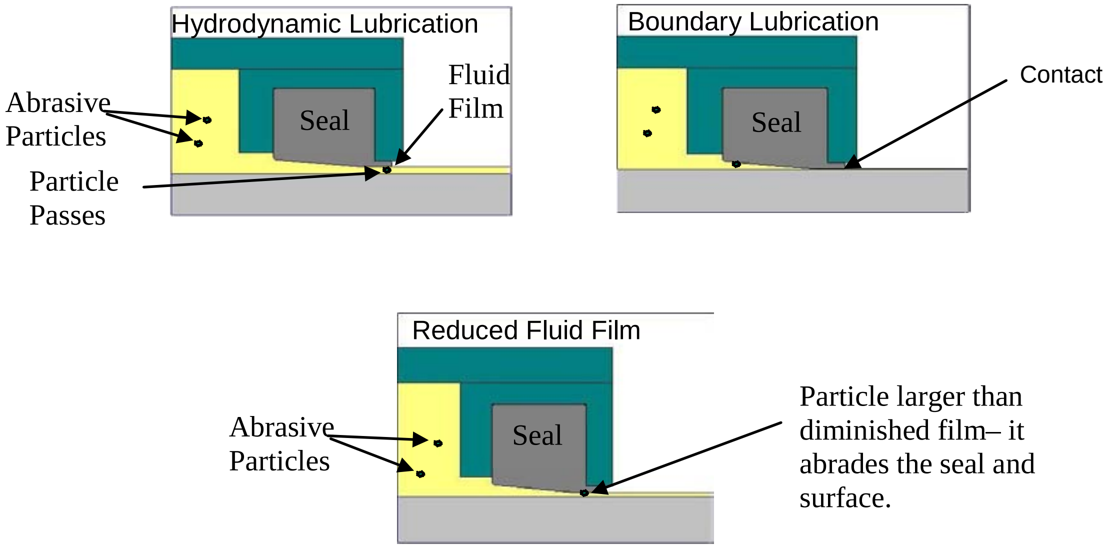

Figure 3.11: Hydrodynamic Fluid Film Concerns.

A count of actuation direction reversals is constructed to compare the potential for increased particulate wear. Figure 3.12 displays the results. Every stroke the actuator takes, no matter how long or short, is defined as the travel between direction reversals for the purposes here, rather than as the maximum displacement of the actuator. Thus, a count of the strokes is a count of the number of reversals plus one, since there is no reversal of direction at the end of the series. As seen in Figure 3.12, the swashplate case has up to about 60% more reversals, depending on the actuator, than the TEF case. The TEF and “no AWC” cases are similar except for actuator 1.

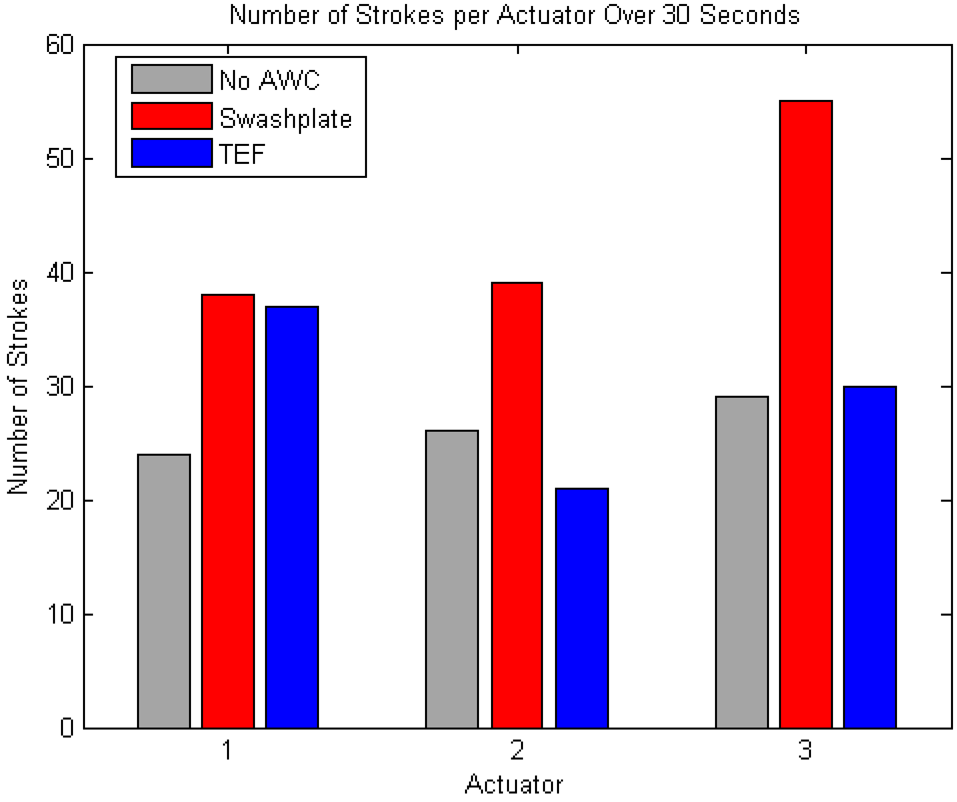

Figure 3.12: Total Actuator Strokes.

In addition to the number of strokes, the length of each stroke must not be too small or there is a risk of partial fluid film collapse. A histogram of the stroke lengths, displayed in Figure 3.13, is compiled to determine which gust rejection scheme creates the most potential for this condition to arise. Once again, the swashplate case dominates this wear condition, with the most small strokes. For actuator 1, the number strokes of length from 0 to 0.5 inches is about the same in the TEF and swashplate cases. Overall, the number of small strokes in the “no AWC” case and the TEF case is about the same, though the distributions are different. This is expected of these flight conditions since small swashplate actuator adjustments are made for gust compensation in the swashplate condition, but not in the other two.

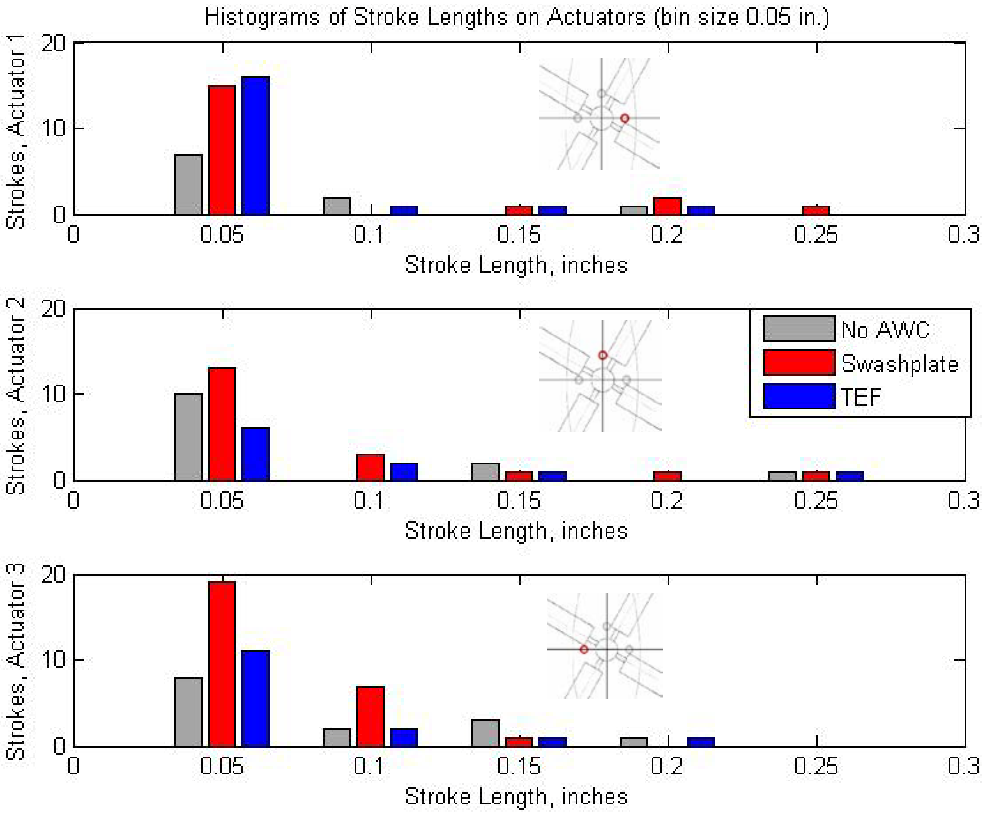

Figure 3.13: Histogram of Stroke Lengths.

Wear can be rather difficult to predict, but these indicators suggest that the swashplate-based gust alleviation method will have a negative impact on the life of flight critical components. Moreover, TEF-based gust alleviation may decrease wear due to dynamic interface tasks. Flight tests must be conducted for verification. Additionally, the wear from gust alleviation in DI tasks alone may not be significant, depending on the percent of flight time spent using the AWC. If compensators are developed for atmospheric gust rejection, similar reliability concerns to the ones expressed here should be investigated for those gust rejection methods as well.

Chapter 4

Vibration Reduction Comparison

4.1 Helicopter Vibration

Active rotors have potential for use in a variety of secondary control functions in addition to gust alleviation, including vibration reduction, rotor power reduction, blade-vortex interaction (BVI) noise reduction, reduction of blade bending moments, in-flight blade tracking, reconfiguration of controls for damage compensation, and artificial lag damping [27]. These possibilities and the possibility of eventually creating a swashplateless rotor encourage ongoing research in IBC.

Helicopters are prone to vibrations by their nature as rotary wing aircraft. The dominant frequency of helicopter vibrations in the helicopter airframe during forward flight is N_b per revolution, or N_bP, and is also known as the blade passage frequency. These vibrations are caused by periodic airloads created in the changing aerodynamic environment each blade experiences with respect to azimuth [29]. Other vibrations come from the engine, the tail rotor, and the transmission [28]. These vibrations contribute to undesired pilot and component fatigue.

To mitigate vibrations, rotors and fuselages are typically designed with vibration response in mind. Vibration absorbers are placed on the rotor or on the airframe. Springs or elastomers have been used to isolate the source of vibrations from the airframe [29]. Passive vibration isolators using variants of the Dynamic Antiresonant Vibration Isolation (DAVI) system such as the Bell Nodal Beam System, the Bell LIVE® system, Lord Fluidlastic® devices, and the MBB ARIS system, have also seen some success [29, 68]. Yet another method of reducing vibrations is to place active elements on the airframe which cancel some helicopter vibrations by creating vibrations 180 degrees out of phase with the major frequency component of airframe vibrations [30]. All of these systems attempt to compensate for vibrations after they have been generated. These are displayed in Figure 4.1.

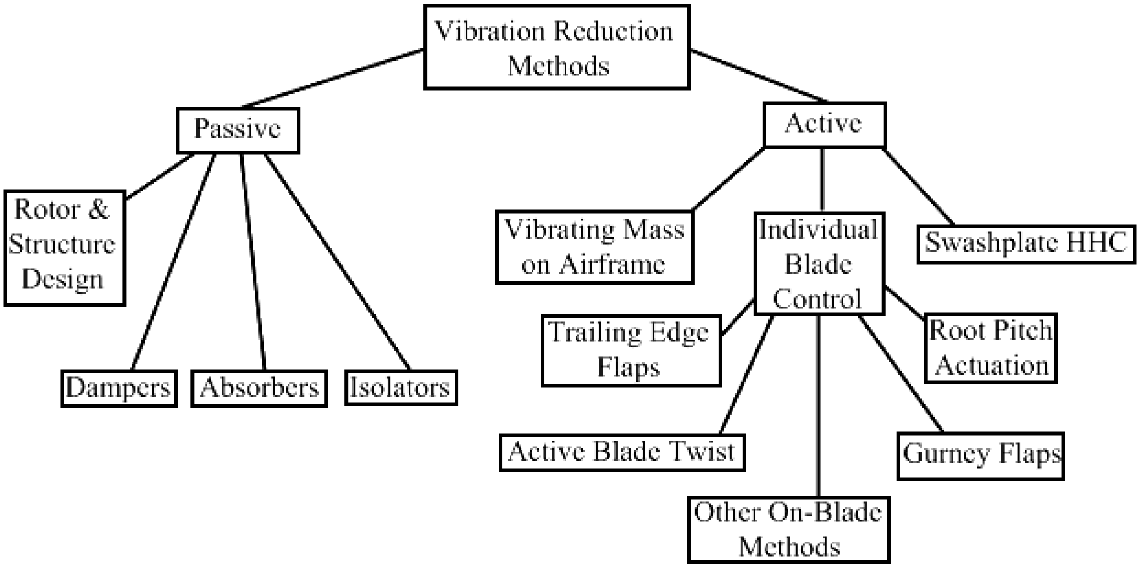

Figure 4.1: Various Helicopter Vibration Reduction Methods.

Yet another method of reducing vibrations is known as swashplate Higher Harmonic Control, or HHC. This actuates the swashplate by N_bP, to send (N_b-1)P, N_bP, and (N_b +1)P commands to the blades in addition to the primary flight control commands,

$$\theta_{HHC,i} = \sum_{k=N_b-1}^{N_b+1}\left[A_k \cos\left(k\psi_{b,i} + \phi_{HHC}\right) + \theta_k \cos(k\psi + \phi_{HHC,col})\right], \quad (4.1)$$

where $\theta_{HHC,i}$ is the higher harmonic control portion of the angle of the i^{th} blade, k is the summation variable (the harmonic), A_k is the amplitude of the k^{th} harmonic cyclic input, , θ_k is the amplitude of the k^{th} harmonic collective input, ϕ_{HHC} is the cyclic control phase angle, and $\phi_{HHC,col}$ is the collective control phase angle. HHC constrains the vibration control inputs for the blades by this equation. Closed-loop HHC can adjust the amplitudes of the cyclic and collective inputs, and the value of the phase angles, but is still constrained to the form of Equation 4.1 and to the three harmonics of the rotor speed previously mentioned.

These higher harmonic commands influence blade motion by introducing higher frequency cyclic pitches, which in turn reduces vibratory loads. Flight tests were conducted on a modified OH-6A [31] and an S-76 [32, 33]. The OH-6A test showed about an 84% reduction in total vibration levels at the pilot seat with the swashplate HHC on and the bifilar pendulum absorbers removed. The S-76 showed vibration reductions of about 90% at the pilot seat with the swashplate HHC using 4P inputs. The bifilar pendulum absorbers were also removed in this test. Pitch link loads with the HHC engaged were within the design limits of the pitch links. Interestingly, the S-76 actuators were bench tested and showed no additional seal wear over the test of fifty-million HHC cycles. It was not mentioned whether particulates were introduced to mimic hydraulic fluid conditions in the field.

Swashplate HHC may have practicality issues because of wear concerns similar to those expressed earlier for swashplate-based gust alleviation. Moreover, in the S-76 tests the HHC actuators introduced a buzz in the pilot stick through the control linkages that was uncomfortable. Swashplate HHC use is limited because it does not allow for control of harmonics aside from (N_b-1)P, N_bP, and (N_b +1)P. For example, 2P harmonics have shown potential for reducing rotor power consumption and BVI noise—on a 4-bladed rotor with swashplate HHC, these would not be possible. Additionally, swashplate HHC relies on a swashplate primary control system and so does nothing to reduce the parasitic drag introduced by the control linkages.

4.2 Active Rotors for Vibration Control

Individual blade control has the promise of overcoming some of the problems inherent to swashplate HHC. IBC actuation allows for blade pitch inputs of any harmonic, as opposed to the three harmonics to which swashplate HHC is restrained. IBC may be operated with a HHC algorithm—that is, the signals are decomposed into harmonics—or, if it is desired, it may be operated so that blade motions are completely independent, so that,

$$\theta_{IBC,i} = \theta\left(t\right), \tag{4.2}$$

where $\theta_{IBC,i}$ is the pitch of the i^{th} blade due to individual blade control and $\theta(t)$ is the commanded blade pitch. The blade pitch can be commanded as desired without harmonic constraints as long as the commands are within the capabilities of the actuators.

There are various proposed methods of implementing IBC, including root pitch control, trailing edge flaps, active twist, Gurney flaps, leading edge slat, leading edge droop, and oscillatory jets. Here, root pitch actuation and TEFs are reviewed because of the advances toward implementation of these on production helicopters. The two are compared for vibration reduction capabilities, required actuation moment, and required power by reviewing current literature on these subjects. Other design concerns such as weight, volume, and centrifugal loading are also addressed.

4.2.1 Root Pitch Control

Of all of the active rotor IBC methods, root pitch control is the most similar to swashplate control because it indexes the pitch of the entire blade, just as the swashplate does, except without the harmonic kinematic constraints the swashplate imposes. This makes root pitch control the logical first step for designing an IBC rotor. Additionally, the blade geometry remains unchanged, which is aerodynamically advantageous. Pitching the entire blade in this method requires high actuation forces [39].

Guinn [34] proposed an IBC system called Individual Blade control Independent of the Swashplate, or IBIS, which removes the swashplate and places actuators in the rotating frame inside the hub of a Bell 412 helicopter (the 412 has a maximum take off weight of 11,900 lbs and a 4-bladed rotor with a diameter of 46 ft [69]). The actuators are linear hydraulic actuators operating on hub-internal pitch horns for each blade. This system places all hydraulics in the rotating frame, which increases the size and complexity of the hub, but eliminates the complexity and maintenance concern of a hydraulic slip ring. While the moment required to pitch the blades is not mentioned, the actuators are specified to each apply 1270 lbs. There are four actuators per blade for redundancy, and any two can provide the required control power for primary flight control and for secondary control functions such as vibration reduction. The configuration is shown in Figure 4.2, where the view is inward toward the hub along the feathering axis of a blade.

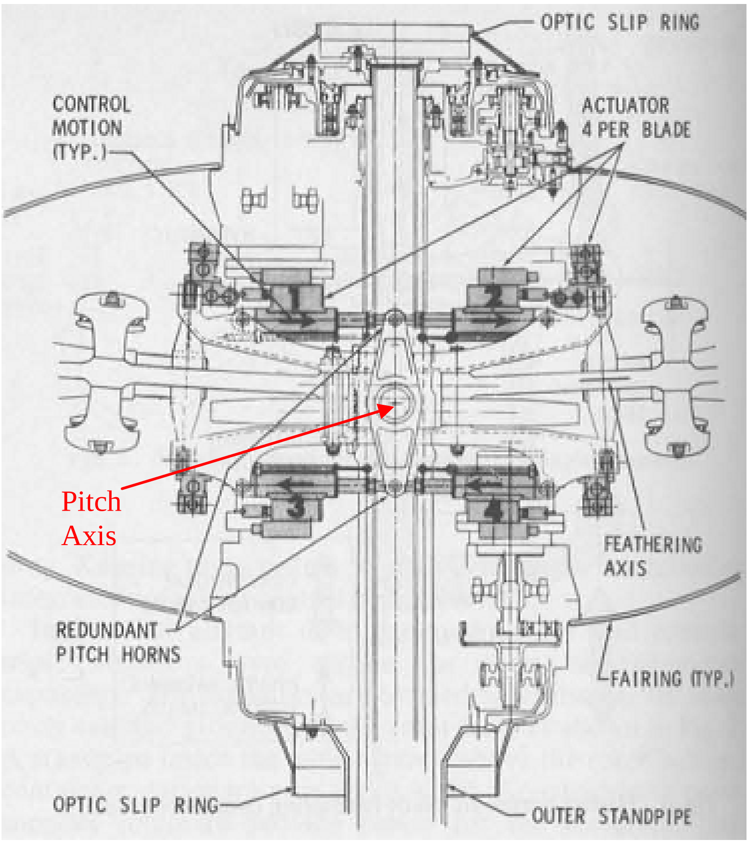

Figure 4.2: The IBIS Concept [34].

ZF Luftfahrttechnik, or ZFL, a German company, has gone a step further than concept and built and tested root pitch actuators for light, medium, and heavy helicopters. The light helicopter full-scale wind tunnel tests were conducted on the four-bladed BO-105 rotor in [35] and [36]. The BO105 root pitch actuators were also flight tested, but the actuation authority was limited for safety reasons [42, 43]. The full-scale wind tunnel tests of a medium-weight helicopter were conducted on the four-bladed UH-60 rotor [37, 38, 24] and the heavy helicopter flight tests were performed on a six-bladed CH-53G using open-loop [39] and closed-loop [40] control. The actuators are hydraulic pitch links which replace the standard pitch links. These actuators are fed by a hydraulic pump through a slip ring. These do not have the advantage of replacing the swashplate for primary flight control, but they are capable of secondary control functions such as

BVI noise reduction and vibration reduction. Because the hydraulic pitch links are in series with the primary control system, they must be failsafe. To address this design criterion, ZFL designed a locking piston that engages when hydraulic pressure is lost, thus creating a rigid link that behaves as a normal pitch link. The hydraulic pitch link used on the UH-60 is shown in Figure 4.3. The horizontal section contains the locking piston and a high pressure gas used to engage the locking piston in case of hydraulic pressure loss.

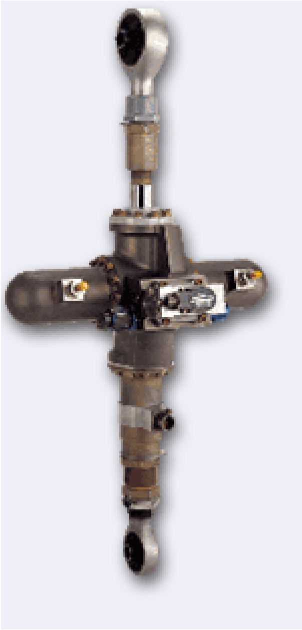

Figure 4.3: UH-60 Hydraulic Pitch Link [41].

More recently, ZFL has begun development of an electrical root pitch actuation system for the purposes of primary and secondary control [27]. This system uses a synchronous motor to adjust the pitch of a blade through a gearbox. All actuation takes place in the rotating frame, and only electrical power and control signals must be transmitted to the rotating frame through a slip ring. This system is still in testing, but shows promise as a way of implementing root pitch IBC without the complications of hydraulics, and without the need of a swashplate for primary control.

The wind tunnel tested and flight tested root pitch actuation schemes showed similar open-loop vibration reductions. In these tests, the HHC control equation was used for commanding the blades, though the possible control frequencies are not restricted to those of swashplate HHC. The maximum vibration reductions, the actuation phase angle, the actuation frequency in terms of rotor rotation rate, the forward speed of the helicopter, and the blade deflection in degrees are listed in Table 4.1.

Test	**Blade Deflection**	**Frequency**	**Phase Lead**	**Vibration Reduction**	**Speed**
BO-105 Open-Loop Wind Tunnel Test [35, 36]	1 degree	3P	150 degrees	55%	43 kts
UH-60 Open-Loop Wind Tunnel Test [37, 38]	1 degree	3P	315 degrees	70%	46 kts
CH-53 Open-Loop Flight Test [39]	0.15 degrees	5P	120 degrees	63%	60 kts

Table 4.1: Hydraulic Pitch Link Open-Loop Vibration Reductions.

The vibration reductions were significant, but it is difficult to compare the results with varying helicopters, actuation frequencies, and advance ratios. The first two cases have advance ratios here around 0.1, while in the CH-53 case the ratio is about 0.14. These are not so different that comparison is impossible, but there is no standard platform or flight condition for these tests. For the open-loop tests it is interesting to note that the deflection used for vibration reduction in the CH-53 test is about an order of magnitude lower than in the other two tests. The lower magnitude could be explained if the baseline 6P vibration levels on the CH-53 are also lower than the baseline 4P levels on the BO-105 and the UH-60. Additionally, the CH-53 actuators are capable of 1.1 degrees amplitude, but larger amplitudes can aggravate vibration levels in some cases [39]. Also of interest is that for open-loop, single-harmonic input vibration reduction, the N_b-1 harmonic delivers the best results in reducing hub vibrations.

Different criteria were used to determine the vibration reductions in each of the three cases. For the BO-105, the vibration reduction reported here is estimated from graphs of the 4P hub shear and lift forces by finding the magnitude of the vibration for controlled and uncontrolled cases, where,

$$\text{Vibration Magnitude} = \sqrt{\text{Lift}_{4P}{}^2 + \text{Shear}_{4P}{}^2}\,. \tag{4.3}$$

In Reference [37], the vibration level for the UH-60 is determined to be,

$$\text{Vibration Level} = \text{Lift}_{4P} + \text{Shear}_{4P} + \text{Moment}_{4P} + \text{Torque}_{4P}\,. \tag{4.4}$$

This is significantly different from the vibration metric in Equation 4.3. For the CH-53 [39], the vibrations are again reported as a magnitude, though this time in terms of linear spatial accelerations. The reduction in the magnitude for the CH-53 reported in Table 4.1 is the reduction in the cargo compartment, not at the hub as the BO-105 and UH-60 tests report.

The closed-loop vibration control tests of the IBC system on the CH-53 showed more promising results [40]. Multiple-harmonic inputs were used in an optimal control scheme based on selected vibration measurements. This allowed vibrations over multiple points on the airframe to be measured and minimized. Using 5P and 6P actuator inputs, the performance index based on vertical and lateral cargo compartment vibrations and lateral gearbox vibrations was reduced by 84%, as shown in Figure 4.4. In the figure, J[g] is the vibration performance index and AMPL5 and AMPL6 are the 5P and 6P amplitudes, respectively. The total amplitude does not exceed 0.3 degrees for this case of closed-loop control.

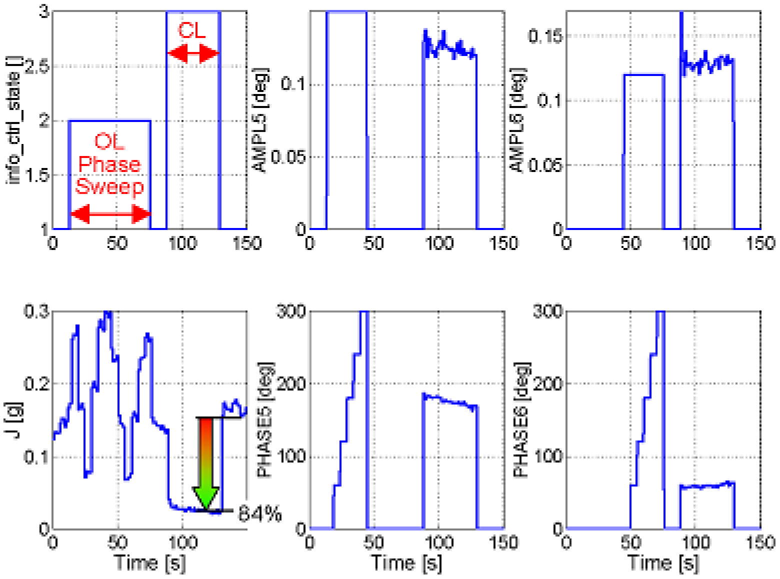

Figure 4.4: CH-53 Closed-Loop Vibration Reduction and Actuation Requirements at 70 kts [40].

Root pitch control pitches the entire blade, so large control deflections are not required. The forces required, however, are significant. The ZFL root pitch actuators were designed with maximum dynamic forces of about 4050 lbs. for the UH-60 and 4250 lbs. for the CH-53. These large required forces increase the bulk of the actuators and thus detract from their appeal unless there is a net weight reduction because the active vibration control allows for removal of isolators, absorbers, and other vibration canceling devices.

4.2.2 Trailing Edge Flap Control

While root pitch actuators have demonstrated themselves for individual blade control in flight tests, on-blade actuation holds appeal as an elegant alternative to the high actuation forces required of root pitch actuation and the complexity of placing hydraulics in the rotating frame. While other on-blade actuation methods show promise, trailing edge flaps show the most progress of the on-blade actuation methods toward implementation in a production helicopter. Gurney flaps (see Figure 4.5) are just recently being considered for vibration control [76]. Furthermore, trailing edge flaps can have discrete actuators, which are appealing for maintenance reasons, while active twist blades (see Figure 4.5) typically have embedded actuators. Given these circumstances, only TEFs will be investigated for on-blade control here. Vibration reduction capabilities, flap sizes, flap deflection, flap moments, and design concerns such as weight and centrifugal loading are examined here.

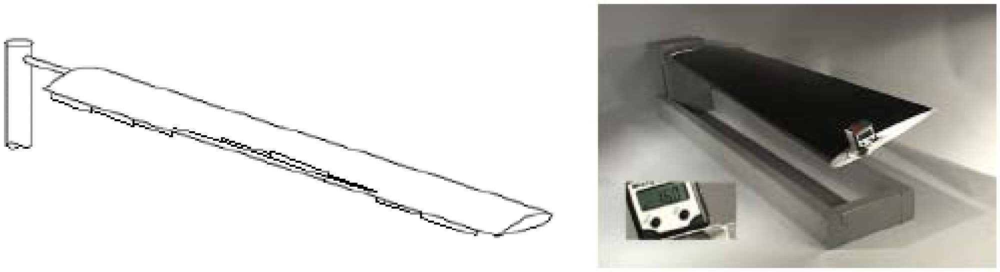

Figure 4.5: Distributed Gurney Flaps [70] and A Statically Deflected Active Twist Blade[71].

Recent work has progressed TEFs from computer simulation to flight tests. The primary challenge for TEF blade control is a set of constraints that dictates low actuator weight, low actuator volume, and minimum drag penalties while fulfilling flap actuation requirements. While there have been numerous studies on actuators and actuation mechanisms, the attempt here is to glean the actuator requirements for TEF control rather than focusing on the varied mechanisms to achieve that control with existing actuators.

Computer simulations of TEFs show promising results. Table 4.2 shows locations and sizes of the trailing edge flaps from selected simulations, and the projected vibration reductions using multiple harmonics.

Study Author	**Platform**	**Span**	**Chord**	**Span Location**	**Max. Flap Deflection**	**Max Vibe. Reduction**
Shen, Yang, and Chopra [44]	UH-60 Swashplateless	28%*R*	15%*c*	80%*R*	4.7 degrees	90%
Myrtle and Friedmann [45]	BO105	12%*R*	25%*c*	75%*R*	7 Degrees	96%
Viswamurthy and Ganguli [46]	BO105	12%*R*	20%*c*	70%*R*	2 degrees	73%

Table 4.2: Selected TEF Vibration Control Computer Simulation Results.

The vibration reductions here are either as reported directly by each study or are estimated from the figures from the study. All refer to the reduction in 4P vibrations—the dominant harmonic for these four-bladed rotors. While it appears the flaps in the study by Viswamurthy and Ganguli did not reduce vibration as much as the others, the vibration reduction reported there is the reduction in the magnitude of the hub vibration vector, which consists of 4P hub vertical, lateral, and longitudinal forces, and the 4P hub moments.

The vibration reductions for the other two studies in the table are for 4P vertical hub loads. Vibration reductions in Reference [45] are shown in Figure 4.6, and reductions in Reference [44] are depicted in Figure 4.7. The case reported in Table 4.2 for Reference [45] has a baseline vibration of “BASE-PLAIN” and controlled vibration of “ACF-PLAIN” in Figure 4.6.

Figure 4.6 also illuminates how vibration reduction capabilities change with blade torsional stiffness, which increases as the frequency of the first torsional mode, ω_{1T}, increases. The stiffer blade (Figure 4.6b) shows less reduction in loads, though the baseline longitudinal and lateral loads are higher for the softer blade (Figure 4.6a).

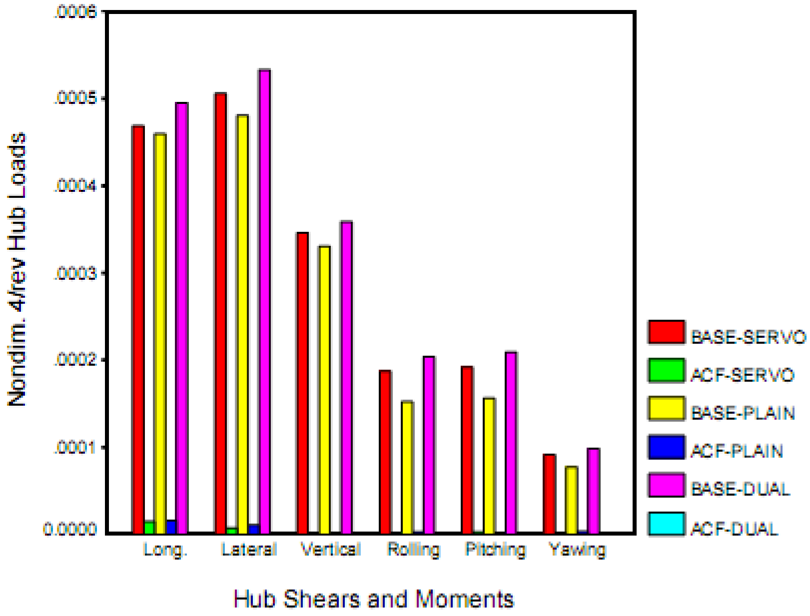

Figure 4.6a: Baseline and Controlled 4P Hub Loads for A Rotor with ω_{1T}=3.17P.

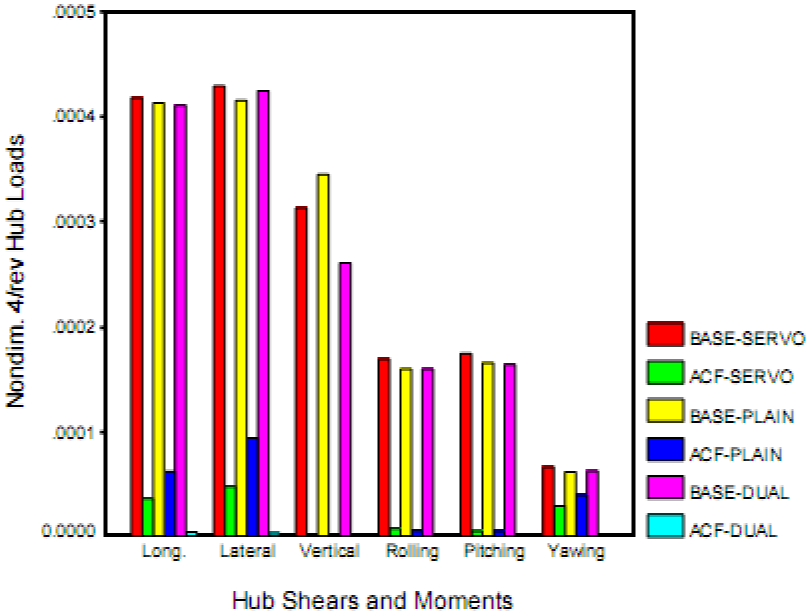

Figure 4.6b: Baseline and Controlled 4P Hub Loads for A Rotor with ω_{1T}=4.5P.

Figure 4.6: Predicted Baseline and Controlled 4P Hub Loads from Reference [45].

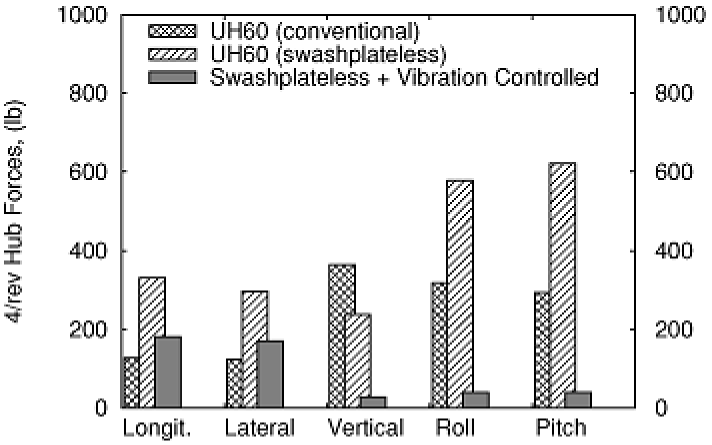

Figure 4.7: Predicted Baseline and Controlled 4P Hub Loads from Reference [44].

Another significant detail is that the deflection was limited to 2 degrees in Reference [46], while 7 degrees and 4.7 degrees of actuation were required in References [45] and [44], respectively. This is a relatively wide range of required deflections for vibration control, with the largest difference between the two models based on a BO-105 platform. The span locations for the flaps in the two BO-105 models, though, were very similar, and the chord ratios do not vary greatly. The span ratio of the UH-60 model [44] is greater because that model is also used for calculations regarding a swashplateless rotor. The flaps in Reference [44] must therefore have greater authority than is required for vibration reduction in order to have the authority necessary for primary control.

These computer simulations show great promise for TEFs for vibration control, but the investigation has not been limited to computer simulation. Various full scale tests have been performed. Boeing, in conjunction with DARPA, NASA, and other entities, has developed and wind tunnel tested a full-scale active flap rotor for the MD900 Explorer [47-55, 12]. Kawasaki Heavy Industries (KHI) and ATIC whirl-tower tested a TEF rotor [56] for which JAXA later improved and bench tested the actuators [57]. Diversified Technologies, Inc. and the U.S. Army whirl tower tested a TEF rotor for an OH-58 [58], and Eurocopter has flight tested a BK117 with a bearingless EC145 rotor equipped with TEFs [30, 59, 60]. The whirl tower tests can give insight into TEF actuation requirements, or at least actuator performance, while the wind tunnel and flight tests can illuminate possible real-world vibration reductions. Figure 4.8 displays these four TEFs. Table 4.3 details the flap parameters from these tests.

Figure 4.8a: MD900 SMART Rotor on Whirl Tower.

Figure4.8b: KHI/ATIC TEF

Figure 4.8c: DTI/Army Heliflap^{TM}

Figure 4.8d: Eurocopter ADASYS TEF Rotor Whirl Test

Figure 4.8: TEFs That Have Undergone Full Scale Testing

Organization	Platform	Test Type	Span	Chord	Span Location	Flap Used/Max. Flap	Max Vibe. Reduction
DARPA, Boeing, *et al.* [54]	MD900	Wind Tunnel	17.73%*R*	35%*c*	83%*R*	2 deg./4 deg.	95%
KHI/ATIC [56]	Test Rotor R=19 ft.	Whirl Tower	10%*R*	10%*c*	79.3%*R*	4 deg./4 deg.	N/A
DTI/ARMY [58]	OH-58	Whirl Tower	11.4%*R*	45.9%*c*	91.4%*R*	6 deg./8 deg.	N/A
Eurocopter [30,60]	BK117 w/ EC145 Rotor	Flight Test	10.9%*R*	17%*c*	74.5%*R*	2 deg./5 deg.	90%

Table 4.3: Full Scale TEF Rotor Tests.

While only two of these tests were able to examine vibration reduction capabilities, the results are promising. The Boeing wind tunnel test [54] produced an excellent reduction of hub normal loads by 95%, but this is a single-axis result and it is not reported how much this affected the vibration performance in the other axes. At the time of writing, the results from the multi-axis reductions had not been published. The Eurocopter test, however, shows the great possibility for reduction of hub loads by producing a maximum reduction of 90%. This reduction is the combination of vertical hub vibrations and vibratory pitching and rolling hub loads through use of a robust optimal controller. Lateral and longitudinal hub loads and the torsion moment were uncontrolled.

The flap sizes and locations are also of interest. The Heliflap™, the flap device used on the OH-58, has a significantly larger chord ratio than the other flaps. This size difference is because the design was focused on a proof of concept for the electromechanical actuator. The flap was subsequently sized to increase torque and to reduce electrical power, chordwise mass imbalance, and mechanical parts count. Of the rest, the Boeing TEF has the largest chord ratio and span ratio. The spanwise locations of the TEFs in all cases are within 10% of each other, when the OH-58 test is excluded. Though the OH-58 TEF test was run at only 81% of the nominal rotor speed, and the location and size of the flap in that study are dissimilar from the other studies, the fact that it used an electromagnetic actuator to actuate the flap up to 6 degrees at 4.4P, rather than the piezoelectric stacks used in the other studies, points to the possibility of other feasible actuation methods.

There are two approaches for TEF secondary control—moment flaps or lift flaps. A moment flap actuates such that the aerodynamic moment it generates pitches the entire blade. The blade pitch creates the desired control forces and moments. This method requires a torsionally soft blade or root pitch spring. The lift flap approach, as used for gust rejection by Montanye [11] and as investigated for vibration reduction by Kim [64], is intended to change the local blade coefficient of lift, and can be used on a torsionally stiff blade. Of the tests in Table 4.3, Boeing did not reduce the torsional stiffness of the MD900 blade to employ a servo effect—in fact, the first torsional frequency (ω_{1T}) was raised to 6.4P from the standard 6P on an MD900 rotor (the intent was to keep the value approximately the same). Conversely, the KHI (ω_{1T}=3.8P) and Eurocopter (ω_{1T}=3.3P) tests used low torsional stiffness root springs to utilize the servo effect of moment flaps. Figure 4.9 displays actuation efficiency for moment and lift based on blade chord ratio (flap chord/blade chord) to illustrate how these moment flaps are sized for the Eurocopter rotor. The lift and moment efficiencies are defined as the change in blade coefficient of lift (c_L) or moment (c_M) per change in flap deflection angle (δ_f) divided by the change in flap hinge moment coefficient (c_{fM}) per change in flap deflection angle, or,

$$\text{Lift Efficiency} = \frac{\partial c_L}{\partial \delta_f} \bigg/ \frac{\partial c_{fM}}{\partial \delta_f}, \qquad (4.5)$$

and

$$\text{Moment Efficiency} = \frac{\partial c_M}{\partial \delta_f} \bigg/ \frac{\partial c_{fM}}{\partial \delta_f}. \qquad (4.6)$$

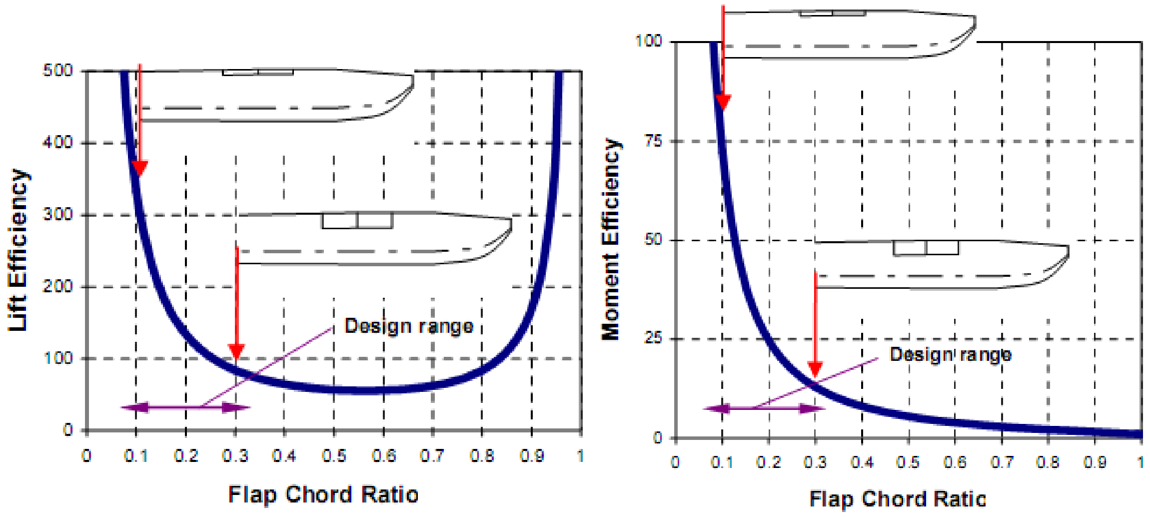

Figure 4.9: TEF Lift and Moment Efficiency v. Chord Ratio [60].

Rotor performance degradation presents a problem for active rotor vibration control using TEFs and other methods such as root pitch IBC. Deployment of a flap can increase the drag on a blade, and so decrease the efficiency of the rotor [62]. The same is true for pitching a blade. Conversely, 2P control of the rotor has been shown to increase the efficiency, often at the penalty of increased vibration levels [61]. Liu *et al.* [63] examined the tradeoffs between rotor performance and vibration reduction using TEFs for control in a computer simulation based on a BO105. Using optimal control, it was found that a 68% reduction in the vibration cost function and a 0.4% reduction in rotor power could be achieved when attempting to minimize both vibrations and rotor power consumed, excluding control power. This reduction in vibration was a composite of hub vibrations and not simply one axis, which shows promise for using TEFs for vibration control without decreasing rotor performance. The flap in this simulation had a chord ratio of 25%, a span ratio of 12%, and a spanwise center location at 75% *R*, which places it with the full-scale tests in terms of dimensions. The deflections of the flaps were less than 3 degrees for this simultaneous reduction. Figure 4.10 shows the motion of one flap over a revolution and the hub vibration levels. The “1 Flap” case is discussed here.

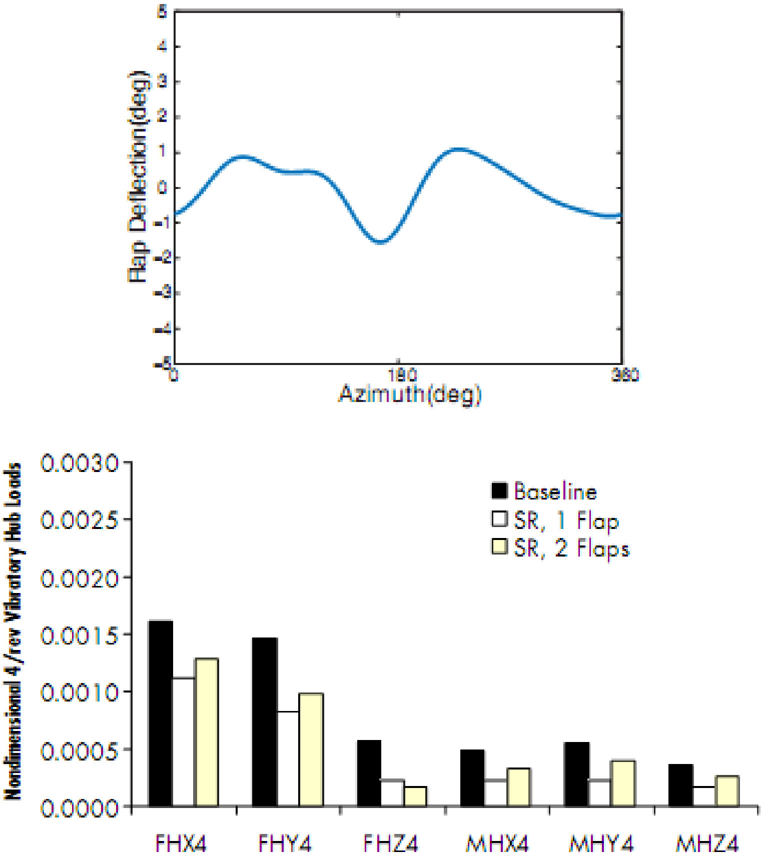

Figure 4.10: Simultaneous Power and Vibration Reduction Flap Deflection (Top) and Nondimensional 4P Hub Loads (Bottom) [63].

4.3 Comparing TEF and Root Pitch Control

While both TEFs and root pitch control appear to have promise for vibration reduction and show similar vibration reduction performance, the two remain quite different in actuation requirements. The hydraulic pitch link [35-39] shows that it is possible to scale root pitch actuation to meet the needs of larger helicopters, but it is questionable whether TEF actuation can be scaled in the same way due to constraints.

The diameter of the rotor increases as the Maximum Takeoff Weight, or MTOW, increases, as shown in Figure 4.11. This agrees with momentum theory, which says that the thrust is proportional to the rotor disk area. The best-fit polynomial increases with the square of the diameter, which is proportional to the disk area, accordingly. The tandem rotor helicopters' MTOWs in the figure are divided by 2 to give the MTOW per rotor. It is worthwhile to note that the BK117, MD900, EC135, EC145, Bell 427 and BO105 are clustered together. These are the size of helicopters that have been fitted with TEFs, while the larger helicopters have not.

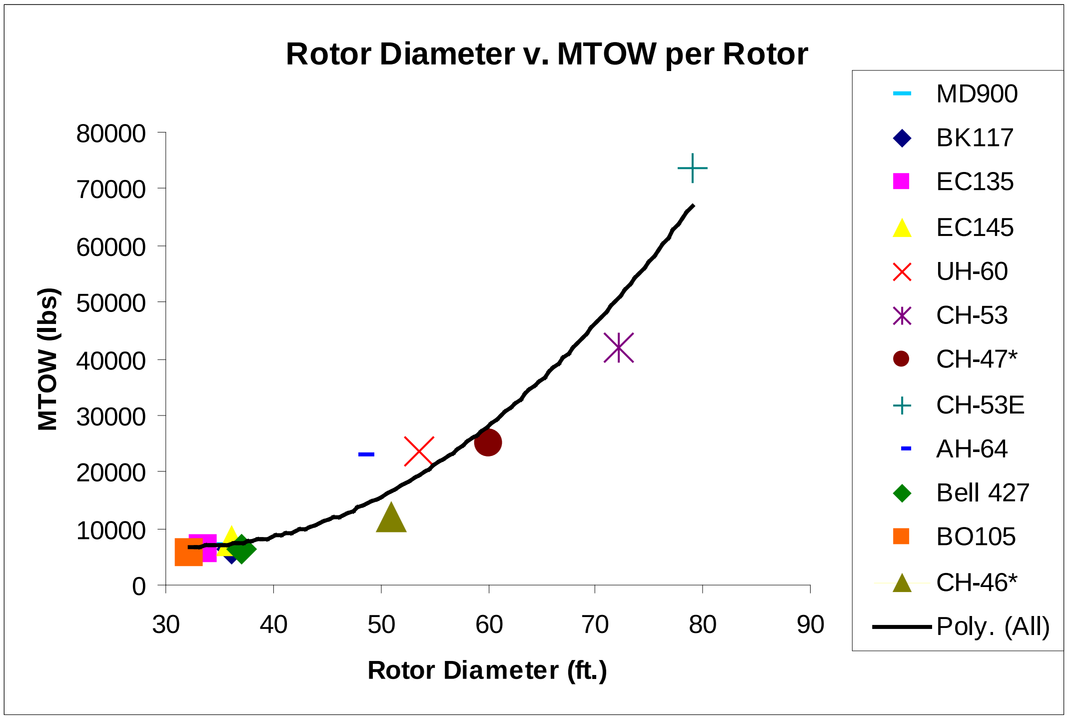

Figure 4.11: Rotor Diameter versus MTOW per Rotor.

One of the design challenges of placing actuators on the rotor is centrifugal loading. One would expect this to increase with rotor diameter for a given rotation rate, since centrifugal acceleration increases linearly as the radius increases. However, larger rotors have lower angular velocities, so that in fact, the centrifugal acceleration is lower at the tip than for smaller rotors. Figure 4.12 demonstrates the centrifugal acceleration along the blades of various rotors.

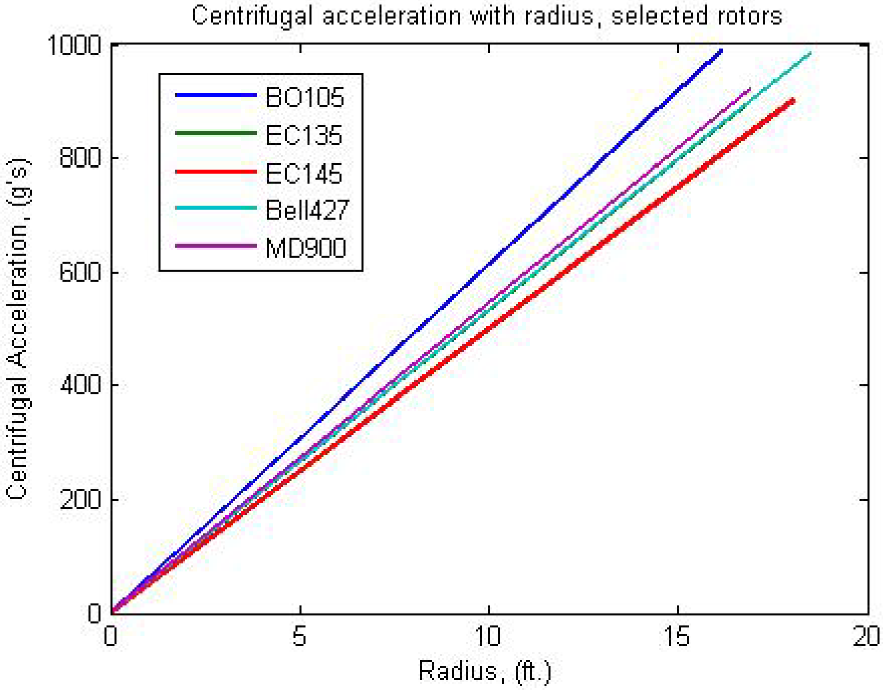

Figure 4.12a: Centrifugal Acceleration in Light Helicopter Rotors

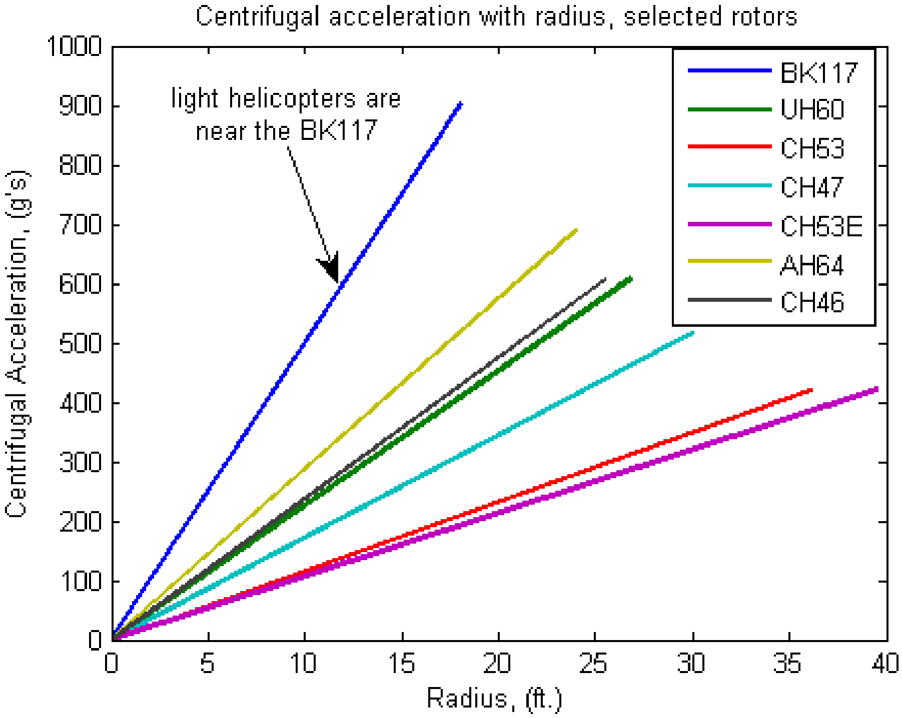

Figure 4.12b: Centrifugal Acceleration in Assorted Helicopter Rotors

Figure 4.12: Centrifugal Acceleration in Selected Rotors, Center to Blade Tip [53, 72-75].

The TEFs implemented in whirl tower, wind tunnel, and flight tests [54, 56, 58, 60] have been operating in the 700 to 800 g range. The same radial locations on larger helicopters would actually see lower centrifugal accelerations, on the order of 300 to 500 g's. This does not necessarily translate to lower forces because the mass of actuators for larger helicopters is bound to increase, probably with the rotor radius squared. The radial load each blade is able to withstand should increase with size as well.

Interestingly, the mass of the actuators for root pitch IBC does not increase with helicopter MTOW. Each UH-60 hydraulic pitch link weighs over 30 lbs, or 0.13% MTOW, and each hydraulic pitch link for the CH-53 comes to 22.5 lbs, or 0.05% MTOW. This decrease may be due, in part, to refinement and optimization of the actuator for the CH-53 from the earlier UH-60 design iteration. In comparison, the weight the TEF and actuator adds to the MD900 blade is about 5 lbs, or 0.07% MTOW [12]. While the weight savings based on these percentages appear to favor the root-pitch actuators, the power supply components for the root pitch hydraulic actuators can be expected to introduce more weight than the electrical components for the TEF piezoelectric stack actuators. These hydraulic components include hydraulic pumps, hydraulic fluid, oil coolers, and the hydraulic slip ring.

According to Kim [64], while the hinge moment for a TEF increases with the radius cubed, the force of a piezoelectric stack only increases with the radius squared, as shown in Figure 4.13. The stack's cross sectional area determines the maximum force it can exert, and the blade cross sectional area is proportional to the radius squared. This means that while stack actuators are capable for light helicopters, as size increases there is a rotor for which a single stack actuator of the same free stroke will not be able to provide enough authority due to size restrictions. Root pitch IBC actuation also has limitations on actuator size due to constraints in the hub, but these are likely not as severe as those for on-blade control.

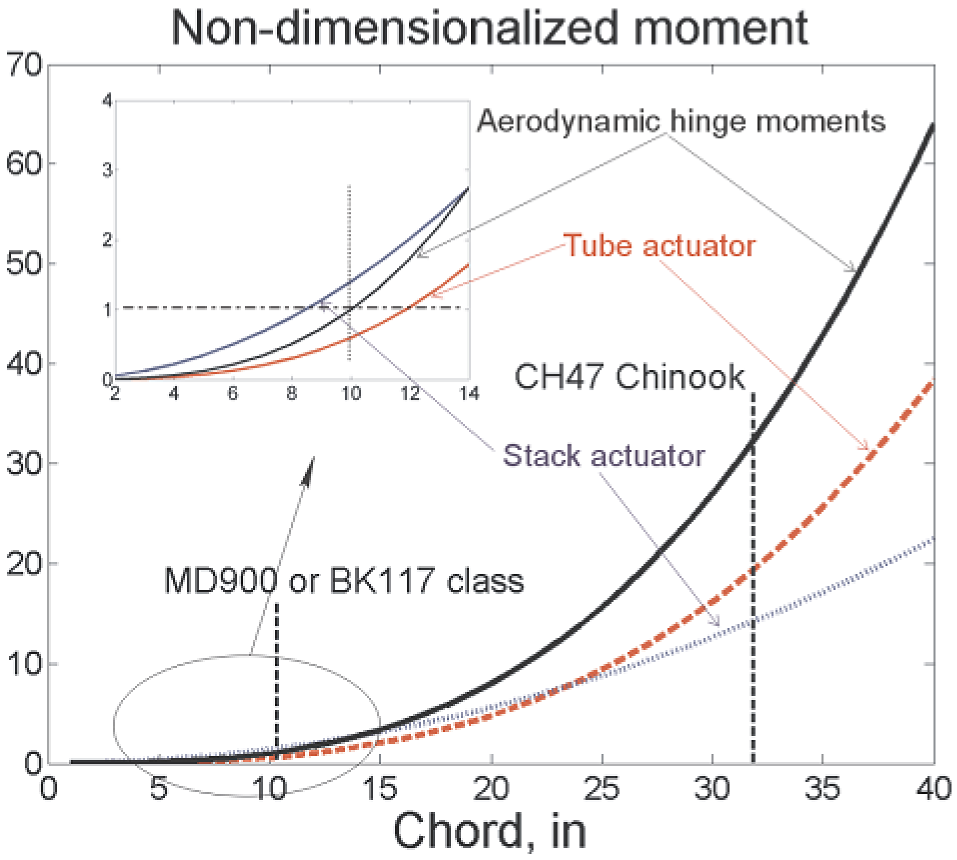

Figure 4.13: TEF Hinge Moment and Actuator Moment Increase with Chord [64].

While there are certainly challenges in actuation for both root pitch IBC and TEFs, TEFs retain an appeal because of the comparatively low actuation moments. The maximum dynamic actuation forces for the UH-60 and CH-53 hydraulic pitch links are 17% and 10% of the MTOW [24, 39]. The actuation force for the MD900 TEF is 1.6% of the MTOW at 113 lbs of block force [54]. The actual moments depend on the pitch horn length for the flap or the blade. For the UH-60, the hydraulic pitch link force of 4050 lbs., or 17% MTOW, translates to a maximum pitching moment of about 2025 ft-lbs., when using a pitch horn of 6 inches. In contrast, the block torque on the MD900 TEF, in conjunction with a pitch horn of 0.75 inches [12], provides a maximum moment of 7 ft-lbs. Scaling this with the radius cubed yields a maximum moment of about 28 ft-lbs for the same proportion flap on a UH-60. For emphasis, the maximum control moments are depicted in Figure 4.14.

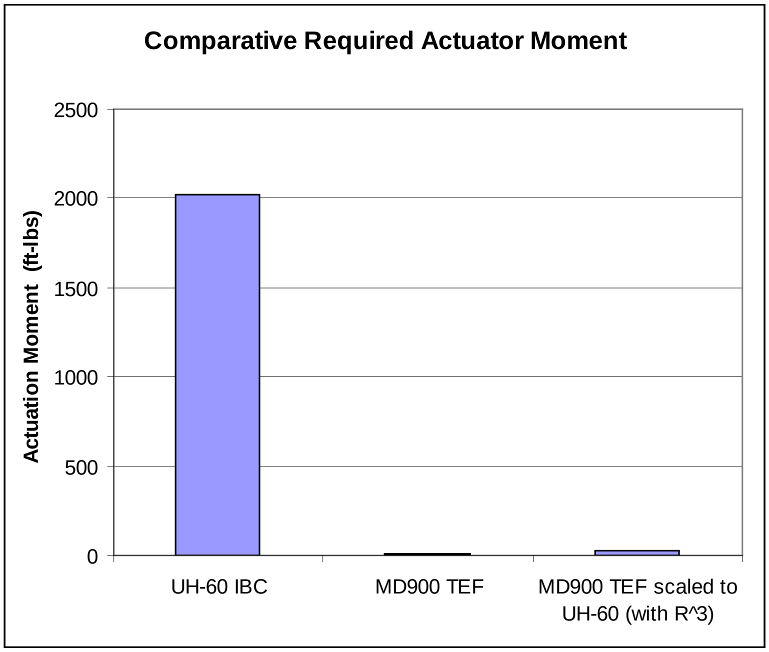

Figure 4.14: Root Pitch versus TEF Actuation Moments.

This comparatively low actuation force requirement in TEFs is promising for control system power consumption as well. Trailing edge flaps and root pitch IBC operate at the same frequencies, but as a conservative estimate for vibration control, assume the TEFs deflect up to 4 degrees. This gives an instantaneous angular velocity four times the rate of the root pitch actuator from the UH-60 wind tunnel test. The maximum instantaneous power at 3P (assuming the actuators could provide maximum force at the maximum rate) is then about 3820 ft-lbs./sec for the UH-60 root pitch actuation versus about 40 ft-lbs./sec for the MD900 flap. Even if the MD900 TEF scaled up with the radius cubed to approximate a TEF on a UH-60-sized blade, the power increases from the power required for the MD900 TEF by a factor of 2.5 when accounting for the change in rotor speed. The root pitch actuation on the UH-60 is many times costlier than TEFs when comparing peak power required, as can be seen in Figure 4.15. This brief exercise does not include inertial effects or direct aerodynamic calculations, but does suggest a clear control power advantage with TEFs, even if actuators can not be found to fit the design constraints.

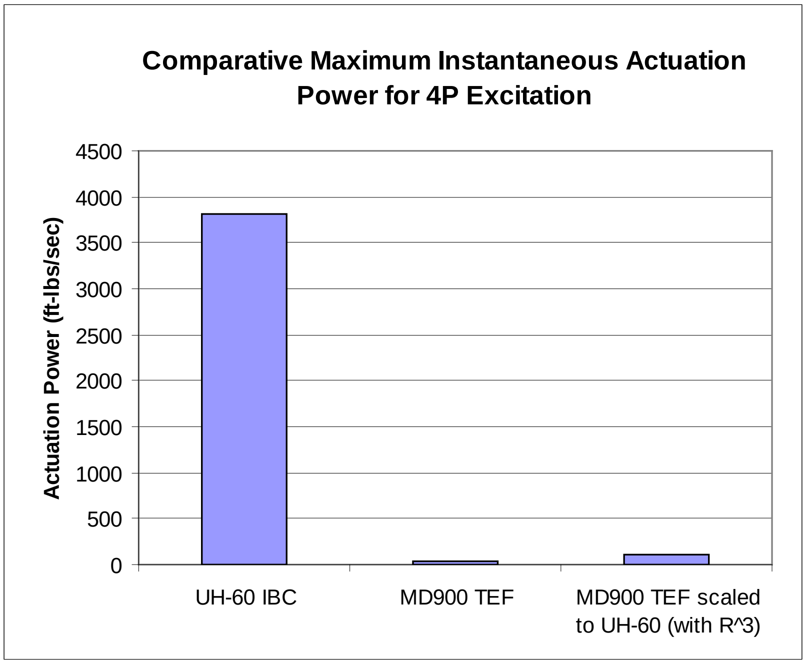

Figure 4.15: Root Pitch versus TEF Maximum Instantaneous Actuation Power.

TEFs also have the advantage of directly controlling loads near the blade tip, where the greatest resultant hub moments are generated. Torsional dynamics of the blade delay blade tip response to root pitch actuation [35]. The effects of torsional dynamics on blade tip response from the BO-105 wind tunnel test are displayed in Table 4.4. The input amplitude was not specified, though elsewhere the study used one degree of root pitch input. Notice the phase lag and amplitude difference at the tip due to torsional dynamics. The increase in amplitude from 3P to 4P is probably because the first torsion mode of the blades in this test was 3.6P, so that the 4P forcing was closer to the resonant frequency. The faster generation of hub moments when using a trailing edge flap could be coupled to an on-blade feedback controller to further improve response time, which could possibly improve closed-loop vibration reduction capabilities in transient flight conditions. For root pitch control, it is possible that torsionally rigid blades can help to improve root pitch response time.

IBC Root Input	Amplitude at Blade Tip, degrees	Phase Lag at Tip, degrees Azimuth	Phase Lag at Tip, degrees N_bP
2P	0.60	10	20
3P	0.50	13	39
4P	0.58	33	132
5P	0.21	42	210
6P	0.15	34	204

Table 4.4: Root Pitch Blade Attenuation and Phase Shift Due to Blade Torsional Dynamics [35].

4.4 Recommendations

The literature review in this chapter shows that root pitch control has the advantage of leaving the blade structurally and aerodynamically unaltered, whereas TEFs may impose additional drag penalties. Conversely, TEFs have the potential to have faster response time than root pitch IBC. If the swashplate is retained and it is desirable to have a decoupled secondary control system, then TEFs are ideal. Vibrations can be reduced and no additional rotor power is needed with proper control. Minimal weight is added to accomplish control because small actuators can be used for vibration reduction. The primary control system is not compromised as it is with root pitch actuators, which place secondary control actuators in the load path.

If the swashplate is removed as the primary control system and it is desired that root pitch control or TEFs should provide primary as well as secondary control, then root pitch actuation is recommended. To provide sufficient authority for primary control, TEFs would most likely use the servo effect to pitch the entire blade, requiring less control power than root pitch, but adding drag penalties. Both methods are capable of the secondary control functions. The total power consumed by the TEF rotor, including shaft power and TEF control power, may be more or less than the total power consumed by the root pitch rotor.

Actuators play a key role in the specification of an on-blade control system. If the rotor is large, current actuators may not be sufficient for primary or secondary control. There may be methods to place actuators at the hub with an internal linkage to reach the flap so that actuator size is less of a concern. In this case the complexity of the system increases and TEFs are less practical. Centrifugally-pumped pneumatic actuation may provide enough authority for some tasks with TEFs [65] or an actuator may be developed with enough energy density to perform the necessary functions. In any case, TEFs cannot be actuated sufficiently on large rotors with the current methods, whereas root pitch control has already been flight tested on a large helicopter and has been shown to reduce vibrations. The movement from hydraulic systems to all-electric root-pitch actuation shows the most promise for IBC implementation in large helicopters.

The earlier comparison of actuation force available from piezoelectric actuators in small and large blades focused a single actuator. This kept the stroke the same, so that the length of a stack was constant, but increased the cross-section to increase force. The single actuator was not able to provide enough force for TEFs on rotors with large chords, even with the increased cross-section. Placing multiple actuators to act in parallel along the length of the spar may be able to provide the force required to actuate the blade, at the cost of increased weight and centrifugal loading. If the hinge moment increases as the square of the increasing flap chord and linearly with increasing flap span [57], then the energy required for a given deflection will increase as cubic with rotor radius. The energy for TEF actuation should then be paired with spar volume to determine the energy density needed for the TEF actuator, which in turn illuminates the current limits of on-blade TEF actuation. Of course, the maximum actuator size may be reduced because of other constraints, such as buckling due to centrifugal loading, heat dissipation, or blade stresses.

The lag between root pitch actuation and blade tip response due to blade torsional dynamics should be studied further. Future work should investigate the lag between actuation and the generation of the desired hub moment or shear for both root pitch IBC and TEFs. The method which has less delay may be more appealing for an on-blade feedback controller.

With current technology, root pitch IBC shows the most promise for secondary control and swashplateless primary control on medium and heavy helicopters. TEFs show great promise for light helicopters, and with advances in actuation could serve on heavier helicopters for both secondary and primary control. TEFs are an elegant control solution because of lower control power requirements, but further studies must be done to compare TEF rotor performance with root pitch performance and to investigate the energy density requirements for TEF actuators.

Chapter 5

Conclusion

5.1 Conclusions

Helicopter rotors have the potential for much more than primary flight control. With the help of secondary flight control such as vibration reduction, rotor performance enhancement, gust alleviation, BVI noise reduction, and other individual blade control options, helicopters can become safer for pilots and passengers due to reduced gust response and vibrations. Additionally, helicopters can become more economical because of increased performance and decreased fatigue and more accepted in communities because of reduced external noise. The promises of IBC are great, but so are the design challenges.

This work creates a nonlinear inverse kinematic model of the swashplate mechanism for the purposes of investigating the effect of shipboard gust alleviation on the swashplate actuators. This model also includes dynamics, which can be modified easily to include a more advanced model of the blade aerodynamic moments. Additionally, helicopters other than the UH-60 may be evaluated by changing relevant parameters.

The swashplate AWC and the TEF AWC perform similarly, but the swashplate AWC requires more actuator motion. All motions and forces are well within actuator capabilities, and metal fatigue is not a concern. Based on combined actuator travel, the swashplate actuators experience 45% more travel in the swashplate AWC case than the TEF AWC case. Unfortunately, this extra motion could result in additional seal wear, especially if particulates are present in the hydraulic fluid. Failure of one of these actuators could be catastrophic, but the amount of wear due to shipboard gust alleviation alone should be only a small portion of the total wear experienced from all flight conditions combined. Using swashplate-based gust alleviation for atmospheric gusts as well would most likely increase component wear. TEF-based gust alleviation has significantly less impact on the wear of the swashplate primary flight control actuators.

TEFs are not the only form of IBC. An investigation of TEFs and root pitch control shows both are similarly capable in terms of vibration reductions, with reductions on the order of 80% to 90%. From a performance standpoint, TEFs have the disadvantage of increased drag, but proper control can minimize drag penalties and still provide good vibration reduction. The additional advantage of low control power requirements combined with the other advantages makes TEFs better than root pitch control for secondary control. Current actuation technology, however, does not meet the actuation requirements for TEFs on medium and heavy helicopters.

5.2 Recommendations for Future Work

This study focuses on the effect of swashplate and TEF–based gust alleviation on the primary actuators and the comparison of root pitch and TEF individual blade control methods. When comparing gust alleviation methods, flight conditions are limited to dynamic interface operations, but it may be possible to design controllers to reject atmospheric gusts as well. It is posited that the reliability concerns for gust alleviation in forward flight would be similar to those in DI operations, but further study is required to prove or disprove this hypothesis. Additionally, a forward flight model requires an updated aerodynamic model for the blades that accounts for the effects of varying relative velocity and changing angles of attack on the blade root moments. It may be expedient to calculate blade pitches, flap, lag, and moments in another model and to use those values as the input for this model.

This study is limited to investigation effects of the two controllers on the swashplate actuators. For a comparison of the overall reliability of a TEF-based AWC or a swashplate-based AWC, other components besides the primary actuators are also of interest. Further study should examine the reliability of TEFs and all associated components in addition to swashplate reliability concerns to determine the reliability of the system as a whole. Similar reliability comparisons can be made with root pitch actuation.

A simulation of root pitch and TEF control should be developed to investigate the response time differences as well as the variations in the control and rotor power requirements of the two control schemes. Blade tip response time is of particular interest for on-blade feedback control, which has the possibility of improving control of transient disturbances. Required actuation energy should also be investigated to discover the limits of current on-blade actuator technology in terms of blade chord, span, and rotation rate, which can then be used to determine helicopter size limits for current actuation technology. This process could allow further research toward developing swashplateless rotors and helicopters with improved safety, comfort, performance, and public acceptance.

Appendix A

Modeling Methods

A.1 Derivation of ν and γ for Haug's Method

Starting with the constraint vector, **Φ**, the solution to the position analysis of a mechanism is **Φ**=0, which gives, when differentiated,

$$\dot{\Phi} = \frac{d\Phi}{dt} = 0 \quad , \tag{A.1}$$

$$\dot{\Phi} = \frac{\partial}{\partial \mathbf{q}}(\Phi)\frac{d\mathbf{q}}{dt} + \frac{\partial \Phi}{\partial t} \quad , \tag{A.2}$$

and subsequently,

$$\frac{\partial}{\partial \mathbf{q}}(\Phi)\dot{\mathbf{q}} = -\frac{\partial \Phi}{\partial t} = \boldsymbol{\nu} . \tag{A.3}$$

The partial derivative of the constraint vector with respect to **q** is the Jacobian, **J**. Solving for the generalized coordinate velocity gives,

$$\dot{\mathbf{q}} = -\left[\frac{\partial}{\partial \mathbf{q}}(\Phi)\right]^{-1} \frac{\partial \Phi}{\partial t} = -\mathbf{J}^{-1}\boldsymbol{\nu} . \tag{A.4}$$

Similarly, this can be done with the acceleration right-hand-side, **γ**, by taking the time derivative of Equation A.4,

$$\frac{d}{dt}\left[\frac{\partial}{\partial \mathbf{q}}(\Phi)\right] = -\frac{d}{dt}\left[\frac{\partial \Phi}{\partial t}\right], \tag{A.5}$$

$$\frac{\partial}{\partial \mathbf{q}}(\Phi)\ddot{\mathbf{q}} + \left[\frac{\partial}{\partial \mathbf{q}}\left(\frac{\partial}{\partial \mathbf{q}}(\Phi)\dot{\mathbf{q}}\right) + \frac{\partial}{\partial t}\left(\frac{\partial}{\partial \mathbf{q}}(\Phi)\right)\right]\dot{\mathbf{q}} = \frac{\partial^2}{\partial \mathbf{q}\partial t}(\Phi)\dot{\mathbf{q}} - \frac{\partial^2}{\partial t^2}(\Phi), \tag{A.6}$$

$$\frac{\partial}{\partial \mathbf{q}}(\Phi)\ddot{\mathbf{q}} = \frac{\partial^2}{\partial \mathbf{q}\partial t}(\Phi)\dot{\mathbf{q}} - \frac{\partial^2}{\partial t^2}(\Phi) - \left[\frac{\partial}{\partial \mathbf{q}}\left(\frac{\partial}{\partial \mathbf{q}}(\Phi)\dot{\mathbf{q}}\right) + \frac{\partial}{\partial t}\left(\frac{\partial}{\partial \mathbf{q}}(\Phi)\right)\right]\dot{\mathbf{q}} = \boldsymbol{\gamma}, \tag{A.7}$$

$$\ddot{\mathbf{q}} = -\mathbf{J}^{-1}\boldsymbol{\gamma}, \tag{A.8}$$

which gives a solution for the coordinate accelerations.

A.2 Chace's Vector Method

This section includes additional material on Chace's method of linkage analysis from Chapter 1.

CASE	Unknown	Known	Solution
1	$s, \hat{s}$	C,t	**s**= - (**C**+**t**)
2	s,t	**C**, $\hat{s}, \hat{t}$	$\mathbf{s} = -\left[\frac{\mathbf{C} \bullet (\hat{t} \times \hat{k})}{\hat{s} \bullet (\hat{t} \times \hat{k})}\right]\hat{s}$ $\mathbf{t} = -\left[\frac{\mathbf{C} \bullet (\hat{s} \times \hat{k})}{\hat{t} \bullet (\hat{s} \times \hat{k})}\right]\hat{t}$
3	$\hat{s}, t$	**C**, $s, \hat{t}$	$\mathbf{s} = \left[-\mathbf{C} \bullet (\hat{t} \times \hat{k})\right](\hat{t} \times \hat{k}) \pm \left\{s^2 - \left[\mathbf{C} \bullet (\hat{t} \times \hat{k})\right]^2\right\}^{\frac{1}{2}}\hat{t}$ $\mathbf{t} = \left[-(\mathbf{C} \bullet \hat{t}) \mp \left\{s^2 - \left[\mathbf{C} \bullet (\hat{t} \times \hat{k})\right]^2\right\}^{\frac{1}{2}}\right]\hat{t}$
4	$\hat{s}, \hat{t}$	**C**,s,t	$\mathbf{s} = \mp\left[t^2 - \left(\frac{C^2 + t^2 - s^2}{2C}\right)^2\right]^{\frac{1}{2}}(\hat{C} \times \hat{k}) + \left(\frac{C^2 + t^2 - s^2}{2C} - C\right)\hat{C}$ $\mathbf{t} = \pm\left[t^2 - \left(\frac{C^2 + t^2 - s^2}{2C}\right)^2\right]^{\frac{1}{2}}(\hat{C} \times \hat{k}) - \left(\frac{C^2 + t^2 - s^2}{2C}\right)\hat{C}$

Table A.1: Solutions to the vector triangle equation. [14]

Case	Unknowns	Vectors	Scalars	Order of Polynomial
1	r,θ_r,ϕ_r	$\mathbf{C}$		1
2a	r,θ_r,s	$\mathbf{C},\hat{\omega}_r,\hat{s}$	ϕ_r	2
2b	r,θ_r,θ_s	$\mathbf{C},\hat{\omega}_r,\hat{\omega}_s$	ϕ_r,s,ϕ_s	4
2c	θ_r,ϕ_r,s	$\mathbf{C},\hat{s}$	r	2
2d	θ_r,ϕ_r,θ_s	$\mathbf{C},\hat{\omega}_s$	r,s,ϕ_s	2
3a	r,s,t	$\mathbf{C},\hat{r},\hat{s},\hat{t}$		1
3b	r,s,θ_t	$\mathbf{C},\hat{r},\hat{s},\hat{\omega}_t$	t,ϕ_t	2
3c	r,θ_s,θ_t	$\mathbf{C},\hat{r},\hat{\omega}_s,\hat{\omega}_t$	s,ϕ_s,t,ϕ_t	4
3d	$\theta_r,\theta_s,\theta_t$	$\mathbf{C},\hat{\omega}_r,\hat{\omega}_s,\hat{\omega}_t$	$r,\phi_r,s,\phi_s,t,\phi_t$	8

Table A.2: Cases of Solutions to the Vector Tetrahedron Equation. [15]

Once a position solution is obtained using the generalized solutions above for a three-dimensional or a planar mechanism, the velocities and accelerations of the joints and links are found by taking the first and second time derivatives of the position vectors, respectively. For three dimensions,

$$\frac{d\mathbf{r}}{dt} = \mathbf{v}_{PQi} = \left(\frac{dr}{dt}\right)\hat{\mathbf{r}} + \left(\boldsymbol{\omega}_i \times \mathbf{r}\right) \tag{A.9}$$

$$\frac{d^2\mathbf{r}}{dt^2} = \mathbf{a}_{PQi} = \left(\frac{d^2 r}{dt^2}\right)\hat{\mathbf{r}} + \boldsymbol{\omega}_i \times \left(\boldsymbol{\omega}_i \times \mathbf{r}\right) + \left(\boldsymbol{\alpha}_i \times \mathbf{r}\right) + 2\left[\boldsymbol{\omega}_i \times \left(\frac{dr}{dt}\right)\hat{\mathbf{r}}\right] + \sum_{j=3}^{i}\left[\left(\boldsymbol{\omega}_{j-1} \times \boldsymbol{\omega}_{j,j-1}\right) \times \mathbf{r}\right] \tag{A.10}$$

where $\boldsymbol{\omega}_{i,i-1}$ is the angular velocity of link *i* with respect to link *i*-1. In two dimensions, these equations become,

$$\mathbf{v}_{PQ} = \frac{\partial \mathbf{r}_{PQ}}{\partial t} = \left(\frac{dr}{dt}\right)\hat{\mathbf{r}} + \omega_i (\hat{\mathbf{k}} \times \mathbf{r}) \tag{A.11}$$

$$\mathbf{a}_{PQ} = \frac{\partial^2 \mathbf{r}}{\partial t^2} = \left(\frac{d^2 r}{dt^2} - \omega_i{}^2 r\right)\hat{\mathbf{r}} + \left[\alpha_i r + 2\left(\frac{dr}{dt}\right)\omega_i\right]\left(\hat{\mathbf{k}} \times \hat{\mathbf{r}}\right) \tag{A.12}$$

where $\hat{\mathbf{k}}$ is a unit vector perpendicular to the plane in which the mechanism lies.

To illustrate this method, take the example of a planar offset slider-crank, as seen in Figure 2 below.

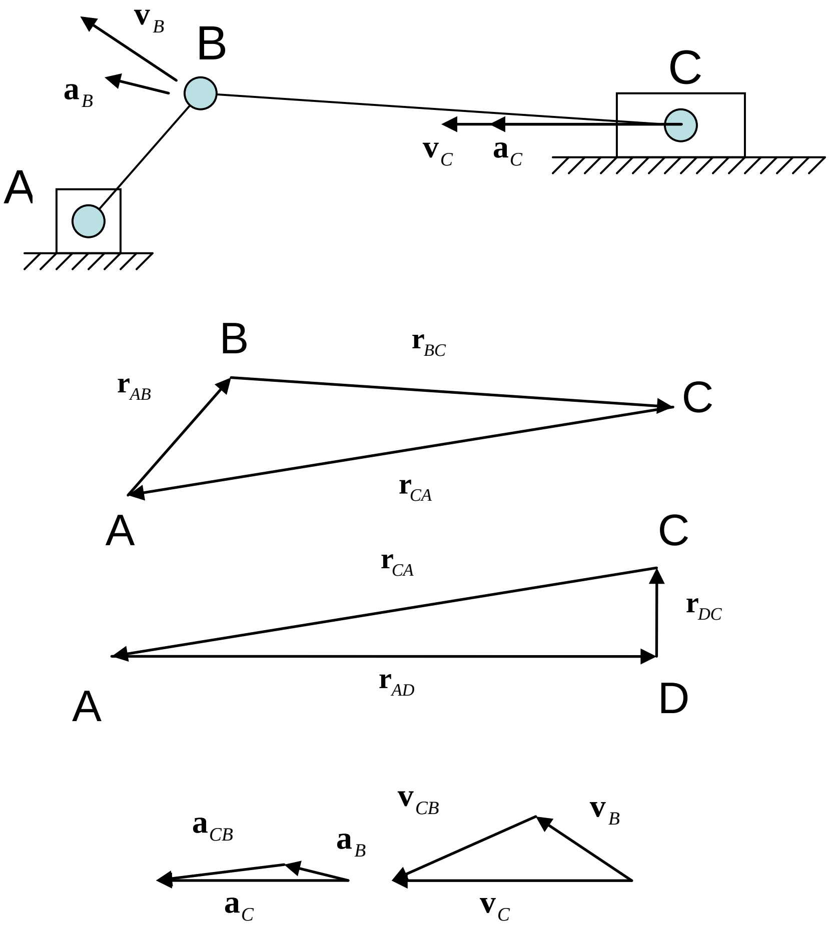

Figure A.1: Offset Slider-Crank Mechanism and Associated Vector Triangles.

At first glance this problem seems very simple to set up, given that there are three joints, A, B, and C, to consider, and so the very geometry is a triangle. But once the first triangle in Figure 2 is drawn, it becomes apparent that there are more than two unknowns in the triangle. Once the offset distance of the slide is included by incorporating the information in triangle ADC, this problem is solved, and the loop equation becomes:

$$\mathbf{C} + r_{BC}\hat{\mathbf{r}}_{BC} + r_{DA}\hat{\mathbf{r}}_{DA} = 0 \tag{A.13}$$

where,

$$\mathbf{C} = r_{AB}\hat{\mathbf{r}}_{AB} - r_{DC}\hat{\mathbf{r}}_{DC}\,. \tag{A.14}$$

Now taking $\mathbf{s} = \mathbf{r}_{BC}$ and $\mathbf{t} = \mathbf{r}_{DA}$ puts the loop equation in standard form where the unknowns are $\hat{\mathbf{s}}$ and t. The solution can be extracted easily from case 3 in Table 1.

To solve for velocities and accelerations, create the velocity and acceleration triangles as shown in Figure 2. Once again make loop equations where:

$$\mathbf{v}_B + \mathbf{v}_{CB} - \mathbf{v}_C = 0 \tag{A.15}$$

$$\mathbf{a}_B + \mathbf{a}_{CB} - \mathbf{a}_C = 0 \tag{A.16}$$

Now to solve these last two loop equations, differentiate the position vectors and insert them in the appropriate locations, then take dot products to solve for the unknowns. The solutions are as follows:

$$\omega_{BC} = \frac{-\omega_{AB}\left(\hat{\mathbf{k}} \times \mathbf{r}_{AB}\right) \bullet \left(\hat{\mathbf{r}}_{DA} \times \hat{\mathbf{k}}\right)}{\left(\hat{\mathbf{k}} \times \mathbf{r}_{BC}\right) \bullet \left(\hat{\mathbf{r}}_{DA} \times \hat{\mathbf{k}}\right)} \tag{A.17}$$

$$\dot{r}_{DA} = \omega_{AB}\left(\hat{\mathbf{k}} \times \mathbf{r}_{AB}\right) \bullet \hat{\mathbf{r}}_{DA} + \omega_{BC}\left(\hat{\mathbf{k}} \times \mathbf{r}_{BC}\right) \bullet \hat{\mathbf{r}}_{DA} \tag{A.18}$$

$$\alpha_{BC} = \frac{\left(\omega_{AB}{}^{2}\mathbf{r}_{AB} + \omega_{BC}{}^{2}\mathbf{r}_{BC}\right) \bullet \left(\hat{\mathbf{r}}_{DA} \times \hat{\mathbf{k}}\right)}{r_{BC}\left(\hat{\mathbf{k}} \times \hat{\mathbf{r}}_{BC}\right) \bullet \left(\hat{\mathbf{r}}_{DA} \times \hat{\mathbf{k}}\right)} \tag{A.19}$$

$$\ddot{r}_{DA} = \left[-\omega_{AB}{}^{2}\mathbf{r}_{AB} - \omega_{BC}{}^{2}\mathbf{r}_{BC} + \alpha_{BC} r_{BC}\left(\hat{\mathbf{k}} \times \hat{\mathbf{r}}_{BC}\right)\right] \bullet \hat{\mathbf{r}}_{DA} \tag{A.20}$$

Performing a force analysis on this two-dimensional linkage is an application of Newtonian mechanics in vectors. For instance, if a force, F, is applied at rest to the slider that points in the $\hat{\mathbf{r}}_{AD}$ direction, then the torque required to hold the slider at rest, assuming massless, infinitely rigid, frictionless links, would be $-\left(\mathbf{r}_{AB} \times F\hat{\mathbf{r}}_{AD}\right)$ applied to the crank. Similarly, forces and torques which include the effects of friction, mass, and moving bodies can be found using basic vector methods.

Appendix B

Kinematic Model Validation

Ideally, any model would be validated by experimental data from flight tests. Such data was unavailable at the time of this writing. In light of this, a few checks are made to the model to investigate whether it operates as intended. These cannot divulge the accuracy of assumptions, but they can shed light on the workings of the swashplate mechanism.

The first test is to see the effect of rotor collective pitch on swashplate motion. The rotor is made to have ten degrees collective pitch and no cyclic pitch. One would expect all three actuators to move vertically the same amount. The extensions of the actuators and the vertical motion of the swashplate are shown in Figure B.1.

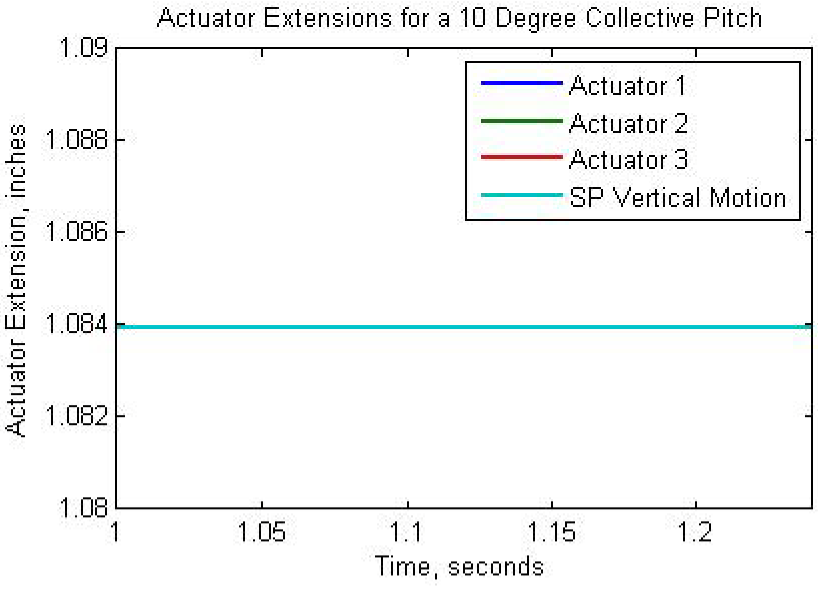

Figure B.1: Actuator Extensions for a Collective Pitch of θ_{col}=10 degrees.

The actuator extensions and the swashplate vertical motion are all the same, as should be the case for a collective-only condition. Moreover, applying values to Equation 2.5 gives,

$$\begin{bmatrix} 13.9 \\ -5.57 \\ 17 \end{bmatrix} + \begin{bmatrix} 2.36 \\ 5.89 \\ -1.42 \end{bmatrix} = \begin{bmatrix} 16.16 \\ 0 \\ 0 \end{bmatrix} + z_{col}\mathbf{E}_3 + \mathbf{c}_{PL}\,, \qquad \text{(B.1)}$$

in the {$\mathbf{a}_1$, $\mathbf{a}_2$, $\mathbf{a}_3$} basis. Using Equation 2.9 determines the vertical motion, in inches,

$$z_{col} = 15.58 - \sqrt{14.5^2 - 0.12^2 - 0.32^2} = 1.084\,. \qquad \text{(B.2)}$$

This is the same as the result from the simulation within rounding error.

A similar approach is used for the swashplate cyclic pitches. The rotor is made to have a lateral cyclic pitch of ten degrees. The vertical motions of the joints of the pitch links and the swashplate for one rotor revolution are plotted in Figure B.2.

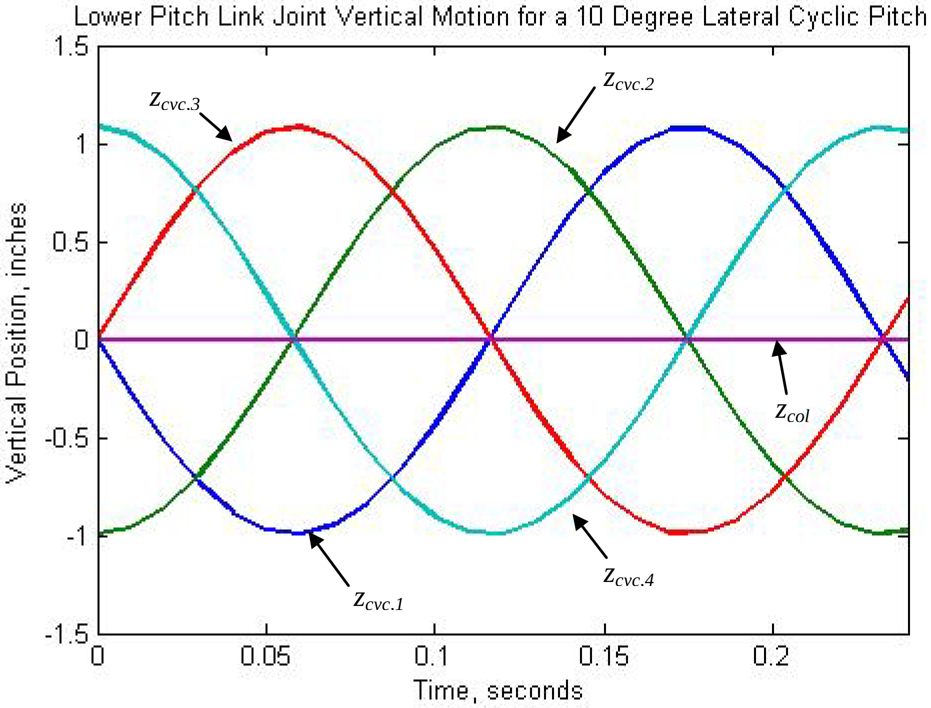

Figure B.2: Lower Pitch Link Joint Motion for θ_{col}=0 and θ_{1C}=10 degrees.

Interestingly, the sinusoidal curve for the vertical motion of each pitch link is not symmetric about the mean value (zero, in this case). This discrepancy between up and down displacements is because the pitch horn on the blade is generally not oriented horizontally. This means that different magnitudes of vertical motion are required to provide a pitch-up angle and a pitch-down angle of each blade.

The simulation code for the cyclic pitch is verified by applying Equation 2.10 and Equation 2.16. For the maximum and minimum values, the blade angle, θ_i, is known. For example, when finding the maximum vertical position of a lower pitch link joint Equation 2.10 becomes,

$$\begin{bmatrix} 13.9 \\ -5.57 \\ 17 \end{bmatrix} + \begin{bmatrix} 2.36 \\ 5.89 \\ -1.42 \end{bmatrix} - 16.16 \begin{bmatrix} \cos(\eta) \\ 0 \\ \sin(\eta) \end{bmatrix} = 14.5\left(\hat{\mathbf{c}}_{PL}\right). \tag{B.3}$$

The value of η is determined using Equation 2.16, which becomes,

$$\eta = 2\tan^{-1}\left(\frac{15.58 - \sqrt{15.58^2 - 33.53*1.01}}{33.53}\right) = 0.067 \text{ radians.} \tag{B.4}$$

This angle is then applied to Equation 2.11, giving (in the $\{\mathbf{a}_1, \mathbf{a}_2, \mathbf{a}_3\}$ frame),

$$\mathbf{r}_p = \begin{bmatrix} 16.12 \\ 0 \\ 1.08 \end{bmatrix}, \tag{B.5}$$

which has the same value for the vertical position of the lower pitch link joint as is returned from the simulation when the pitch link reaches its maximum vertical displacement due to a ten-degree lateral cyclic pitch. This procedure is also used to check the minimum values.

The solution to $\mathbf{c}_{PL}$ also provides some insight into the workings of the mechanism. Now that η is known, $\mathbf{c}_{PL}$ becomes (with very little rounding to preserve the length constraint):

$$\mathbf{c}_{PL} = \begin{bmatrix} 0.1364 \\ 0.32 \\ 14.4958 \end{bmatrix}. \qquad \text{(B.6)}$$

This result for $\mathbf{c}_{PL}$ shows that the pitch link tilts from vertical due to cyclic blade pitch. In fact, a constant tilt is introduced when a collective blade pitch is applied, and a cyclic tilt occurs due cyclic blade pitch. This could be useful knowledge when designing a component that interacts with the pitch link.

The next step in verification of the kinematic model is to determine the effect of rotor cyclic on the actuator extensions. Ideally, the swashplate orientation should determine the rotor cyclic pitches rather than the other way around. Imposing the constraint of sinusoidal rotor cyclic as discussed in Equation 2.4 requires the vertical displacement of each lower pitch link joint to follow a harmonic shape that has the same mean value and period as the cyclic pitch of the blade, but with maximum and minimum values that are different distances from the mean as shown in Figure B.2. This is imposed by the nonlinearities of the control linkage as described previously. This variation in displacement would mean the swashplate would have to “wobble”, or to move at high frequencies, to attempt to meet the rotor cyclic constraint. This “wobble” is due to the inaccuracy of the convention of modeling the blade pitch as in Equation 2.4. The magnitude of the “wobble” decreases as average pitch horn orientation approaches horizontal.

To compensate for this “wobble”, the swashplate angles are filtered using a windowed moving average. The nominal swashplate angles are the end result. The unfiltered actuator motions over one rotor revolution are depicted in Figure B.3, and the filtered (nominal) motions are shown in Figure B.4. These filtered actuator motions are expected to be closer to the actual motion of the swashplate since the goal of the control system is not to attempt to keep the rotor cyclic constraint of Equation 2.4 filled for one or two blades, but rather to follow the commands of the pilot.

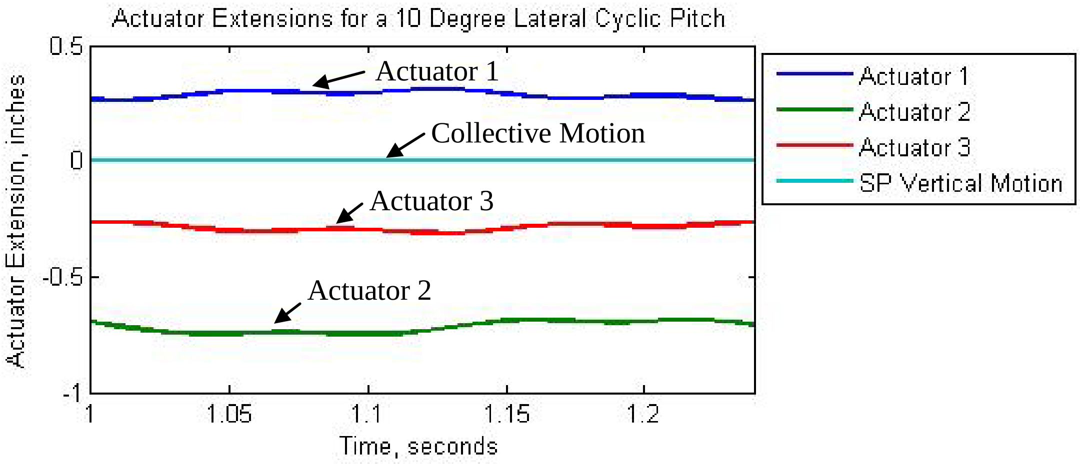

Figure B.3: Unfiltered Actuator Motion During One Revolution for θ_{col}=0 and θ_{1C}=10 degrees.

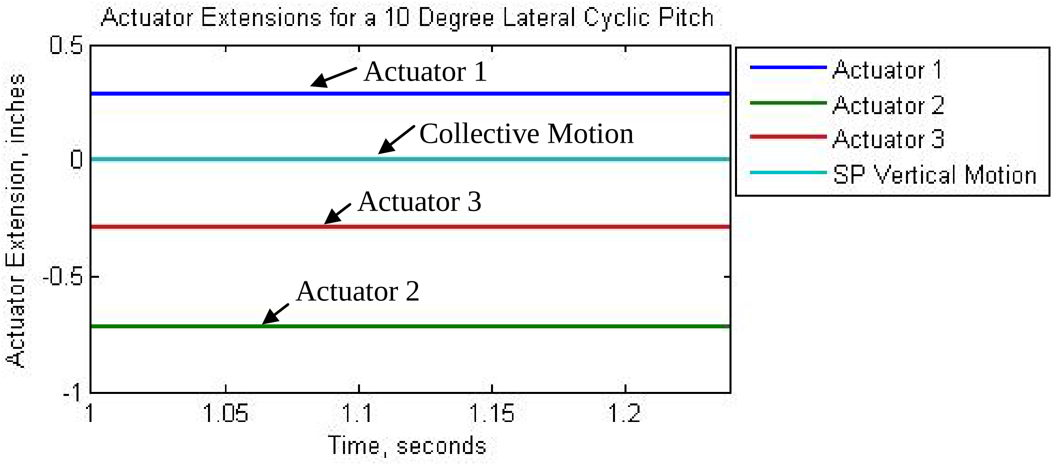

Figure B.4: Filtered Actuator Motion During One Revolution for θ_{col}=0 and θ_{1C}=10 degrees.

Figure B.4 shows the actuator extensions as they should be for a lateral cyclic command. Notice that all actuators have moved, not just actuator 2. The motion in actuators 1 and 3 that can be attributed to a tilt of the swashplate must always be equal and opposite, which is clearly shown in Figure B.4.

For a rotor with a positive lateral cyclic pitch, the pitch of each blades must be at its maximum when $\psi_{b,i}$=0, or when the blade points to the tail. This means that the swashplate must tilt such that the rear is higher than the front. Actuator 2 has a relatively large negative displacement in order to pull the front of the swashplate down. The maximum vertical position on the swashplate must be at $\psi=\varepsilon$ because this is location of the pitch link when the blade is at $\psi_{b,i}=0$. This explains the motion in actuators 1 and 3, because the right side of the swashplate must tilt up in order to enforce the pitch constraints—actuator 1 accordingly is extended and actuator 3 is retracted by the same amount.

Through these checks, the kinematic model implemented in the computer simulation is shown to adhere to the mathematical model described in Chapter 2. Further validation of this model would require experimentation that is beyond the scope of this project. Validation of the dynamic portion of the simulation was limited to checks similar to those described here.

Appendix C

Helicopter Parameters

The swashplate actuator modeling portion of this study uses helicopter geometric and inertial parameters similar to those of a UH-60. Table C.1 lists the values used. Recall that vectors in global coordinates are represented with an "**r**" and vectors in local, body-fixed coordinates are represented with an "**s**." The subscripts remain the same.

Parameter	Value	Units	Coordinate Frame
N_b	4		
ε	21.8	degrees	
Ω	27	rad/sec	
R	26.83	ft.	
$\mathbf{s}_{A,1}$	$[12,0,0]^T$	in.	$\{\mathbf{e}_1, \mathbf{e}_2, \mathbf{e}_3\}$
$\mathbf{s}_{A,2}$	$[0,12,0]^T$	in.	$\{\mathbf{e}_1, \mathbf{e}_2, \mathbf{e}_3\}$
$\mathbf{s}_{A,3}$	$[-12,0,0]^T$	in.	$\{\mathbf{e}_1, \mathbf{e}_2, \mathbf{e}_3\}$
$\mathbf{r}_{base,1}$	$[12,0,-23]^T$	in.	$\{\mathbf{E}_1, \mathbf{E}_2, \mathbf{E}_3\}$
$\mathbf{r}_{base,2}$	$[0,12,-23]^T$	in.	$\{\mathbf{E}_1, \mathbf{E}_2, \mathbf{E}_3\}$
$\mathbf{r}_{base,3}$	$[-12,0,-23]^T$	in.	$\{\mathbf{E}_1, \mathbf{E}_2, \mathbf{E}_3\}$
$\mathbf{s}_h$	$[-6,0,-2.5]^T$	in.	$\{\mathbf{x}_i, \mathbf{y}_i, \mathbf{z}_i\}$
$\mathbf{s}_b$	$[15,0,17]^T$	in.	$\{\mathbf{a}_1, \mathbf{a}_2, \mathbf{a}_3\}$
c_{PL}	14.5	in.	
r_p	16.16	in.	
M_a	-1500	in-lbs.	
$I_{f,\text{section}}$	8.28	slugs-in^2	
I_f	140.83	slugs-in^2	
m_{sp}	6.22	slugs	
r_{sp}	14.14	in.	
k_r	150	in-lbs/degree	

Table C.1: UH-60 Swashplate and Rotor Parameters

Table C.2 gives approximate values for many helicopters. This data is used for comparing different platforms. These values are representative.

Helicopter	Rotor Diam. (ft)	MTOW (lbs)	Rotor Speed (RPM)
BO105	32.29	5511	424
BK117	36.08	6270	383
EC135	33.5	6415	395
EC145	36.08	7903	383
UH-60	53.66	23500	258
CH-53	72.23	42000	185
CH-47*	60	25000	225
CH-53E	79	73500	177
AH-64	48.3	23000	290
MD900	33.83	6900	400
Bell 427	37	6350	395
CH-46*	51	12150	264
Bell 412	46	11900	314
OH-58	35.33	2313	395
KHI Rotor	38		346

* CH-47 and CH-46 are two-rotored, so the helicopter weight is double what is reported

Table C.2: Rotor Diameter, MTOW, and Rotor Speed of Various Helicopters [53, 72-75].

References

[1]. Lee, D., Horn, J., Sezer-Uzol, N., and Long, L., “Simulation of Pilot Control Activity During Helicopter Shipboard Operation,” *AIAA Atmospheric Flight Mechanics Conference and Exhibit*, Austin, TX, 11-14 August, 2003.

[2]. Lee, D., Sezer-Uzol, N., Horn, J., and Long, L., “Simulation of Helicopter Shipboard Launch and Recovery with Time-Accurate Airwakes,” *Journal of Aircraft*, Vol. 42, No. 2, March-April 2005.

[3]. Harrer, K.L., Yniguez, D., Majar, M., EllenBecker, D., Estrada, N., and Geiger, M., "Whole Body Vibration Exposure for MH-60S Pilots", *Proceedings of the 43rd Annual SAFE Association Symposium*, Salt Lake City, Utah, October 24-26, 2005.

[4]. Wilkinson, C.H., Roscoe, M.F., and VanderVliet, G.M., “Determining Fidelity Standards for the Shipboard Launch and Recovery Task," *Proceedings of the AIAA Modeling and Simulation Technologies Conference and Exhibit*, Montreal, Canada, August 2001.

[5]. Domke, Burkhard, “Main Rotor Head,” http://www.b-domke.de/AviationImages/Rotorhead/0235.html, Paris LeBourget, June, 1987. Accessed May 22, 2009.

[6]. “SH-2 Seasprite,” http://image36.webshots.com/36/5/78/29/316657829VKPMZr_ph.jpg , accessed May 23, 2009.

[7]. Roscoe, M.F. and Wilkinson, C.H., "DIMSS – JSHIP’S Modeling and Simulation Process for Ship/Helicopter Testing & Training," *AIAA Modeling and Simulation Technologies Conference and Exhibit*, Monterey, California, August 5-8, 2002.

[8]. Horn, J., Bridges, D., and Lee, D., "Flight Control Design for Alleviation of Pilot Workload During Helicopter Shipboard Operations," *Proceedings of the 62nd American Helicopter Society Forum*, Phoenix, AZ, May 9-11, 2006.

[9]. Lee, D., and Horn, J.F., "Simulation of pilot workload for a helicopter operating in a turbulent ship airwake," *Journal of Aerospace Engineering--Proceedings of the Institute of Mechanical Engineers, Part G,* Special Issue on Shipborne Aviation, Vol. 219, November 2005, pp.445-458.

[10]. Horn, J. F. and Bridges, D. O., "A Model Following Controller Optimized for Gust Rejection during Shipboard Operations," *Proceedings of the 63rd American Helicopter Society Forum*, Virginia Beach, VA, May 1-3, 2007.

[11]. Montanye, P., “Shipboard Helicopter Gust Response Alleviation Using Active Trailing Edge Flaps,” M.S. Thesis, Department of Aerospace Engineering, The Pennsylvania State University, State College, PA, 2008.

[12]. Straub, F.K. and Kennedy, D.K., "Design, Development, Fabrication, and Testing of an Active Flap Rotor System," *Proceedings of the 61st American Helicopter Society Forum*, Grapevine, TX, June 1-3, 2005.

[13]. Haug, E.J., *Computer aided kinematics and dynamics of mechanical systems. Vol. 1: basic methods*, Allyn & Bacon, Inc. Needham Heights, MA, USA, 1989.

[14]. Chace, M.A., “Vector Analysis of Linkages,” *Transactions of the ASME, Journal of Engineering for Industry,* University of Michigan, Ann Arbor, Michigan, August 1963.

[15]. Uicker, J.J. Jr., Pennock, G.R., and Shigley, J.E., *Theory of Machines and Mechanisms*, 3rd Edition, Oxford University Press, New York, 2003.

[16]. Merlet, J.-P., *Parallel Robots,* 2nd Edition, Springer, Netherlands, 2006.

[17]. Saffarian, M., Fahimi, F., "A Comprehensive Kinematic Analysis of A Model Helicopter's Actuating Mechanism," *46th AIAA Aerospace Sciences Meeting and Exhibit*, January 7-10, 2008, Reno, Nevada.

[18]. Denavit, J. and Hartenberg, R.S., “A Kinematic Notation for Lower-Pair Mechanisms Based on Matrices,” *Transactions of the ASME, Journal of Applied Mechanics,* series E, Vol. 22, No. 2, June 1955, pp.215-221.

[19]. Kim, S. K. and Tilbury, D. M., "Mathematical Modeling and Experimental Identification of an Unmanned Helicopter Robot with Fly-Bar Dynamics," *Journal of Robotic Systems*, Vol. 18, No. 3, 2004, pp. 95-116.

[20]. Lange, C., Ranjbaran, F., Angeles, J., and Goritschnig, G., "The Kinematics of the Swashplate Mechanism of a VTOL Unmanned Aerial Vehicle," *Multibody System Dynamics*,Vol. 3, pp. 333–365, 1999.

[21]. Lange, C., Angeles, J., Ranjbaran, F., and Goritschnig, G., "The Dynamics of the Swashplate Mechanism of a VTOL Unmanned Aerial Vehicle," *Multibody System Dynamics*,Vol. 5, pp. 105-131, 2001.

[22]. Abhishek, A., Datta, A., and Chopra, I., "Prediction of UH-60A Structural Loads Using Multibody Analysis and Swashplate Dynamics," *Journal of Aircraft*, Vol. 46, No. 2, March-April, 2009.

[23]. Leishman, J.G., *Principles of Helicopter Aerodynamics*, 2nd Ed., Cambridge University Press, New York, 2006, page 372.

[24]. Haber, A., Jacklin, S.A., and deSimone, G., "Development, Manufacturing, and Component Testing of an Individual Blade Control System for a UH-60 Helicopter Rotor," *Proceedings of the AHS Aerodynamics, Acoustics, and Test and Evaluation Technical Specialists Meeting*, San Francisco, CA, January 23-25, 2002.

[25]. Williams, J.A. and Hyncica, A.M., “Mechanisms of Abrasive Wear in Lubricated Contacts,” *Wear*, Vol. 152, pp. 57-74, 1992.

[26]. Kaneta et al. “Tribology of Flexible Seals for Reciprocating Motion.” *Journal of Tribology*. Oct. 2000. Vol. 122, Issue 4, p790.

[27]. Arnold, U.T.P., Neuheuser, T., and Bartels, R., "Development of an Integrated Electrical Swashplateless Primary and Individual Blade Control System," *Proceedings of the 63rd American Helicopter Society Forum*, Virginia Beach, VA, May 1-3, 2007.

[28]. Laing, E.M., "Army Helicopter and Vibration Survey Methods and Results," *Journal of the American Helicopter Society*, Vol. 19, No. 2, 1974, pp. 4-30.

[29]. Loewy, R., "Helicopter Vibrations: A Technological Perspective," *Journal of the American Helicopter Society*, October 1984, pp. 4-30.

[30]. Konstanzer, P., Enenkl, B., Aubourg, P., and Cranga, P., "Recent advances in Eurocopter’s passive and active vibration control," *Proceedings of the 64th American Helicopter Society Forum*, Montreal, Canada, April 29 - May 1, 2008.

[31]. Wood, E.R., Powers, R., Cline, J.H., and Hammond, C.E., "On Developing and Flight Testing a Higher Harmonic Control System," *Journal of the American Helicopter Society*, Vol. 30, No. 1, 1985, pp. 3-20.

[32]. Miao, W., Kottapalli, S.B.R. and Frye, H.M., "Flight Demonstration of Higher Harmonic Control (HHC) on S-76," *Proceedings of the 42nd American Helicopter Society Forum*, Washington D.C., 1986, pp. 777-791.

[33]. Walsh, D.M. "Flight Test of an Open Loop Higher Harmonic Control System of an S-76A Helicopter," *Proceedings of the 42nd American Helicopter Society Forum*, Washington D.C., June 2-4, 1986, pp. 832-843.

[34]. Guinn, K.F., "Individual Blade Control Independent of a Swashplate," *Journal of the American Helicopter Society*, July 1982, pp. 25-31.

[35]. Jacklin, S.A., Nguyen, K.Q., Blaas, A., and Richter, P., "Full Scale Wind Tunnel Test of a Helicopter Individual Blade Control System," *Proceedings of the 50th American Helicopter Society Forum*, Washington, DC, May 11-13, 1994.

[36]. Jacklin, S.A., Blaas, A., Teves, D., and Kube, R., "Reduction of Helicopter BVI Noise, Vibration, and Power Consumption Through Individual Blade Control," *Proceedings of the 51st American Helicopter Society Forum*, Fort Worth, TX, May 9-11, 1995.

[37]. Jacklin, S., Haber, A., de Simone, G., Norman, T., and Shinoda, P., "Full Scale Wind Tunnel Test of an Individual Blade Control System for a UH-60 Helicopter.", *Proceedings of the 58th American Helicopter Society Forum*, Montreal, Canada, June 11-13, 2002.

[38]. Norman, T.R., Shinoda, P.M., Kitaplioglu, C., Jacklin, S.A., Sheikman, A., "Low-Speed Wind Tunnel Investigation of a Full-Scale UH-60 Rotor System," *Proceedings of the 58th American Helicopter Society Forum*, Montreal, Canada, June 11-13, 2002.

[39]. Kessler, C., Fuerst, D., and Arnold, U.T.P., "Open Loop Flight Test Results and Closed Loop Status of the IBC System on the CH-53G Helicopter," *Proceedings of the 59th American Helicopter Society Forum*, Pheonix, AZ, May 6-8 2003.

[40]. Arnold, U.T.P., and Furst, D., "Closed Loop IBC Results from CH-53G Flight Tests," *Aerospace Science and Technology*, Vol. 9, Issue 5, July, 2005, pp. 421-435.

[41]. “Single rotorblade control”, www.zf.com, accessed June 29, 2009.

[42]. Splettstoesser et al., "Helicopter Noise Reduction by Individual Blade Control (IBC) -Selected Flight Test and Simulation Results," *Proceedings of the RTO-AVT Symposium*, Braunschweig, Germany, May 8-12, 2000.

[43]. Kube, R., Schimke, D., and Jänker, P., "Active/Adaptive Rotor Blade Control for Disturbance Rejection and Performance Enhancement," *Proceedings of the RTO-AVT Symposium*, Braunschweig, Germany, May 8-12, 2000.

[44]. Shen, Jinwei., Yang, Mao., Chopra, Inderjit., “Swashplateless Helicopter Rotor with Trailing-Edge Flaps for Flight and Vibration Control.” *Journal of Aircraft*, Vol. 43, No. 2, March-April 2006.

[45]. Myrtle, T.F. and Friedmann, P.P., "Vibration Reduction in Rotorcraft Using the Actively Controlled Trailing Edge Flap and Issues Related to Practical Implementation," *Proceedings of the 54th American Helicopter Society Forum,* Washington, D.C., May 20-22, 1998.

[46]. Viswamurthy, S.R. and Ganguli, R., "Using the Complete Authority of Multiple Active Trailing-edge Flaps for Helicopter Vibration Control," *Journal of Vibration and Control,* 14(8), pp. 1175–1199, 2008

[47]. Straub, F.K. and Hassan, A.A., "Aeromechanic Considerations in the Design of a Rotor with Smart Material Actuated Trailing Edge Flaps," *Proceedings of the 52nd American Helicopter Society Forum*, Washington, D.C., June 4-5, 1996, pp. 704-714.

[48]. Straub, F., Ealey, M., and Schetky, L. McD., "Application of Smart Materials to Helicopter Rotor Active Control," *Proceedings of SPIE Symposium on Smart Structures and Materials,* San Diego, March 3-6, 1997.

[49]. Straub, F.K., Charles, B.D., "Comprehensive modeling of rotors with trailing edge flaps," *Proceedings of the 55th American Helicopter Society Forum*, Montreal, May 1999.

[50]. Straub, F.K., Ngo, H.T., Anand, V., Domzalski, D.B., "Development of a piezoelectric actuator for trailing edge flap control of rotor blades," *Proceedings of the SPIE Symposium on Smart Structures and Materials*, Newport Beach, March 1999.

[51]. Hassan, A.H., Straub, F.K., and Noonan, K., "Experimental/Numerical Evaluation of Integral Trailing Edge Flaps for Helicopter Rotor Applications," *Proceedings of the 56th American Helicopter Society Forum*, Virginia Beach, Va, May 2000.

[52]. Hall, S.R., Tzianetopoulou, T., Straub, F.K., and Ngo, H., "Design and Testing of a Double Xframe Piezoelectric Actuator," *Proceedings of the SPIE Conference on Smart Structures and Materials*, Newport Beach, CA, March 2000.

[53]. Straub, F.K. et al., "Development and whirl tower testing of the SMART active flap rotor," *Proceedings of the SPIE Symposium on Smart Structures and Materials,* San Diego, March 2004.

[54]. Straub, et al., "Wind Tunnel Test of the SMART Active Flap Rotor," *Proceedings of the 65th American Helicopter Society Forum*, Grapevine, TX, May 27-29, 2009.

[55]. JanakiRam, et al., "Blade-Vortex Interaction Noise Characteristics of a Full-Scale Active Flap Rotor," *Proceedings of the 65th American Helicopter Society Forum*, Grapevine, TX, May 27-29, 2009.

[56]. Hasegawa, et al., "Experimental and Analytical Results of Whirl Tower Test of ATIC Full Scale Rotor System," *Proceedings of the 57th American Helicopter Society Forum*, Washington, DC, May 9-11, 2001.

[57]. Kobiki, N., Shigeru, S., Takehito, K., and Takayoshi, K., "Design and Performance Evaluation of Full Scale On-Board Active Flap System," *Proceedings of the 63rd American Helicopter Society Forum*, Virginia Beach, Virginia, May 1-3, 2007.

[58]. Fink, D.A., Hawkey, T.J., and Gaudreau, M.P.J., "An Electromagnetic Actuator for Individual Blade Control," *Proceedings of the 56th American Helicopter Society Forum*, Virginia Beach, VA, May 2-4, 2000.

[59]. Hofinger, M., and Leconte, P., "Development of an Active Flap Rotor Model," ONERA: Tire a Part , no. 108, pp. 1-12. 2004

[60]. Dieterich, O., Enenkl, B., and Roth, D., "Trailing Edge Flaps for Active Rotor Control: Aeroelastic Characteristics of the ADASYS Rotor System," *Proceedings of the 62nd American Helicopter Society Forum*, Pheonix, AZ, May 9-11, 2006.

[61]. Cheng, R. P., Theodore, C.R., Celi, R., “Effects of Higher Harmonic Control on Rotor Performance,” *Proceedings of the 56th American Helicopter Society Forum*, Virginia Beach, Virginia, May 2-4, 2000.

[62]. Falls, J., Datta, A., and Chopra, I., “Performance Analysis of Trailing Edge Flaps in Helicopter Primary Control,” *AHS Specialist’s Conference on Aeromechanics*, San Francisco, CA, January 23-25, 2008.

[63]. Liu, L., Friedmann, P.P., Kim, I., Bernstein, B.S., "Simultaneous Vibration Reduction and Performance Enhancement in Rotorcraft Using Actively Controlled Flaps," *47th AIAA/ASME/ASCE/AHS/ASC Structures, Structural Dynamics, and Materials Conference*, May 1-4, 2006, Newport, Rhode Island.

[64]. Kim, J-S, “Design and Analysis of Rotor Systems with Multiple Trailing Edge Flaps and Resonant Actuators,” Doctoral Thesis, The Pennsylvania State University, State College, PA. 2005.

[65]. Szefi, J., “Investigation into Centrifugally Powered Pneumatic Trailing Edge Flap Actuation in Rotorcraft,” Invercon White Paper. April 29 2009.

[66]. Shigley, J. E. and Mischke, C.R., *Mechanical Engineering Design*, 6th Edition, McGraw Hill, New York, NY, 2001.

[67]. "Abrasive Wear", www.pall.com/Aerospace_18134.asp. Accessed July 15, 2009.

[68]. McGuire, D.P., "High Stiffness ("Rigid") Helicopter Pylon Vibration Isolation Systems," *Proceedings of the 59th American Helicopter Society Forum*, Pheonix, AZ, May 6-8 2003.

[69]. *Bell 412 Product Specifications*, Bell Helicopter Textron, January 2006. http://www.bellhelicopter.com, Accessed July 17, 2009.

[70]. Thiel, M., "Actuation of an Active Gurney Flap for Rotorcraft Applications," MS Thesis, The Pennsylvania State University, 2006.

[71]. Mistry, M., "Induced Warp Systems To Obtain Active Twist Of Rotor Blades", M.S. Thesis, The Pennsylvania State University, 2008

[72]. Derby, M.R. and Yamauchi, G.K., "Design of 1/48th Scale Models for Ship Rotorcraft Interaction Studies," *Proceedings of the 21st AIAA Applied Aerodynamics Conference*, Orlando, FL, June 23-26, 2003.

[73]. Filippone, A., "Data and Performances of Selected Aircraft and Rotorcraft," *Progress in Aerospace Sciences*, Vol. 36, 2000, pp. 629-654.

[74]. Straub, F., "A feasibility study of using smart materials for rotor control," *Proceedings of the 49th American Helicopter Society Forum*, St. Louis, MO, May 19–21 1993.

[75]. Sturgeon, W.R. and Phillips, J.D., "A Mathematical Model of the CH-53 Helicopter," NASA Technical Memorandum 81238.

[76]. Liu, L., Padthe, A.K., and Friedmann, P.P., "A Computational Study of Microflaps with Application to Vibration Reduction in Helicopter Rotors," *Proceedings of the 50th AIAA/ASME/ASCE/AHS/ASC Structures, Structural Dynamics, and Materials Conference*, Palm Springs, CA, 4 - 7 May 2009.